Tampereen yliopisto

HANNA HULKKONEN

Nanophotonic Materials by Block Copolymer Self-Assembly

Tampereen yliopiston väitöskirjat 386

Tampere University Dissertations 386

HANNA HULKKONEN

Nanophotonic Materials by Block Copolymer Self-Assembly

ACADEMIC DISSERTATION
To be presented, with the permission of
the Faculty of Engineering and Natural Sciences
of Tampere University,
for public discussion in the Auditorium TB109
of the Tietotalo building, Korkeakoulunkatu 1, Tampere,
on 12 March 2021, at 12 o'clock.

ACADEMIC DISSERTATION
Tampere University, Faculty of Engineering and Natural Sciences
Finland

Responsible supervisor and Custos	Associate Professor Tapio Niemi Tampere University Finland	
Pre-examiners	Professor Janne Ruokolainen Aalto University Finland	Professor Joona Bang Korea University Republic of Korea
Opponent	Assistant Professor Pawel Majewski University of Warsaw Poland	

The originality of this thesis has been checked using the Turnitin Originality Check service.

Cover design: Roihu Inc.

ISBN 978-952-03-1881-9 (print)
ISBN 978-952-03-1882-6 (pdf)
ISSN 2489-9860 (print)
ISSN 2490-0028 (pdf)
http://urn.fi/URN:ISBN:978-952-03-1882-6

PunaMusta Oy – Yliopistopaino
Joensuu 2021

Science is magic that works.

- Kurt Vonnegut

… however, a researcher will tell you that when the science finally works after the n^{th} try, it must be magic.

PREFACE

In late 2015, I joined the Nanophotonics research group and began working at the Optoelectronics Research Centre of the former Tampere University of Technology. During the years there have been quite a few changes. One of the biggest ones was the university merger in 2019 and the start of the newly formed Tampere University. Despite the changes, the experimental research presented in this thesis has been carried out in essentially the same research environment during the years 2015–2020. It has been a privilege to work in the Nanophotonics research group and to be a part of the photonics community.

First and foremost, I want to sincerely thank my supervisor Assoc. Prof. Tapio Niemi for the opportunity to join his research group and to pursue a doctorate in the field of photonics. His ideas, expertise and guidance have been essential during these past years and without him this thesis would never have happened. I also want to thank Dr. Turkka Salminen, my unofficial advisor in science and all other things. I'm thankful for the many fruitful conversations that we had and the knowledge that he shared with me. I would also like to acknowledge other former members of my research group. Dr. Tero Isotalo, thank you for passing on your knowledge of electron-beam lithography and then entrusting the whole system into my hands. I appreciate the help and advice that I received from Dr. Sozaraj Rasappa, and I wish to thank Aashish Sah and Markus Hiekkamäki for their contributions to the experimental work. All in all, I had many awesome colleagues who made the whole experience worthwhile. The quality of the jokes in the coffee room has arguably always been quite poor, but the discussions have been great and the company even better.

The experimental research wouldn't have really happened without the help of our wonderful laboratory staff. I would like to thank Mervi Koskinen, Ilkka Hirvonen

and Maija Karjalainen for teaching me the ins and outs of the cleanroom and for making sure that the labs ran as smoothly as possible. Mariia Bister, thank you for all the support and for everything else, too. And my sincere thanks to Jarno Reuna for keeping every machine and system going in the cleanroom even when they made a valiant effort to die in the middle of things.

I am grateful for the research funding provided by the TUT Graduate School. The work has also been supported by projects from the Academy of Finland. In addition, I'm thankful for the personal financial support that I received from the Finnish Foundation for Technology Promotion (TES) and the Emil Aaltonen Foundation. This work is a part of the Academy of Finland Flagship Programme, Photonics Research and Innovation (PREIN).

Finally, I would like to thank my friends and family for their love and support during these years. My life has been blessed with some of the most amazing people. Thank you for being a part of my journey and believing that I could do this.

Hanna Hulkkonen

Tampere, October 2020

ABSTRACT

Nano- and microstructures are the core building blocks of modern-day devices such as phones, cameras, solar cells and lasers. Development of nanofabrication methods is essential if we want to continuously achieve smaller, faster and more sophisticated devices. The self-assembly of molecules is a promising scalable and low-cost nanopatterning method. Block copolymers are large molecules that can, under the correct conditions, self-organize into well-defined 2D and 3D patterns. The patterns can then be used to create functional nanoscale devices. In this thesis the prospects of block copolymer lithography for the fabrication of nanophotonic materials are explored.

The thesis focuses on the self-assembly and use of polystyrene–polyvinylpyridines (PS–PVP). The work describes the development of a solvent vapour annealing device that uses a novel type of feedback control to manipulate the swelling of the polymer films for a more repeatable annealing process. The solvent annealing device is one of the most precise systems demonstrated so far. It is also the only one with a control mechanism fast enough to enable cyclic annealing. It is shown that high-molecular weight PS–PVP can be made to self-assemble into nanopatterns in less than 10 min as opposed to the usual timescale of hours.

The produced polymer nanopatterns are utilized in the fabrication of mesoporous silicon that has tunable optical properties. It is possible to control the pore size, and consequently the effective refractive index of the material, in a straightforward plasma etching process during pattern transfer. The method could be used to create thin films that have tunable or ultra-low refractive indices. Finally, block copolymer lithography is combined with a template-stripping process to create patterned gold metasurfaces. The fabricated sub-wavelength nanodome arrays exhibit omnidirectional, broadband, perfect absorption of visible light. According to simulations, the light absorption and the electric field enhancement arise from localized surface plasmon and gap plasmon resonances in the material. The plasmonic coatings could be exploited in emerging energy-harvesting applications or in high-sensitivity optical sensors.

CONTENTS

LIST OF ABBREVIATIONS

BCP	Block copolymer
DSA	Directed self-assembly
EBL	Electron-beam lithography
EMA	Effective medium approximation
FDTD	Finite-difference time-domain method
FIB	Focused ion beam milling
FinFET	A fin field-effect transistor
GISAXS	Grazing incidence small angle X-ray scattering
GUI	Graphic user interface
IC	Integrated circuit
ICP	Inductively coupled plasma etching
IRDS	International Roadmap for Devices and Systems
ITRS	International Technology Roadmap for Semiconductors
LSP	Localized surface plasmon
NIL	Nanoimprint lithography
NIR	Near-infrared (light)
ODT	Order–disorder transition
P2VP	Poly(2-vinylpyridine)
P4VP	Poly(4-vinylpyridine)
PID	Proportional–Integral–Derivative (controller)
PMMA	Poly(methyl methacrylate)

PS	Polystyrene
PTFE	Polytetrafluoroethylene, 'Teflon'
RF	Radio frequency
RIE	Reactive ion etching
RTP	Rapid thermal processing
SCFT	Self-consistent field theory
SEM	Scanning electron microscope
SF_6	Sulfur hexafluoride
$SiCl_4$	Silicon tetrachloride
SiF_4	Silicon tetrafluoride
SR	Swelling ratio
SVA	Solvent vapour annealing
TEC	Thermoelectric cooling
THF	Tetrahydrofuran
UV	Ultra-violet (light)

ORIGINAL PUBLICATIONS

Publication I H. Hulkkonen, T. Salminen and T. Niemi, Block copolymer patterning for creating porous silicon thin films with tunable refractive indices, *ACS Applied Materials & Interfaces*, vol. 9, no. 37, 31260–31265, 2017.

Publication II H. Hulkkonen, A. Sah and T. Niemi, All-metal broadband optical absorbers based on block copolymer nanolithography, *ACS Applied Materials & Interfaces*, vol. 10, no. 49, 42941–42947, 2018.

Publication III H. Hulkkonen, T. Salminen and T. Niemi, Automated solvent vapor annealing with nanometer scale control of film swelling for block copolymer thin films, *Soft Matter*, vol. 15, no. 39, 7909–7917, 2019.

Author's contribution

Publication I — This work explores the modification of the refractive index of silicon via block copolymer patterning. The author designed the experiments together with T. Niemi. The author prepared all the samples and performed the optical measurements and the SEM imaging. T. Niemi coded the scripts for the effective medium approximations and the author did the data analysis. The manuscript was written by the author with contributions from T. Salminen and T. Niemi.

Publication II — This work describes the creation of a patterned metal metasurface that functions as an omnidirectional, broadband optical absorber. The author designed the experiments together with T. Niemi. Preliminary template-stripping tests were done by A. Sah. The author prepared most of the samples, characterized them and analysed the measurement data. FDTD modeling was done together with T. Niemi. The author wrote the manuscript with contributions from T. Niemi.

Publication III — This work presents the development of a computer-controlled solvent vapour annealing device for rapid self-assembly. The device and the MATLAB control program were initially developed by T. Salminen and T. Niemi and then further developed by the author. The author carried out the annealing tests, the characterization and the data analysis. The manuscript was written by the author with contributions from T. Salminen and T. Niemi.

1 INTRODUCTION

The development of science and technology has been going onwards at a stunning pace. The electron microscope was invented in the early 1930s. The first transistors were demonstrated in the late '40s while space flight was achieved in the '50s. Microprocessors and personal computers emerged in the '70s. Optical data storage was invented in the '90s and mobile phones became a commodity in the 21st century. A breakthrough in quantum computing was achieved just last year. Actually, the development of technology has been progressing so fast that it's hard to keep up with it. To quote Carl Sagan: *"We live in a society exquisitely dependent on science and technology, in which hardly anyone knows anything about science and technology."*

Many of those key inventions have to do with the development of micro- and nanofabrication techniques. Nanofabrication refers to processes that make one-, two- or three-dimensional nanostructures from various materials. Structurally complex patterns and nanoscale features come together to form functional components, devices and products. A major driving force for the development of nanofabrication methods has been the desire to pursue smaller, lighter, faster, and smarter electronic devices. According to Moore's Law, which has become more of a self-fulfilling prophecy than a prediction, the number of transistors in an integrated circuit doubles every two years. This means that the nanostructures that make up the transistors have had to become smaller and smaller as time goes on. Consider this: the chipset in your mobile phone now has *several billion* transistors and the phone is several million times faster than the roomful of computers that were used to guide the Apollo space flights.

The current semiconductor device mass production relies heavily on photolithography. In photolithography the nanopatterns are formed on a light-sensitive polymer

via masked exposure to ultraviolet light. The patterning resolution of traditional photolithography is inherently limited by the diffraction of light. Feature downscaling has therefore focused on using shorter wavelengths and multiple patterning steps to improve the minimum feature size. However, feature downscaling in this multistep process is getting increasingly more complex and extremely expensive. There are other lithography methods that are not similarly wavelength-limited. Nanoimprint lithography (NIL) is based on pattern replication from moulds, and electron-beam lithography (EBL) uses a beam of electrons to directly write patterns onto polymer resists.

Photolithography, NIL and EBL are so-called top-down methods, where you start with a block of material and slowly remove bits and pieces from it to produce the wanted device structure. Contrary to this, bottom-up processes start from the bottom and build the desired structures by selectively adding atoms, molecules or other building blocks together. In practice, this is best done using materials that can self-organize. Nature is very good at self-assembly. Chains of polypeptides fold into three-dimensional functional proteins and DNA helices get replicated almost perfectly from base nucleotides. On a molecular scale, self-assembling materials come together spontaneously to form organized structures due to thermodynamics and inter- and intramolecular forces. Molecular self-assembly would be a straightforward and low-cost way of fabricating extremely small patterns and structures. One of the main challenges in this bottom-up approach is how to make sure that the structures assemble in the correct way – and in a reproducible manner.

It was discovered already in the 1960s that if you coupled two thermodynamically incompatible polymer chains together, they would separate into repeating nanopatterns [1]. These are *block copolymers* (BCP), synthetic molecules with the ability to self-assemble into a wide variety of nanostructures including micelles, cylinders, lamellae and gyroids. Block copolymers produce periodic patterns that are in the size range of 10 to 100 nm. This is a size range that is currently difficult to obtain with any other established 1-step lithography method. It can be of course done with electron-beam lithography, but that requires expensive, state-of-the-art EBL equipment and there are limitations on the spatial area that can be patterned. Recent advances in polymer synthesis methods have made it possible to make even smaller, sub-5 nm features using so called high-χ BCPs [2], [3]. It has been thought that

self-assembled BCPs could be one of the next-generation lithography techniques for making nanoscale sensors and devices. The ITRS and IRDS roadmaps, that represent the interests of the five leading integrated chip manufacturers in the world, have listed directed self-assembly of BCPs as a potential technology for integrated circuit (IC) fabrication [4], [5]. Despite the promising potential and the copious amount of research, sub-10 nm BCP self-assembly has yet to become a mainstream lithography method.

A less explored avenue is the use of BCPs from the other end of the size range. BCP patterns close to 100 nm or larger have not been so appealing for IC fabrication. Perhaps that is why they have not been in the spotlight. However, nanomaterials with large periodic patterns hold importance for applications such as water purification with ultrafiltration membranes [6], [7] or the manipulation of light with photonic nanomaterials [8], [9]. Nanophotonic materials are artificial, nanostructured materials that can change how light is confined, focused, transported or reflected in the material. In order to manipulate photons of visible light (350–650 nm) the scale of the nanostructures has to often be smaller than the wavelength of the light. Recent examples of nanophotonic materials made by BCP self-assembly include tunable colour photonic crystals [10], [11], stimulation responsive photonic gels [12], antireflection coatings [13] and plasmonic metamaterials [9], [14]. The difficulty with the >100 nm pattern size is that it requires the use of high- or ultrahigh-molecular weight BCPs. There are considerable challenges in the synthesis and preparation of these long chain polymers. Furthermore, the large size of the molecules significantly hinders their self-assembly and the use of these BCPs is technically challenging.

I have been studying high-molecular weight linear BCPs at Tampere University in the Nanophotonics research group for the past five years or so. I have been interested in developing fast annealing techniques that would speed up the self-assembly process. I've also wanted to explore how the assembled patterns could be utilized in the fabrication of novel nanophotonic materials. These materials could be used in light-based technologies such as optical communications, energy harvesting and spectral sensing.

1.1 Research objectives and the scope of this work

The key questions in BCP lithography have been how to control the self-assembly and then how to utilize the produced patterns. How to turn the organic polymer nanopattern into inorganic nanostructures with the desired functionality? The aim of this doctoral project was to use molecular self-assembly to create nanophotonic materials that can change how light interacts with the matter in the nanoscale. The idea was to design and build materials that have unconventional optical properties such as total light absorption or modifiable refractive index.

This thesis focuses on one block copolymer family, the polystyrene–polyvinylpyridines (PS–PVP). It was chosen due to the versatility of the vinylpyridine block. The PVP part of the pattern can be either selectively removed or selectively doped with metal precursors. The selective block removal enables traditional mask-based lithography while the selective metal doping offers an easy way of producing uniformly distributed plasmonic nanoparticles.

The first objective of this thesis was to investigate PS–PVP self-assembly and find ways to control the pattern formation so that the desired shapes and geometries could be achieved. **Publication III** describes the working principle of an automated solvent annealing device that the research group has been developing over the past five years. The publication focuses on the assembly and annealing of high-molecular weight polymers, which are of most use in nanophotonic applications. Due to the large size of these molecules, their self-assembly is usually difficult and extremely slow, taking hours or several days to form patterns. For this, the group developed a way to quickly anneal polymers using controlled swelling. The aim was to create a device that would minimize or mitigate the influence of external factors on the pattern output and ensure that the process was reproducible. Reproducibility has been a major issue in previous solvent annealing devices. The developed device is currently one of the most precise solvent annealing systems to exist and the first one to be able to demonstrate controlled cyclic swelling.

The second objective was to use BCP patterns as templates for fabricating surfaces or coatings that have modifiable optical properties. These materials are similar to

metamaterials, where the properties of the material are defined, not simply by the material, but also by the composition, placement, and geometry of the nanostructures on the material surface. **Publication I** explores the use of the high-molecular weight PS–PVP patterns for conventional mask-based nanolithography. BCP patterning was used to create dense arrays of nanocavities in silicon, which altered the refractive index of the material. Effective medium approximations were used to identify that the index change was correlated to the size of the surface nanopores. **Publication II** is a direct continuation of the previous lithography research. The publication reports the study of patterned plasmonic coatings made using BCP lithography and templated metal stripping. The flexible metal coatings were structured with closely spaced sub-wavelength nanodomes. By changing the placement of the plasmonic gold structures, near-perfect, omnidirectional absorption of visible light could be achieved in the thin coatings.

2 BLOCK COPOLYMERS FOR NANOLITHOGRAPHY

The rise of block copolymers has been credited to the invention of living anionic polymerization in the 1950s, which provided an easy way to produce block copolymers by sequential addition of monomers [15]. Block copolymers are a good example of technologies that most people have never even heard of and yet encounter often in their daily lives. The first commercially used block copolymers were triblocks from poly(ethylene oxide) and poly(propylene oxide), which are best known by the commercial brand name Pluronic. These amphiphilic molecules are still widely used as surfactants in cosmetics and pharmaceuticals and also as key ingredients in encapsulated drug delivery systems and cell cultures [16]. Another major commercial success are the triblock copolymer rubbers made from styrene, butadiene and isoprene (SBS, SIS), which can be found in adhesives, elastic films, tire treads, shoe soles and asphalt.

To understand how block copolymers can be used to fabricate nanoscale patterns, we'll first have to go through a few basic concepts. A polymer is a macromolecule that consists of repeating structural units called monomers, which are covalently bonded together to form long chains. A block copolymer is a polymer that consists of two or more covalently linked polymer chains or "blocks" made from chemically differing monomers. The size of a polymer is defined by an average molecular weight M or the polymerization degree N, which is the number of monomeric segments in the polymer.

Block copolymers can be categorized by the number of blocks (di, tri- or multiblock) or by the molecular architecture (linear, branched). Figure 2.1 illustrates a few of the many linear and branched architectures of block copolymers. The simplest form

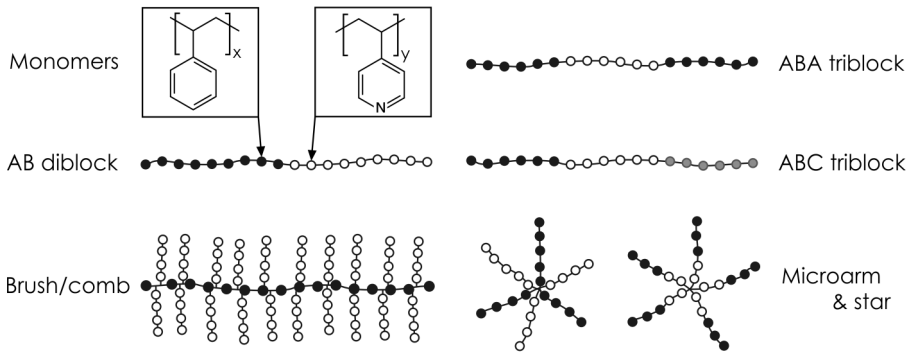

Figure 2.1 Schematic illustration of several types of block copolymer architectures. The blocks are made from repeating monomer units.

is an A-B diblock copolymer that consists of two linear chains of polymer A and polymer B linked end-to-end. Triblock copolymers have three linearly linked blocks (e.g. ABA or ABC) and star or miktoarm polymers have multiple blocks connected at one central point. Advances in polymerization techniques and post-polymerization functionalization have made it possible to fabricate also hyperbranched molecules such as bottle-brush or comb block copolymers and dendrimers [17]–[19]. BCPs are exceptionally versatile. The physical properties of these man-made molecules can be defined by selecting the sequence and chemical nature of the blocks and tuned by changing the molecular weights and the molecular architecture.

I have been interested in block copolymers that can be used for nanolithography and the fabrication of patterned nanophotonic materials. Block copolymers have the fascinating ability to spontaneously form nanoscale, periodic patterns under the correct processing conditions. These self-assembling molecules are an excellent candidate for bottom-up lithographic processes since they are able to form extremely small patterns over large surface areas. In practice, a self-assembled BCP thin film can act like a conventional photoresist and function as a lithographic mask or a template. The nanoscopic features of the self-assembled structures can be transferred onto the underlying substrate material using common lithographic processing steps such as plasma etching or metal evaporation. The polymer is typically stripped off or removed during the patterning process and none of the BCP is present in the final product. Essentially, the BCP is a sacrificial template, which is used to build inorganic nanostructures such as nanowires, fins, pillars, cones, grooves, pits or

nanoparticles. The lithographic process can be repeated multiple times for pattern density multiplication [20] or for the fabrication of more complex patterns and even three-dimensional structures [21]–[23].

2.1 Theory of block copolymer self-assembly

Theoretical and experimental efforts from the past 50 years have produced a solid foundation for understanding the complex behaviour of block copolymer systems and provided insights into how this self-assembling behaviour can be utilized in various technological applications. Self-assembling block copolymers consist of two or more blocks that are thermodynamically incompatible. Ideally, the polymer chains will arrange themselves in a minimum free energy configuration and minimize the contact area between the different blocks [24]. Since the blocks are still connected together at one end, complete segregation is not possible. Instead, phase separation occurs at microscopic length scales and results in a variety of so-called microdomain structures or phase morphologies. These morphologies are repeating patterns with a periodicity and size that are directly related to the length of the polymer chain.

One of the most useful and wide-spread theories of block copolymer self-assembly is the self-consistent field theory (SCFT). The theoretical framework for the SCFT was developed first by Helfand and Wasserman [25], [26] in the 1970s based on preliminary concepts developed around the same time period [27], [28]. The field theory could calculate the free energy of block copolymers using experimentally obtainable molecular parameters such as chain length, polymer composition and monomer interaction energy. Later developments made it possible to solve the field equations numerically, find the local free energy minima, and map the corresponding polymer phases [29].

Nowadays unified SCFT calculations can be used to predict phase transitions and the stability of different phase morphologies in polymer melts with reasonable accuracy. The phase behaviour of a block copolymer melt is described by three main factors: (1) the volume fraction of the blocks f, (2) the degree of polymerization N, and (3) the Flory-Huggins interaction parameter χ [24]. The predicted morphology diagram for a diblock copolymer is shown in Figure 2.2. It depicts the possible equilibrium

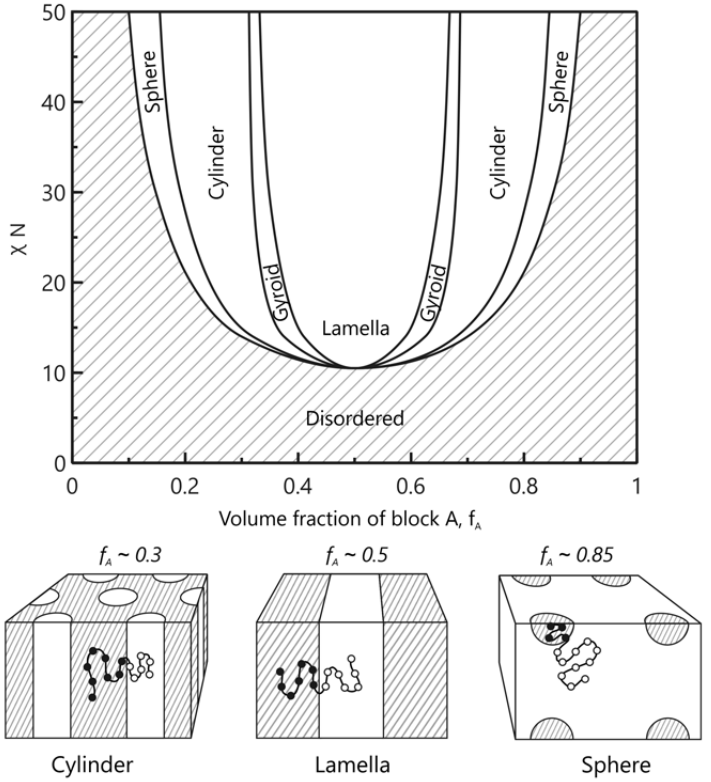

Figure 2.2 Theoretical morphology diagram of a linear diblock copolymer. Spherical, cylindrical, lamellar or gyroidal patterns form depending on the volume fraction of the blocks, the interaction parameter χ and the size of the polymer N. The phase diagram is adapted with permission from: Springer Nature, European Physical Journal E [30], Copyright (2009).

phases as a function of the block volume fraction and the product χN. An A-B block copolymer can form either body-centered-cubic spheres, hexagonally packed cylinders, a bicontinuous gyroid or symmetric lamellae depending on the relative volume fraction of the A and B blocks. Newer studies suggest that also orthorhombic and hexagonally close-packed spherical phases exist, though their stability regions are significantly smaller than the others [30]. This thesis focuses on morphologies that are useful for lithographic applications. For linear diblock copolymers, it means the cylinder and lamella phases, which can be used to make dot and line patterns.

As mentioned earlier, there are three factors that define the self-assembly behaviour of a BCP. In broad terms, the polymer volume fraction defines the morphology or the shape of the patterns. The other two parameters define the phase separation.

In the morphology diagram this is represented by the product χN, where χ is the Flory-Huggins interaction parameter and N the degree of polymerization. The Flory-Huggins χ parameter is temperature dependent and it will decrease as the temperature is increased and vice versa. As a consequence, the χN value (or the temperature) then determines whether the BCP melt exists in a phase-separated state or a disordered state. At elevated temperatures, the BCP chains are disordered and no patterns can form (see shaded area in Figure 2.2). When the temperature is decreased and the χN exceeds a critical value, phase separation will spontaneously occur. For a symmetric ($f = 0.5$) diblock copolymer the order–disorder transition (ODT) is predicted to happen at $\chi N = 10.495$ [31]. Phase separation behaviour can also be manipulated via the addition of solvent, since the χ value of a BCP changes with the solvent concentration. Thermal treatments and solvent treatments are the two main methods that are used to promote phase separation and obtain self-assembled patterns. These annealing methods are explored later in Chapter 3.

The size and periodicity of the polymer patterns is largely determined by the degree of polymerization N. According to Semenov [32], the domain length or the periodicity L_0 of a block copolymer pattern in the strong segregation regime ($\chi N \gg 10.5$) is estimated as

$$L_0 = aN^{2/3}\chi^{1/6} \tag{2.1}$$

where a is the statistical segment length of the polymer and χ is the Flory-Huggins interaction parameter. The degree of polymerization N is the number of monomeric segments in the polymer, which is related to the molecular weight of the BCP. In essence, a high-molecular weight BCP will form large patterns with a large periodicity and vice versa. During the past decade or so, researchers have been mostly interested in low molecular weight BCPs with the intention of making ever smaller and smaller patterns that could be used to solve the feature minimization problem presented by Moore's law. High- and ultra high-molecular weight polymers have been less studied, perhaps due to the technical difficulties related to their synthesis and slow self-assembly kinetics. This thesis focuses on that particular region, since high- and ultra high-molecular weight block copolymers would be well-suited for producing periodic nanostructures for photonic applications.

2.2 High-χ polystyrene-polyvinylpyridine

The desire for feature minimization in nanolithography has been steadily driving the block copolymer research towards so called high-χ materials. High-χ BCPs are able to form smaller patterns than BCPs with low χ values. A high χ value can compensate for a low N value so that the χN of the polymer will still stay above the order-disorder limit ($\chi N > 10.5$) during annealing. In technical terms the χ parameter quantifies the non-ideal polymer–polymer or polymer–solvent mixing effects. The parameter arises from the polymer lattice theory developed first by Paul Flory and Maurice Huggins to describe the free energy of mixing in polymer systems [33]. A positive Flory-Huggins χ value indicates a repulsion between the blocks and the larger the value, the more incompatible the monomers are. Sufficient incompatibility between the blocks is essential for self-assembly. For a pair of monomers, χ is often empirically defined as

$$\chi = a + b/T \tag{2.2}$$

where a and b are constants of entropic and enthalpic origin and T is the temperature in Kelvins. The constants can be extrapolated using experimentally measured ODT temperature values. Order–disorder transitions can be determined by small-angle X-ray scattering [34] or dynamic mechanical analyses [24]. According to equation 2.2, the χ parameter is temperature dependent. In addition, it also has a concentration dependence, which becomes more significant when the polymer is solvated during solvent annealing [35]. The effects of solvents on the Flory-Huggins parameter and on the self-assembly of BCPs are discussed in Chapter 3. Table 2.1 lists the Flory-Huggins parameters for some selected BCPs.

Polystyrene-poly(methyl methacrylate) (PS–PMMA) is one of the most studied block copolymers for lithographic applications and it could be said that it has become almost an industry standard. The wide spread use of PS–PMMA could be credited to its availability, well-known properties, easy synthesis and straightforward self-assembly using thermal annealing. However, PS–PMMA has a relatively low Flory-Huggins value ($\chi \approx 0.04$), which limits the smallest obtainable pattern size to about

Table 2.1 Flory-Huggins interaction parameters for a variety of block copolymers

Polymer	χ (25 °C)	Flory–Huggins $\chi\,(T)$	Reference
PS–PMMA	0.043	$+0.028 + 3.9/T$	[36]
PS–P2VP	0.178	$-0.033 + 63/T$	[37]
PS–PLA	0.217	$-0.112 + 98/T$	[38]
PS–PDMS	0.265	$+0.037 + 68/T$	[39]
PS–P4VP	~ 0.300	–	[40]

18 nm [41]. Furthermore, the segregation of the PS and PMMA domains is quite weak and subsequently the interface between the patterns is not clear-cut. Wide interfacial areas and pattern undulation can lead to increased line edge roughness (LER), which distorts the geometry of the nanopatterns and results in not-so-well defined nanostructures after lithographic pattern transfer [41]. Another factor that makes pattern transfer more difficult is that the PMMA domains have to be removed using etching or chain scission to make the lithographic masks. Nevertheless, PS–PMMA has been and still is in the spotlight for semiconductor industry applications as seen in recent demonstrations of fin field-effect transistors (FinFET) and static random-access memory circuit patterns [42]–[44].

This thesis focuses on the self-assembly and applications of a high-χ block copolymer called polystyrene-polyvinylpyridine (PS–PVP) (Figure 2.3). PS–PVPs are all-organic block copolymers with some unique properties, which make them promising candidates for next-generation nanolithography and nanostructure synthesis. Pyridines are known to be able to associate with metal ions using the nitrogen binding site in the pyridine either via metal-ligand coordination or via electrostatic binding [45]. Therefore, PS–PVP patterns can be selectively infused with metal-containing precursors to form inorganic nanostructures. This has enabled the creation of ordered nanoparticles and nanowires. Previously PS–PVPs have been utilized to synthesize nanostructures made from metals (gold, silver, platinum, nickel) [45], [46], ceramic hard mask materials (iron oxide, aluminium oxide) [47] and semiconductors (molybdenum disulfide, tungsten trioxide, zinc oxide) [48]–[50]. PVPs are also readily soluble in common alcohols while PS isn't. PVP regions can be selectively dissolved from the patterned BCP thin film to create lithographic masks or porous membranes

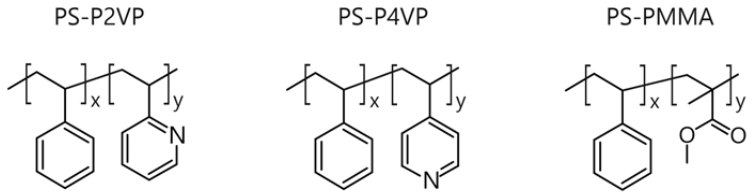

Figure 2.3 Examples of block copolymers: Polystyrene–poly(2-vinylpyridine), polystyrene–poly(4-vinylpyridine) and polystyrene–poly(methyl methacrylate).

[51]. Lithographic mask formation and metal nanopattern fabrication are described in more detail in Chapter 5.

Structurally the PVP monomer is very similar to PS, the only addition being a nitrogen in the aromatic ring structure (see Figure 2.3). It's been known for a while that the positioning of the nitrogen in the pyridine ring is significant and that the properties of the two isomers, P2VP (ortho position) and P4VP (para position), notably differ from each other. The Flory-Huggins interaction parameter of PS–P2VP has been calculated to be $\chi = 0.178$ at 25 °C [37]. The interaction parameter of PS–P4VP is estimated to be at least double of that. Alberda van Ekenstein et al. [40] calculated from miscibility studies of random copolymer blends that the χ value of PS–P4VP would be in the range of 0.30 to 0.35. Later studies obtained similar values using rheometry and small-angle X-ray scattering at temperatures between 160 and 195 °C [34]. The temperature dependence of $\chi_{PS-P4VP}$ is still somewhat unclear. Our group has studied the self-assembly of both PS–P2VP and PS–P4VP but the publications included in this thesis focus on the use of PS–P2VP.

2.3 Pattern orientation in thin films

In nanolithographic applications, BCPs are assembled onto substrates as thin films. The film thickness can vary from a few tens of nanometers to several hundreds of nanometers. It is often essential to control the orientation of the BCP patterns. For cylinder and lamella morphologies, a perpendicular domain orientation with respect to the substrate surface is typically preferable (see Figure 2.4a). Patterns also need to be well-aligned or well-ordered with relatively few defects in order to be useful as lithographic masks.

In thin films, the substrate and the free interface (air) begin to significantly influence the behaviour of the BCP. The blocks interact with surfaces in different manners due to their chemical dissimilarity and there may be a preferential segregation of one block at a particular interface. The preferential segregation or ”wetting” is a result of the system trying to minimize the surface and interfacial energies by putting the most energetically compatible block near the surface. BCP wetting behaviour has a significant effect on the orientation of the nanopatterns.

Ideally, surface wetting should be non-preferential (neutral) so that the block copolymer domains orient perpendicular to the surface (Figure 2.4a). Neutral wetting conditions can be achieved when the energy differences between the blocks and the surface are very similar: $\Delta\gamma_{A-sub} \approx \Delta\gamma_{B-sub}$. Large differences in the surface free energies lead to preferential wetting and the patterns tend to orient parallel to the surface as depicted in Figure 2.4b-d. Mixed pattern orientations can occur especially if one of the interfaces is neutral while the other is preferential. BCPs behave differently on different material surfaces due to their wetting behaviour. As a consequence, it becomes quite difficult to make universally working lithographic processes. Generally, studies have focussed on three approaches for controlling pattern formation in thin films: interface engineering, film thickness optimization and annealing techniques.

Interface engineering focuses on substrate surface modification techniques that balance the interfacial interactions between the blocks and the substrate making the surfaces effectively neutral. A variety of molecules have been shown to provide

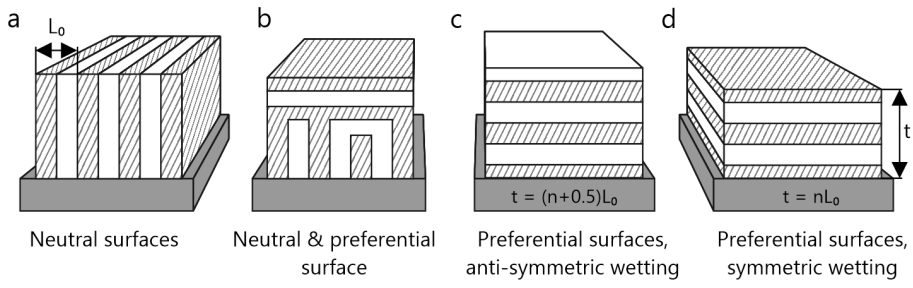

Figure 2.4 Orientation of lamellar BCP patterns on different substrates. (a) Neutral or non-preferential wetting promotes perpendicular pattern orientation. (b) One surface neutral, one preferential results in mixed pattern orientations. Preferentially wetting surfaces with either (c) asymmetric or (d) symmetric wetting behaviour produce horizontally stacked structures. The number of layers depends on the film thickness t and periodicity L_0.

sufficient surface neutrality and induce perpendicular pattern orientation when anchored onto the substrate surface. The most common approach has been to graft short chains of random copolymers onto the substrate surface forming a brush layer that contains a random mixture of both monomer units [52]–[54]. Neutral layers have also been composed of homopolymer brushes and their mixtures [55], [56], crosslinked polymers [57], [58], and other assembled molecules [59], [60]. Substrate surface modification processes have then been extended to fabricate chemical nanopatterns for directed self-assembly (DSA). A typical approach is to make a sparse pattern on the neutral brush layer using deep-UV immersion lithography or EBL and remove or modify selected regions of the brush layer by plasma treatment [61]. Removed regions can be backfilled with another brush for improved selectivity [62]. BCP patterns will align and orient according to the underlying chemical pattern since the two blocks prefer to wet different regions. Chemical patterning, coined chemoepitaxy, has been used to obtain defect-free arrays of aligned, perpendicular lamellae for line density multiplication with the end goal of incorporating DSA into 300 mm wafer process lines at semiconductor fabrication plants [63], [64]. Isolated features such as bends, jogs and T-junctions for integrated circuits have also been demonstrated [65].

While effective when done correctly, molecular surface functionalization is a delicate balance between brush layer thickness, surface coverage and brush composition. It involves a lengthy process of substrate cleaning, spin-coating, annealing and washing. In the case of chemoepitaxy there are additional steps of lithography, etching and brush deposition. Some functionalized random copolymer molecules are commercially available, though expensive, such as hydroxyl-terminated PS-ran-PMMA. Others have very limited availability and need to be synthesized by the research groups themselves. Our group has chosen not to pursue brush functionalization and this work has experimented with other techniques for domain orientation.

Film thickness is one of the other two methods that influences the pattern formation in thin films. The film thickness should ideally match the domain periodicity L_0 of the block copolymer as multiples of n or $n + 0.5$ (where n = 1,2,3...) depending on the wetting symmetry of the thin film (Figure 2.4c, d). If the film thickness is incommensurate with the periodicity, the BCP may redistribute over the surface during annealing so that locally the film thickness matches nL_0 or $(n + 0.5)L_0$ [66].

The local variation of the film thickness results in an uneven surface topography. The phenomenon is known as terracing or island/hole formation. Terracing is unwanted as it can lead to a film that has local changes in the pattern morphology or orientation especially near the terrace edges [67], [68]. The film thickness can also be used as a way to control the orientation of the BCP patterns. Patterns may orient perpendicular to the substrate especially if the film thickness is less than the pattern periodicity ($t < L_0$), meaning monolayer or submonolayer films [67].

The last method for controlling self-assembly in thin films is annealing and a wealth of techniques used during annealing. Annealing of thin films is discussed in more detail in the following Chapter 3. Various other methods can be used at the same time to guide BCP patterns into the desired geometry, order or direction. External forces such as electric fields [69], [70], shearing [61], temperature gradients [71], [72] or solvent evaporation [73] have been demonstrated to control pattern orientation or alignment. Other essential tools for directing the self-assembly during annealing are pre-patterned topographic substrates (graphoepitaxy) or the previously discussed chemically patterned surfaces (chemoepitaxy).

3 ANNEALING METHODS

BCP thin films that are spin-coated or cast onto substrates are typically initially disordered. The solvent in the casting solution evaporates rapidly and the polymer chains are kinetically trapped in a metastable, poorly ordered morphology. Annealing is therefore required to promote chain mobility and initiate microphase separation. Ideally the polymer would reach an equilibrium morphology after annealing. In practice, the behaviour of BCPs is not so straightforward especially as thin films. Substrate and interface effects, film thickness and film processing history can affect the outcome of annealing. BCP systems often experience energy barriers for chain re-organization, which prevent reaching the global thermodynamic equilibrium and result in persisting defects in the pattern [74]. Without external guidance, BCP systems will form a polygrain structure where the pattern is ordered inside multiple small grains. To overcome this, pre-patterned substrates (DSA) can be used to guide the BCP into the preferred pattern alignment during annealing. Annealing is typically done either by heating the thin film or by partially solvating it using a suitable solvent vapour. The process becomes more complicated and time-consuming as the complexity of the chain architecture increases or as the molecular weight is increased. It is important to note that not all annealing techniques suit all BCPs.

3.1 Thermal annealing

In thermal annealing the polymer thin film is heated above or near the glass-transition temperature T_g to allow chain movement. Typically thermal annealing has been done by placing the sample on a hot plate or in a vacuum oven and heating the sample for extended periods. At elevated temperatures the molecule chains begin diffusing and then phase separate locally leading to small grains. During extended thermal

annealing the grains coarsen and the defect density decreases as defects diffuse through the film, encounter other defects and annihilate each other. As the defect density decreases, it takes longer and longer for the defects to meet and annihilate. The coarsening of the grain size ξ scales according to a power law as $\xi = kt^{\alpha}$, where t is time, k is a prefactor and the exponent α describes the ordering mechanism [75]. For thin films with sphere or cylinder morphologies experimental studies have calculated the exponent as $\alpha = 0.25 - 0.28$ [76], [77]. This means that hexagonal ordering in micron-sized grains will take hours or several days of oven annealing.

Conventional thermal annealing can realistically only offer small-scale ordering due to the slow self-assembly kinetics. Motivated by the interest in incorporating BCPs into IC manufacturing, many methods have been developed to improve ordering and cut down on the required annealing time. Since kinetics scale with temperature, a logical approach is to increase the annealing temperature. However, thermal treatments are fundamentally limited by the ODT temperature, above which the BCP becomes disordered and phase separation can not occur any more ($\chi N < 10$). Another limiting factor is the thermal decomposition temperature of the polymers, which is typically in the range of 300 to 500 °C. Rapid thermal processing (RTP) allows the sample to be quickly heated with an infrared light source and cooled by gas purging. A nitrogen atmosphere can be utilized to delay the onset of polymer degradation. The results from high-temperature (250–290 °C) RTP annealing studies have indicated faster coarsening kinetics during the first few minutes [78], [79]. Grain sizes of $\xi \approx 500$ nm have been obtained in RTP above 300 °C in under 100 s. Another similar rapid thermal treatment relies on microwave heating, which can either be done dry [59] or combined with solvent vapour exposure [80].

A third thermal treatment worth mentioning is zone annealing. In zone annealing a heated filament or a laser-line is scanned across the sample to induce a moving temperature gradient. It's theorized that the in-plane thermal gradient promotes rapid grain growth and that the movement of the thermal field can be used to align BCP structures in a preferred direction [71]. Cold zone annealing (CZA), where the temperature remains below T_{ODT}, has been shown to also control the orientation (parallel vs. perpendicular) of the BCP patterns via the sharpness of the temperature gradient [81]. CZA can yield a significant enhancement of the ordering kinetics compared to conventional oven annealing ($\alpha \approx 0.46$) [82]. Even faster assembly can

be achieved with laser zone annealing (LZA), which creates extreme temperature gradients ($T > T_{ODT}$) using laser sweeping. According to Majewski and Yager, LZA can anneal small samples in minutes and achieve effectively infinite grain sizes due to spontaneous alignment of the in-plane BCP cylinders along the sweep direction [72].

Thermal annealing methods have been extensively used for assembling PS–PMMA patterns. Unfortunately, some polymer systems are not so well-suited for thermal methods. For many high-molecular weight and high-χ BCPs thermal annealing isn't very effective or is too slow. High ODT temperatures, slow chain kinetics and low diffusivities hinder the self-assembly and poorly ordered patterns are produced. High-χ materials can also face difficulties in obtaining the perpendicular domain orientation due to the large surface energy difference between the blocks [83]. For these systems solvent vapour annealing is a promising alternative to thermal annealing.

3.2 Solvent annealing

Solvent vapour annealing (SVA) is the other annealing technique that can be used to self-assemble BCPs. In SVA the BCP thin films are exposed to a solvent vapour and the thin films swell with the uptake of solvent. The added solvent plasticizes the polymer by effectively decreasing the T_g of the system from ~ 100 °C to room temperatures or even below [84]. Polymer chain mobility and diffusivity is significantly increased and this can lead to a dramatically improved self-assembly time compared to thermal annealing. In addition to enhancing the self-assembly kinetics, the solvent can influence the interactions between the blocks. The solvent can screen unfavourable BCP–substrate interactions, change interface wetting preferences, influence the orientation of the BCP structures and even change the morphology of the BCP thin film. SVA is particularly useful for high-χ polymers where the blocks have high incompatibility and highly dissimilar surface energies. Solvent annealing can be done at room temperature or at elevated temperatures in a solvothermal process.

Self-assembly via solvent annealing is somewhat more complex process than via thermal annealing. Multiple factors affect the phase separation of a BCP during

solvent annealing. Yoon et al. [85] highlight three molecular weight-dependent factors that govern BCP self-assembly during SVA: 1) Solubility of both blocks in the selected solvent, 2) chain mobility in the solution and 3) the order–disorder transition concentration. The ODT concentration is a similar limit as the order–disorder transition temperature. When the solvent concentration in the thin film is too high the BCP will become disordered and the pattern morphology is lost. Additional factors that influence the self-assembly can be temperature [86], [87], processing history [88] and pattern confinement and commensurability [47], [89].

3.2.1 Solvent effects

The selection of the solvent is critical in SVA. To assess whether a solvent is suitable for the polymers, solubility parameters can be examined. Solubility parameters δ are factors that can be used to predict whether a polymer will be soluble in a certain solvent. Materials with similar solubility values are likely to interact with each other and form a mixture. From a thermodynamic point of view, mixing is described as

$$\Delta G_{mix} = \Delta H_{mix} - T\Delta S_{mix} < 0 \tag{3.1}$$

where ΔG_{mix} is the Gibbs free energy of mixing, ΔH_{mix} is the mixing enthalpy and ΔS_{mix} the mixing entropy [90]. For binary mixtures the Hildebrand equation states that the change in mixing enthalpy is

$$\frac{\Delta H_{mix}}{V_m} = \left(\delta_p - \delta_s\right)^2 f_p f_s \tag{3.2}$$

where V_m is the molar volume of the mixture, δ are the solubility parameters and f_p, f_s are the volume fractions of the homopolymer and the solvent [90]. For mixing to occur, the Gibbs free energy of the system must be negative (Equation 3.1). This means that the mixing enthalpy must be small. It cannot be negative since that would indicate that the mixing is an exothermic reaction, which is not the case with polymer dissolution. So in general, $\left(\delta_p - \delta_s\right)^2$ must be small for the components to mix well. Therefore a simple estimate can be made that if a polymer and a solvent have very similar solubility parameters, the polymer will be miscible in the solvent. If both BCP

blocks are well-miscible, the solvent is deemed neutral or near-neutral and it will swell both blocks in a similar manner. A selective solvent has a distinctive preference for one of the blocks and during solvent annealing this block will swell more.

It is possible to estimate the amount of swelling that the blocks will exhibit in a solvent vapour atmosphere. The Flory-Huggins theory of polymer solutions states that the swelling of a homopolymer depends on the vapour pressure P and the interactions between the solvent and the polymer as

$$ln\left(\frac{P}{P_s}\right) = \chi\left(\frac{d_0}{d}\right)^2 + ln\left(1 - \frac{d_0}{d}\right) + \left(1 - \frac{V_s}{V_p}\right)\frac{d_0}{d} \tag{3.3}$$

in which P/P_s is the ratio of the partial pressure of the solvent in the annealing chamber to the equilibrium (saturation) vapour pressure [91], [92]. The equilibrium vapour pressure is temperature dependent and can be calculated using the semi-empirical Antoine expression. The film swelling is given as the ratio of the original film thickness d_0 to the swollen thickness d. The V_s and V_p are molar volumes of the solvent and the polymer. Lastly, χ is the Flory-Huggins interaction parameter between the polymer and the solvent. The polymer–solvent interaction parameter χ relates to the Hildebrand solubility parameters:

$$\chi = \frac{V_s}{RT}\left(\delta_s - \delta_p\right)^2 \tag{3.4}$$

where δ_p and δ_s are the solubility parameters of the polymer and solvent respectively [33]. The temperature T is given in Kelvins and R is the molar gas constant. Tabulated χ values for common polymer–solvent pairs can be found in the literature [90].

In block copolymer systems the addition of solvent screens unfavourable interaction between the blocks. Polymer–polymer interactions are basically ”diluted” by the solvent. The diluted interactions are described using an effective interaction parameter χ_{eff} [35] instead of the normal Flory-Huggins parameter χ as

$$\chi_{eff} = \chi\phi^{\alpha} \tag{3.5}$$

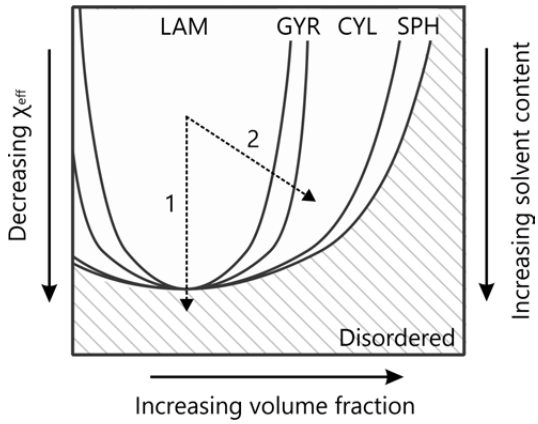

Figure 3.1 Schematic phase diagram depicting the effect of BCP swelling in neutral (line 1) and selective (line 2) solvents. As the solvent concentration is increased, the selective solvent changes the relative volume fraction of the blocks shifting the morphology from lamellar to cylindrical. Excessive addition of solvent will result in the BCP becoming disordered.

where $\phi = d_0/d$ is the polymer concentration in the swollen film, χ is now the polymer–polymer Flory-Huggins interaction parameter and α is a scaling exponent. Past studies have shown the exponent α to be in the range of 1.2 to 1.6 [35], [93].

The phase behaviour of block copolymers solvated in neutral solvents has been approximated to follow the melt phase behaviour depicted in the theoretical phase diagram (Figure 3.1), although some of the phase transition boundaries may be shifted [35], [94]. In the phase diagram the degree of segregation parameter χN is then replaced by $\chi_{eff}N$ (or $\chi\phi^{\alpha}N$). Self-assembly in the solvated state therefore depends on χ, N, f and also the solvent concentration and selectivity. Interestingly, the solvent can be utilized to change the morphology of the BCP. A selective solvent will swell one of the blocks more than the other and thus the relative volume fraction f of the blocks will change. The effects of selective and non-selective swelling are illustrated in Figure 3.1 with two annealing pathways. It is possible to swell a lamella-forming BCP with a neutral solvent and achieve lamellae (Figure 3.1 Line 1) or use a selective solvent and obtain cylinder patterns (Line 2). Multiple morphologies and different pattern orientation have been achieved in thin films annealed in various solvent vapours [95]–[97]. It is even possible to reversibly switch between different morphologies by annealing in alternating solvents [98]. Our group has achieved cylinders, lamellae and inverted cylinders from a 27.2–11.7 kg/mol polystyrene–polydimethylsiloxane (PS–PDMS) polymer using selective and non-selective solvents [99].

3.2.2 Static solvent annealing

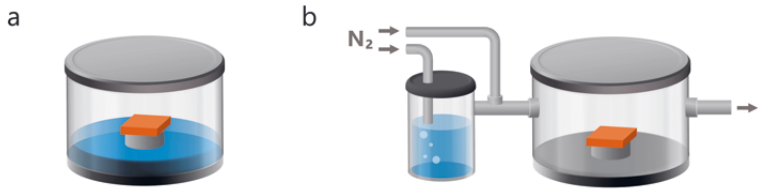

Figure 3.2 A schematic of two different types of solvent vapour annealing set-ups. (a) "Static" annealing in a closed jar and (b) "Flow" annealing where the solvent vapour is delivered into the chamber using a carrier gas flow.

The simplest realization of solvent vapour annealing is a sealed chamber that contains both the sample and a solvent reservoir (Figure 3.2a). The solvent saturates the atmosphere in the chamber and the BCP film swells with the solvent. There is no direct control over the film swelling so the annealing process is managed indirectly through the volume of the chamber, amount of solvent in reservoir, choice of solvent, solvent leak rate, annealing time and temperature [83], [100]–[103]. These factors affect the vapour pressure inside the chamber and hence the swelling of the thin film. In practice, the sample is exposed to the solvent vapour for a certain amount of time and then the film is deswelled either quickly by opening the chamber or slowly by letting the vapour leak out. The removal of the solvent vitrifies the polymer film.

Despite the apparent simplicity of SVA, controlling the process has proven to be very difficult. Even small changes in the laboratory environment may change the outcome of the annealing. Sinturel et al. [104] utilized *in situ* grazing incidence small angle X-ray scattering (GISAXS) to monitor morphology changes during static solvent annealing. Film thickness was monitored via ellipsometry. The study showed that BCP thin films began swelling immediately after solvent vapour exposure and while 90 % of maximum thickness was obtained already within the first 10 minutes, the film reached a thickness plateau only after 30 minutes. During this small film thickness change between 10 min and 30 min, *in situ* GISAXS revealed transitions in the pattern morphology. The crux of static SVA apparatuses is that the swelling and deswelling of the film cannot be precisely controlled. Also, it is not feasible to routinely use GISAXS to identify when the BCP thin film reaches the desired pattern morphology since GISAXS requires a synchrotron light source. Moreover, experiments are highly

susceptible to changes in the environment such as humidity, room temperature fluctuations and seasonal changes [105], [106]. Especially temperature-control is an issue, since the saturation vapour pressure of the used solvents is often very sensitive to temperature changes. Thus a small change in temperature can result in a large change in vapour pressure leading to a change in the swollen film thickness. This makes reproducibility an issue. One other disadvantage of static SVA is that the annealing times are still long – ranging from a few hours to several days.

3.2.3 Vapour flow annealing

SVA systems have progressively evolved into more sophisticated devices when it was recognized that the annealing process must be monitored and controlled more precisely. Flow annealing devices use an inert carrier gas to deliver the solvent vapour into and out of the sample chamber (Figure 3.2b). Nitrogen bubblers are commonly used to generate the solvent vapour in an external solvent reservoir and flow meters or mass flow controllers regulate the gas flows. A gas stream saturated with the desired solvent is directed through the annealing chamber while the film thickness is monitored using spectral reflectometers or interferometers. By mixing the solvent rich gas with an inert gas the vapour pressure inside the chamber can be altered. In practice this has often been done by varying the flow rates of the saturated vapour stream and a second diluent gas stream [107]. The solvent removal is done by purging the chamber with an inert gas such as nitrogen. The manipulation of the flow rates provides some control over the swelling of the thin film but the maximum achievable vapour pressure is decreased due to the diluting nitrogen gas.

Flow annealing devices have enabled controlled annealing in mixed solvent vapours. An example of this are the works of Gotrik et al. [108] and Cushen et al. [109] where multiple solvent reservoirs were added into the input gas line in order to mix solvent vapours and experiment with selective and non-selective swelling and the resulting morphologies. Similar methods have then flourished in studies concerning quenching and deswelling conditions [106], [110], [111], directed self-assembly [93], and polymer swelling dynamics [112]. Most of the devices have controlled the vapour pressure and the subsequent film swelling through flow rates and gas mixing but there are a few exceptions. Lundy et al. [113] and Stenbock-Fermor et al. [114] combined flow control with a temperature differential between the heated solvent and the heated sample.

Solvothermal annealing and temperature-control have been recognized in the field as promising ways to enhance self-assembly kinetics and reduce variations in the annealing results due to varying ambient temperatures. The downside of heating the solvent is that also everything else, the chamber walls, gas feedthroughs, pipes and the sample stage have to be heated above the temperature of the solvent to prevent solvent condensation and a subsequent drop in the vapour pressure [113].

There has been an evident need for precision control of the SVA process and the swelling of BCP thin films. During recent years, computer-controlled SVA devices have been proposed by a few research groups. Jin et al. [105] presented a computer-controlled SVA apparatus that had a temperature-regulated annealing chamber, mass flow controllers for the solvent lines and laser reflectometry for the film thickness. The film thickness monitoring was linked to a feedback control loop, which enabled real-time computer control of the solvent vapour flow rate and therefore the swelling of the film. Film swelling, deswelling, dwell time and purging could be regulated. The previously mentioned thermoregulated SVA device also contained computer-control over the device temperature but it lacked real-time film thickness monitoring [113]. One of the most elaborate SVA systems was presented a couple of years ago by Nelson et al. and it featured computer-controlled pneumatic inlet and outlet valves which control the film swelling [115]. The inlet/outlet flow rate variation appears to be a somewhat faster and more precise control mechanism than the typical flow control via nitrogen dilution.

3.3 Important factors in solvent annealing

The recent developments in SVA technology have significantly contributed to the understanding of what occurs during solvent annealing and how different factors may affect the outcome. It's been long known that annealing in different solvents causes differing pattern morphologies to appear and that the annealing time is somehow critical. Controlled SVA combined with *in situ* GISAXS measurements has shed some more light on why some factors are more important than others in the annealing process. It has been identified that the swelling ratio and the solvent removal rate are two very critical parameters that affect the periodicity of the pattern, the long-range order and the preservation of the morphology. In a study by Gu et al.

[116] the average grain size of PS–P2VP was seen to increase as the film swelling ratio (SR) was increased. The largest grains were obtained when the SR was close to the order-disorder transition. Baruth et al. came to similar conclusions using another high-χ BCP, polystyrene–polylactide [117]. Furthermore, order-order or order-disorder transitions have been identified to occur at very precise swelling ratios [98], [116].

Solvent removal and its effects on morphology has been one much debated factor throughout the years and its role appears to be quite complex. It is assumed that upon fast drying the ordered structures obtained in the swollen state contract in the out-of-plane direction, but that the lateral morphology is essentially preserved [104]. This type of film quenching has been a commonly accepted method for "freezing-in" the obtained morphology, although the compression of the film may also cause restructuring of the domains [98], [118]. Slow solvent removal has sometimes been credited for changing the orientation of BCP cylinder morphologies [111]. Some studies report no orientation changes but note a slight increase in the pattern periodicity likely because the slow solvent removal gives more time for the BCP molecules to respond to unfavourable molecular interactions and film commensurability issues [119].

Solvent evaporation from a fully disordered state acts differently. Instead of preserving the disordered state, ordered morphologies can form during solvent removal and the removal rate affects the morphology and its orientation [73], [120]–[122]. It has been theorized that pattern nucleation begins at the film surface when the local solvent content falls below the order-disorder concentration [73]. Studies seem to agree on that the nucleated morphology propagates from the surface into the film as a front. It has been noted for thick films, that the ordering can progress partway into the film but not necessarily all the way down to the film-substrate interface [73], [117].

4 DEVELOPMENT OF CONTROLLED SOLVENT ANNEALING DEVICE

Solvent vapour annealing of block copolymer thin films is a complex process and it can be influenced by many environmental factors. A wide variety of solvent annealing devices have been developed but comparison between these SVA studies is difficult. This is mainly due to the diversity of the SVA processes and varying practices in reporting. Critical SVA parameters such as the swelling ratio or the swelling and deswelling rates are not always mentioned or they are reported in various formats (e.g. time, nitrogen flow rate, film thickness or partial vapour pressure). Environmental factors such as humidity, temperature, or solvent purity are not or cannot always be controlled. These factors make it difficult to draw universal conclusions from the evidence or reproduce studies using another SVA setup. One of the main challenges in using block copolymers for lithography is acquiring the desired, defect-free pattern morphology in a repeatable way. The semiconductor industry has been focusing on thermal annealing since it appears more reliable and reproducible. However, application-wise there is a need for sub-10 nm as well as larger than 100 nm patterns, both of which cannot easily be obtained using thermal annealing.

There is clearly still a need to develop more sophisticated solvent annealing devices that can be used to self-assemble high-χ and high-molecular weight block copolymers. The key factor in these devices should be the precise control of both the annealing process and the environmental conditions. Key features should include fast modulation of the solvent content (SR) and the capacity for wafer-scale processing. Most flow SVA devices have miniature processing chambers that fit only centimeter-sized samples so that the film swelling would respond faster to changes in the gas flow. Still, it can take up to 15–30 min for the thin film to reach a steady swollen state

[108], [112], [119] and further changes implemented via gas-flow mixing take up to 3–5 min to occur [123]. Importantly, the total duration of SVA should be preferably minutes if not even seconds instead of hours.

The Nanophotonics research group at Tampere University has been developing a computer-controlled solvent annealing device for the past five years. Our aim has been to cut down the required annealing time and create an annealing process that can be precisely replicated. If the swelling and deswelling of the BCP could be repeated reliably, it could be possible to examine how isolated factors or parameters affect the produced BCP pattern.

4.1 SVA apparatus

The controlled solvent vapour annealing system that was developed and used in this work is illustrated in Figure 4.1. The annealing chamber was composed of three main parts: the lid, the body and the base. The lid had an embedded window for optical monitoring and feedthrough ports for other sensors such as temperature probes. The lid was fully detachable and was fastened to the chamber using quick screws. The custom-made aluminium body of the chamber had ports for electrical wiring as well as gas feedthroughs (Figure 4.2 A–D). The aluminium base plate was flat with a shallow groove around the circumference of the chamber. The input gas flow

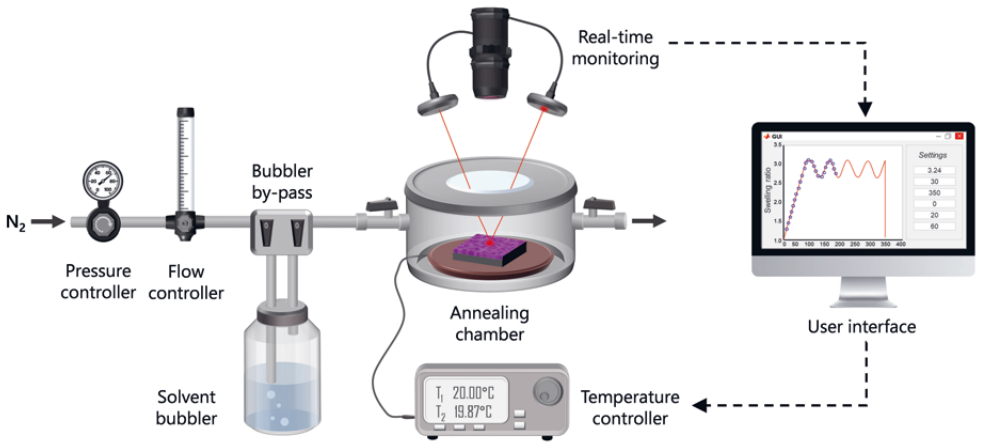

Figure 4.1 Schematic of the computer-controlled solvent vapour annealing system.

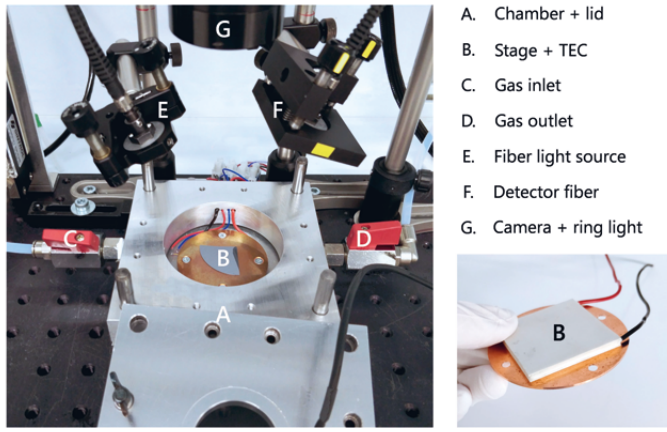

Figure 4.2 The solvent annealing chamber (A–D) with a silicon quarter wafer on the sample stage. The film thickness monitoring system (E–F) and the camera (G). The underside of a detached copper stage plate with the thermoelectric cooler module is shown in the inset (B).

could be fed in through the ring-structure in the base plate so that the solvent vapour would be distributed evenly inside the chamber. A copper plate stage was bonded to a thermoelectric cooler module (MultiComp, TEC 110 W, 12 A) and screwed onto the centre of the baseplate (Figure 4.2 B). The stage could then be heated or cooled by driving an electric current through the TEC element. The wiring of the TEC module and a temperature transducer (AD590MF) went through one of the feedthrough ports in the body and was fixed in place with epoxy. The base was screwed onto the body and sealed with O-rings. The internal diameter of the chamber was 75 mm ($V \sim 100\ \mathrm{cm}^3$) and it could accommodate semiconductor wafers up to 2 inches in size.

Solvent vapour was generated in a temperature-stabilized glass bubbler by bubbling dry nitrogen through the solvent reservoir. Later, the bubbler was switched to a larger, 100 ml bottle and a small-pore sparger head was added for more efficient vapour production. In a bubbler the small bubbles travel upwards and become filled with the solvent vapour as the liquid evaporates at the edge of the bubble. The vapour is released into the bubbler headspace above the liquid and from there the solvent rich gas can be extracted through another tube. The bubbler temperature was kept slightly below the ambient temperature to avoid condensation of the vapour.

The flow rate of the carrier gas was set using a gas pressure regulator and a variable area flow meter (Brooks Instrument Sho-rate). A constant nitrogen flow rate was

chosen that would ensure fast filling of the chamber but not so fast that the saturation level of the solvent rich stream would drop due to a too high feed rate. An adequate level of flow was assessed based on the shape of the swelling profile during SVA. The swelling of the thin films was not controlled via gas mixing so complex flow control systems were not needed. Nor was there a need for an additional nitrogen gas line for dilution. However, the solvent bubbler could be by-passed to quickly purge the chamber with pure nitrogen. The chamber also had valves on both the inlet and the outlet so that the vapour flow could be cut off to seal the chamber. The gas lines used 6 mm PTFE (polytetrafluoroethylene) and metal piping and connections were made using Swagelok tube fittings. Initially, there were some issues with the system leaking likely from one of the joints. Then all junctions and joints in the SVA apparatus were made leak-proof by either O-rings, epoxy or PTFE tape.

The SVA system was eventually moved into a semiconductor processing clean-room with controlled humidity and room temperature. This was done to minimize variations in the ambient conditions and mitigate process variation arising from external factors such as temperature fluctuations. For safety reasons the whole system was set-up in a fume hood to ensure that any leaked hazardous vapours were removed appropriately. A blast shield would also be recommended if the system does not have pressure relief valves or if any of the solvents are prone to forming potentially explosive peroxides. The tetrahydrofuran (THF) was periodically tested using peroxide indicator strips and was only acquired in bottles that had an inhibitor mixed in.

4.2 Sample monitoring

The samples were monitored during annealing via spectral reflectometry and optical imaging (Figure 4.2 E–G). The film thickness measurement setup consisted of a broadband, ultraviolet to near infrared (UV–NIR) light source (Ocean Optics DT-MINI-2-GS) that was used to illuminate the sample and a high-resolution UV–NIR spectrometer (Ocean Optics HR4000) that measured the reflected intensity as a function of wavelength. The light was collimated and focused using an optical fiber with a lens so that the spot size on the sample was approximately 4 mm. The reflected signal was collected at another optical fiber and fed into the spectrometer.

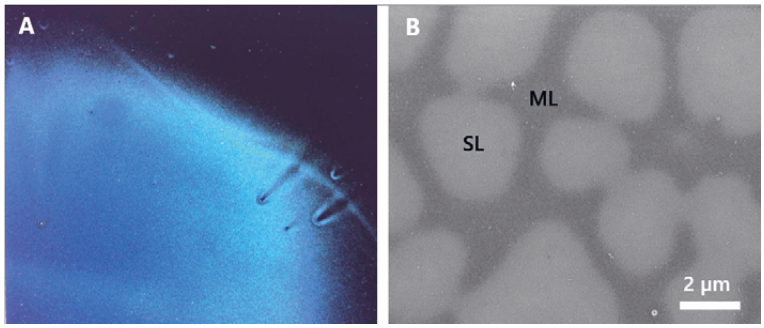

Figure 4.3 (a) Dark-field video image of an over-swollen BCP film. The blue colour indicates the unwanted formation of terraces in the swollen film. The comet-like features are defects from spin-coating. (b) An SEM image of the terraced area with thin (SL) and thick (ML) regions.

A video camera was positioned above the chamber so that the center position of the video image coincided with the reflectometry measurement spot. The samples were illuminated using a dark-field ring light. Alignment of samples could be done by checking their position in the video feed. The video feed also provided real-time information of the thin film quality. Figure 4.3a displays a still image of an over-swollen film that is experiencing terracing during SVA. The onset of terracing or dewetting could be seen as a change in the colour of the thin film. Figure 4.3b shows an SEM image of the terraced area. Due to terracing, the polymer in the thin film has been redistributed so that there are regions where the film is thinner (white regions) or thicker (dark regions). This could affect the morphology of the BCP film. The live video feed helped choose annealing parameters that didn't result in unwanted terracing.

Measurements as well as live video imaging was done through the window in the chamber lid, which caused some complications. Firstly, the viewport had to be made from fused silica glass instead of normal window glass to minimize the absorption of the optical signal. Furthermore, the reflectance measurement had to be done at a slight angle from the normal so that the overhead lights and the camera ring light would not interfere with the signal and oversaturate the spectrometer. The angle was taken into account in the film thickness calculations. Finally, a reference spectrum had to be taken before each annealing run to compensate for changing lighting conditions. A clean, uncoated piece of silicon was used as a reference sample. Data acquisition was initially done in the Ocean Optics SpectraSuite software but was

later moved to MATLAB with the help of MATLAB's Instrument control toolbox.

The thickness of a thin film can be calculated from the reflectance spectra if the optical constants, n and k, of the coating material and the substrate are known. The real part of the refractive index n and the extinction coefficient k are material-specific characteristics that vary with the wavelength of light. Optical constants can be derived form database values or from empirical relations such as the Sellmeier equation. It was assumed that the optical constants of the thin film would change with the addition of solvent. The change was calculated based on a Lorentz-Lorenz mixing rule, which is a frequently used theory for predicting the refractive index of a mixture from the indices and volume fractions of the components [124]. Refractive index values for P2VP or P4VP polymers could not be found in the literature, so the refractive index of polystyrene was used to represent the whole BCP. The indices of styrene and vinyl pyridine monomers are very similar, so the assumption was thought to be reasonable. A thin film model with a concentration dependent refractive index was fitted to the measured reflectance data to determine the film thickness during SVA. To confirm the validity and accuracy of the model, the dry thin films were routinely measured using both ellipsometry and the SVA reflectometry setup.

4.3 Operation

The operation of the SVA device included steps needed for the preparation of the setup followed by the actual annealing run. When first starting up the system, the light source and the camera ring light were turned on and let warm up and stabilize for about 15 min. The solvent reservoir was let stabilize to the desired operation temperature and nitrogen purging was turned on to flush the SVA chamber and the tubing clean. The gas flow rate was set to the desired fixed level (e.g. 100 ml/min) and a leak test was preformed to check that no solvent vapour would leak into the working environment later during the annealing. The reference Si piece was placed in the closed chamber and a dark spectrum and a reference spectrum were recorded. After this, the actual sample was positioned inside the chamber using the camera view for correct placement. The TEC plate under the sample was set to the initial temperature value and stabilized.

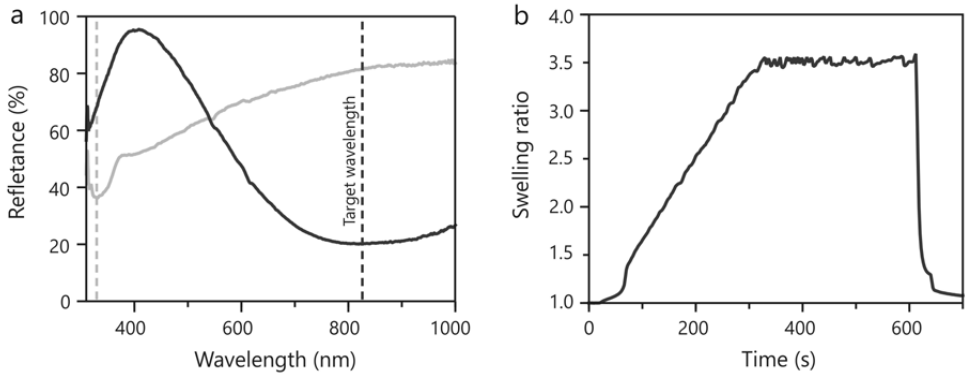

Figure 4.4 Manually controlled SVA annealing process in the early stages of the device development. (a) Reflectance spectra of a dry BCP thin film (grey) and a film swollen to a target thickness (black). (b) Resulting swelling profile.

At the start of the actual annealing, the solvent bubbler was switched on and the solvent rich vapour began to fill the sample chamber. The thickness change in the BCP thin film was monitored using reflectometry as explained in Section 4.2. Our approach was to control the swelling of the film via the temperature of the TEC plate. In general, a decrease in temperature led to an increase in film swelling while an increase in temperature acted oppositely. The temperature of the stage was gradually decreased until a desired swelling ratio was obtained. A high swelling ratio ($SR > 3$) could be achieved in minutes. The swelling of the thin film was kept at a constant level for 1–30 min (dwell time), after which the film was deswelled either by by-passing the bubbler and quenching with pure nitrogen or by temperature-controlled deswelling. After annealing the solvent stream was switched off and nitrogen purging was turned on (if not already) to ensure that the thin film would not re-swell. The sample was removed from the chamber immediately after annealing.

In the first version of the SVA device, the TEC plate temperature was changed manually. Sample monitoring was done by observing changes in the reflectance spectra. The desired level of swelling was obtained by aiming for a specific value of the first order minimum of the thin film reflectance (Figure 4.4a). After the annealing run, the exact swelling profile and film thickness changes were calculated from the recorded reflectance data. Understandably, the reproducibility of the manually controlled process wasn't exactly stellar, but an experienced operator could achieve a decent swelling profile in a reasonable time as seen in Figure 4.4b.

4.4 Implementation of feedback control

The next step was to automate the changing of the TEC plate temperature in order to achieve better reproducibility and eliminate user-related errors. The thickness calculation was made to operate in real-time. A wavelength range of 320–800 nm was used, which was mainly chosen because of the spectral output of the light source and the transmittance of the viewport window. A feedback loop was implemented that monitored the measured film thickness, compared it to a pre-determined setpoint and adjusted the TEC temperature accordingly.

This type of automatic steering is called Proportional–Integral–Derivative control (PID). PID controllers aim to minimize the error between the signal value and the setpoint. Here only the Proportional mode of control was needed meaning that the error was multiplied by a proportional constant, which then determined the magnitude of the temperature correction. The thickness of the thin film could be measured approximately every 30 ms but there was no point in making the P-controller change the temperature so often. Thus the control loop waited for a certain amount of measurement points before applying any corrections.

A graphical user interface (GUI) was designed around the MATLAB script for ease of use. Parameters such as the swelling ratio, dwell time and ramp up/down rates were typed into the GUI and a swelling profile was created. After the user had initialized the SVA system, inserted the sample in the chamber and defined the annealing profile, the rest of the annealing was controlled by the software. The user could monitor the progress in the GUI window. Figure 4.5a displays a typical annealing profile with a swelling regime (I), a steady state SR (II) and a quenching or deswelling regime (III). The temperature of the stage TEC plate was initially decreased during regime I and then maintained at a semi-steady state during regime II as depicted in Figure 4.5c.

Due to the precision and speed of the temperature control, fast swelling modulations such as sinusoidal change depicted in Figure 4.5b could be easily implemented. The TEC temperature set by the P-controller is shown in Figure 4.5d. A similar sinusoidal shape is seen but the temperature minimums correspond to the swelling maximums since decreased temperature increased the swelling. It is good to note that the temperature effect was extremely localized and that the majority of the chamber

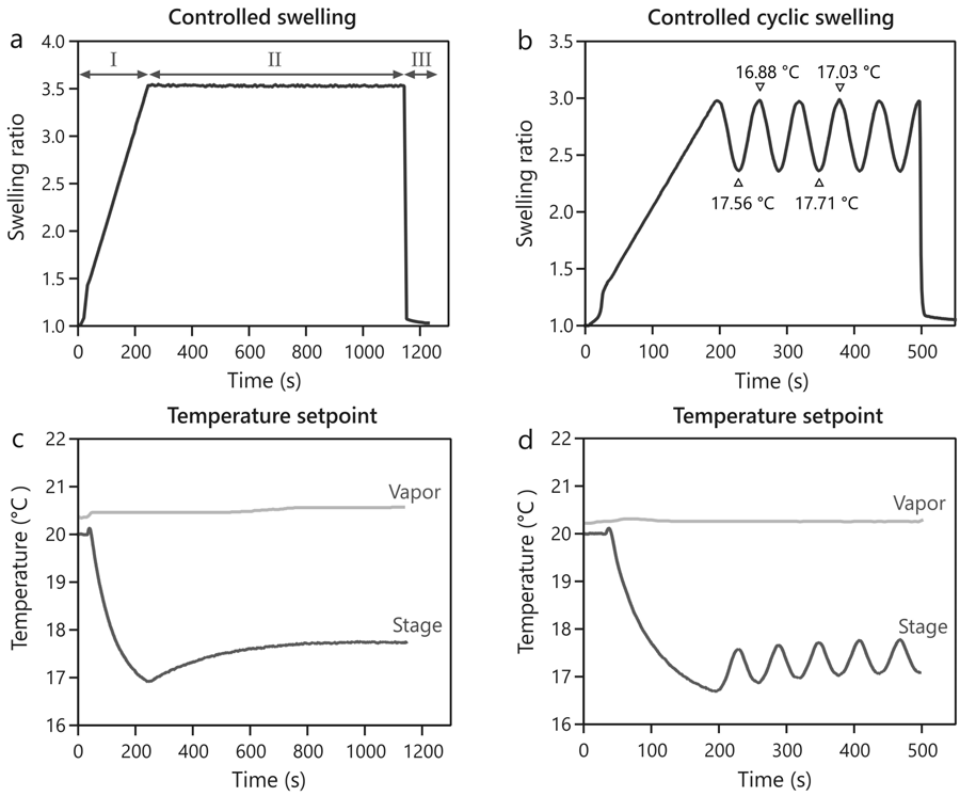

Figure 4.5 Precisely controlled swelling of a high-molecular weight PS-P2VP polymer in the SVA system. (a) Measured swelling profile with a solvent uptake regime (I), a dwell regime at a constant swelling ratio (II) and a quenching or controlled solvent removal regime (III). (b) Temperature-controlled cyclic swelling and deswelling during the dwell regime. The annotations show the temperature of the stage at selected points. (c,d) Setpoint temperature of the sample stage for (a) and (b). The temperature of the solvent vapour elsewhere in the chamber (approx. 1 cm above the stage) was largely unaffected.

and the majority of the solvent vapour were unaffected by the control system. To the best of our knowledge, the SVA system presented in **Publication III** is one of the most precise SVA systems so far and the first one to actually realize controlled cyclic swelling. Previously it has not been viable due to the slowness of the (flow) control systems.

4.5 Swelling control mechanism

The uptake of solvent in a polymer film is influenced by the vapor pressure. More precisely it's the vapour pressure ratio P/P_s, where P is the partial pressure of the solvent vapor present in the system and P_s is the saturation (or equilibrium) vapor pressure of the solvent. Figure 4.6a depicts the saturation vapour pressures of three different solvents and the effects of temperature. The depicted THF and acetone are both high vapour pressure solvents and have a strong temperature dependence at room temperatures. THF is a near-neutral solvent for PS–PVP and acetone is slightly PVP selective. Toluene has a lower vapour pressure and is slightly PS selective.

Figure 4.6b illustrates what happens to the swelling of polystyrene in THF vapour according to the polymer solution theory if the P/P_s ratio is changed by altering the temperature (Equation 3.3). The Flory-Huggins parameter for PS–THF was assumed to be 0.41 and an arbitrary THF partial pressure P was used for calculation purposes. As the temperature is decreased, the saturation vapour pressure of THF drops and the relative vapour saturation P/P_s subsequently increases. This in turn increases the film swellibility. The polymer becomes very sensitive to the P/P_s value close to the dew point (the temperature where the relative saturation is 100 %). Even small changes in the temperature in this range can result in large changes in the polymer

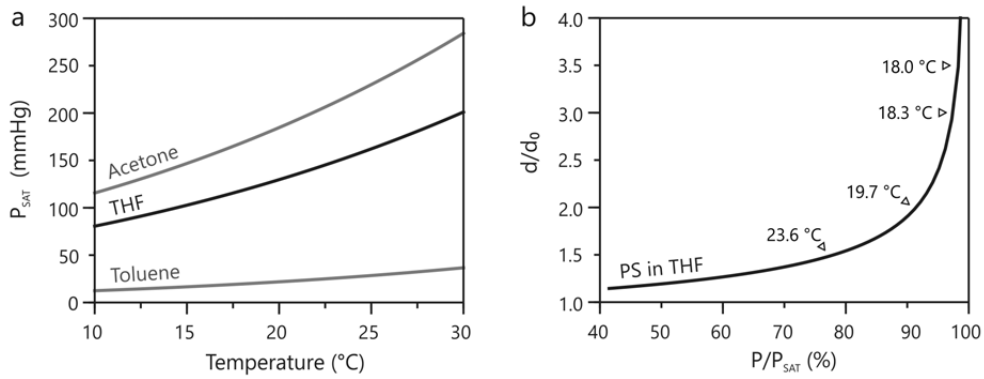

Figure 4.6 (a) The temperature dependent saturation vapour pressure curves of acetone, THF and toluene [125]. (b) Theoretical equilibrium sorption of THF in polystyrene at differing vapour pressure ratios P/P_{SAT} according to Equation 3.3. The thickness ratio d/d_0 is the swelling ratio of the thin film. The annotations show the temperature at selected points.

swelling behaviour. If the system temperature is decreased below the current dew point, the vapour will begin to condense into liquid matter.

The theoretical behaviour matched quite well with what was observed in the experimental swelling studies. The swelling of a thin film increased as the temperature of the stage plate was decreased. Thin films became very sensitive to temperature changes at large swelling ratios and a very responsive and accurate TEC plate system was needed. If a very thick copper plate was used as the sample stage, the swelling control became laggy and sluggish, presumably due to the slower heating and cooling of the plate. Fast swelling control was achieved with a 1 mm thick copper plate. Solvent could also be made to condense on the stage plate if the plate temperature was decreased low enough. It is important to note that the TEC plate temperature did not change the temperature of the whole chamber and that the vapour atmosphere further away from the sample was unaffected by the temperature changes as seen in Figure 4.5b, d. Overall the temperature changes during annealing were quite minute and the TEC plate temperature was typically in the range of 20 ± 4 °C.

4.6 Fabrication of block copolymer patterns

During my time at Tampere University, I've studied the self-assembly of PS–PVPs on various different substrates such as silicon, gallium arsenide, indium arsenide, indium tin oxide, glass substrates and metals. The publications included in this thesis deal with the patterning of (100) silicon wafers. The Si wafers were cleaned before use, but no neutral brush layers or polymer grafting was utilized. The BCP thin films were formed by spin-coating on cleaned quarters of 2-inch wafers. Usually the weight/volume concentration of the BCP solutions was 0.4–1.0 w/v %, which produced thin films with a thickness ranging from 15 nm to 50 nm. An ideal film thickness was $d < L_0$, which would help avoid the island/hole formation and promote a perpendicularly oriented pattern. After spin-coating, the thin films were baked on a hot plate to remove all residual solvent from the films.

Sample preparation turned out to be of great importance. If the spin-coating was non-uniform, the thin films would have some variations in the film thickness. This in turn could lead to thickness dependent morphology changes during annealing.

Non-uniform coatings would be formed for example if the casting solvent evaporated too quickly. The film would dry out before it had enough time to spread evenly over the wafer surface. Rapid evaporation is an issue especially with solvents that have a high vapor pressure, such as THF or acetone (see Figure 4.6a). A 7:3 mixture of toluene and THF was used as the casting solvent, since the solubility parameter of the mixture was close to that of PS–PVP and the evaporation rate of the solution was slowed down due to the presence of the low vapor pressure toluene. A closed-lid spin-coater was used, which further slowed down the evaporation of the solvent and improved the uniformity of the formed thin films. Debris on the wafer surface or in the casting solution could also cause non-uniform coatings. Therefore, the wafers were cleaned with care right before spin-coating and the casting solutions were mixed overnight and filtered through a 0.2 µm PTFE syringe filter before use.

The block copolymer thin films were annealed in the SVA device using various solvents such as THF, toluene, acetone and ethanol. THF was clearly the superior annealing solvent for achieving large grain sizes in high-molecular weight PS–P2VP thin films. Different swelling profiles were explored by varying the swell rate, the dwell time, the maximum swelling ratio, and the rate of deswelling. The aim was to find a good combination of factors that produced well-ordered, uniform patterns over the whole sample surface so that the BCP could be used as a template for lithography.

4.7 Characterization of patterns

The self-assembled block copolymer thin films were characterized using scanning electron microscopy (SEM). All SEM images of block copolymers were taken using a Zeiss Ultra 55 (Carl Zeiss AG) field emission SEM at 1.5–5 kV acceleration voltage. SEM provides qualitative information about the surface characteristics of the BCP thin films. An SEM image is formed by scanning a beam of electrons over the sample surface and recording the response at each raster point. The beam electrons hit the sample surface and interact with the sample atoms around the point of impact. There are two main signal sources for creating SEM images: secondary electrons (SE) and backscattered electrons (BSE). Topographic features, such as edges, tilted structures and small particles, produce a large amount of secondary electrons. The image formed from SEs is a pseudo-3D image of the surface topography of the sample. Backscattered

electrons on the other hand form images that depict the elemental composition of the sample since the generation of BSEs depends on the atomic number Z of the sample atoms. Heavy elements (high atomic number Z) produce many BSEs and vice versa. Scanning electron microscopy produces greyscale images where the dark and light areas correspond to the amount of detected SEs or BSEs. Image formation therefore requires the sample to have either topographic or elemental contrast. Untreated BCP thin films have neither of these. The thin film is flat and the pattern domains are elementally indistinguishable from each other since both polymers consist mostly of the same light elements (carbon, hydrogen).

Selective metal ion loading of PS–PVP structures was utilized for image contrast enhancement. The method can be used to selectively incorporate metallic species into the PVP domains via the nitrogen in the pyridine ring. The thin film is immersed in an aqueous, slightly acidic metal salt solution. In an acidic environment the PVP blocks become protonated and acquire a net positive charge. Therefore, selective metal loading can be done using anionic metal complexes, such as $[MCl_4]^{n-}$ (where M = Au, Pd, Pt), which bind via electrostatic interactions to the cationic PVP domains [126].

The wafers were dipped in aqueous solutions of $HAuCl_4$ (hydrogen tetrachloroaurate) and $Na_2[PtCl_4]$ (sodium tetrachloroplatinate) at an optimized molar concentration of 1–5 mM with 0.05–0.1 % HCl. The HCl concentration was kept intentionally low since higher concentrations resulted in ring-like patterns as the PVP chains exploded out from the cylinders. The uniformity of the obtained metal structures has been seen to depend on the immersion time and the metal salt concentration [46]. Using the aforementioned aqueous solutions, well-formed metal structures could be achieved in 10–15 min. A subsequent oxygen plasma treatment could be used to remove the polymer and reduce the metal salt into elemental metal. It was noticed that for SEM imaging purposes the plasma reduction was not necessarily needed since the metal salt doping already provided sufficient image contrast.

4.8 Image analysis

Image analysis was used to study the BCP cylinder patterns and determine factors such as periodicity, defects and the degree of ordering from SEM images. The pattern morphology analysis was performed with scientific imaging software ImageJ [127] and MATLAB R2015 (MathWorks Inc.). SEM images were first converted into binary black and white images by automatic thresholding. The binary images were then smoothed if outlier pixels needed to be removed. Particle analysis tools were used in ImageJ to measure the shapes in the binary images. The tool calculated the size, center coordinates and the number of objects in the image. Furthermore, the average cylinder size, standard deviation and cylinder circularity could be calculated.

For a more in-depth defect analysis the point coordinates were exported into MATLAB. A custom-made script performed a Voronoi partition and a nearest neighbour analysis on the coordinate data to determine the lattice defectivity. A cylinder with 6 neighbouring points represented a perfect hexagonal lattice while any other number of neighbours was considered a lattice defect. Average lattice periodicity and the standard deviation was also simultaneously calculated. Figure 4.7 outlines the different stages of the image analysis process.

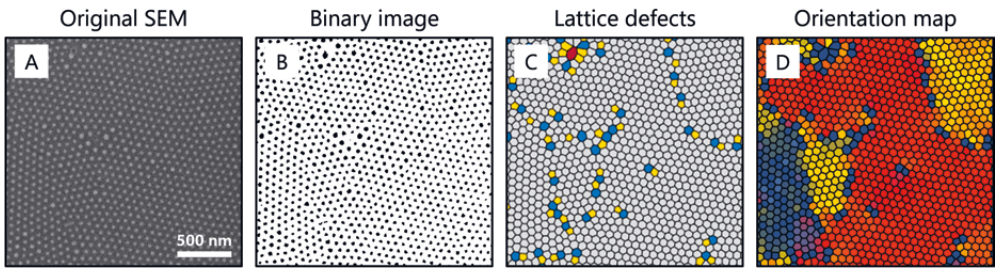

Figure 4.7 Illustration of the different steps in the image analysis of PS–P2VP 185–73 kg/mol patterns. (a) SEM image of the Pt-doped cylinder morphology. (b) Conversion of the SEM image into a black and white image for particle counting. (c) Division of the image into Voronoi cells and identification of lattice defects. (d) Mapping of the orientation of the Voronoi cells as an indicator of BCP grains.

4.9 Effects of controlled solvent annealing

The self-assembly of a variety of PS–P2VP and PS–P4VP polymers was studied using controlled solvent vapour annealing. The molecular weights of the tested polymers ranged from 458 kg/mol to 15 kg/mol. Not all of them could be made to form patterns with long-range order. Some of the high-molecular weight ones, like the 458 kg/mol BCP, were problematic to dissolve using THF/toluene. Thin films made from those solutions tended to have agglomerates of polymer in them and well-ordered patterns would not form even after extended annealing. The lack of success was likely due to a combination of extremely slow chain kinetics and poor solvent compatibility. Better assembly could have possibly been achieved with solvents such as chloroform but those were deemed too unsafe to use in the annealing system. Some of the low-molecular weight BCPs, such as the 15 kg/mol one, formed only micelle-like patterns. It is possible that the selected swelling parameters pushed the polymer always into the disordered phase past the ODT concentration limit (see Figure 3.1).

Publication III reported the effects of some selected annealing parameters on the self-assembly of high-molecular weight PS–P2VP polymers. The main parameters examined were the thin film swelling ratio (SR) and the dwell time at a fixed SR value. The ramp up rates and the ramp down rates were also examined for controlled film swelling and deswelling. No changes in the orientation of the domains were observed related to the ramp rates. Most polymers had a processing window for the optimal swelling of the thin film as illustrated in Figure 4.8. If the SR value was too low, patterns would be badly ordered likely due to low chain mobility. On the other hand, if the SR value was too large, the thin film would begin to experience dewetting or terracing. This would lead to thin films with mixed domain orientations. The largest grain sizes were observed when the SR was large, but still slightly below the terracing limit. On unmodified Si substrates the terracing often began when the swollen film thickness became a multiplication of the pattern periodicity ($d_{max} < 2L_0$). Similar processing windows have been observed in previous BCP annealing studies but in these the upper swelling limit has been the ODT concentration [117], [119].

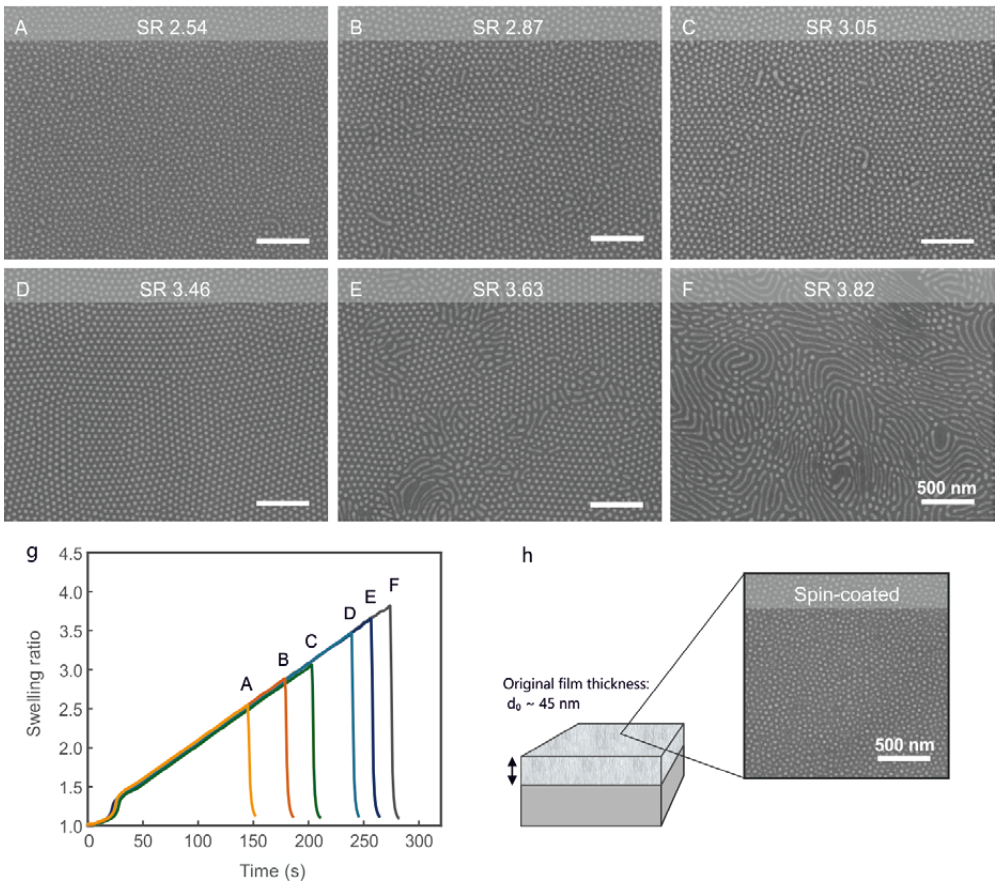

Figure 4.8 Controlled solvent vapour annealing of 188 kg/mol PS–P2VP in THF at increasing swelling ratios. (a)-(f) SEM images of the annealed BCP thin films. (g) Swelling profiles of the thin films A–F. The BCPs were immediately quenched when the desired SR was reached. (h) Before annealing, the thin films displayed a disordered morphology. PVP domains were doped with Pt for SEM imaging. Scale bars 500 nm. Adapted from **P3** with permission from the Royal Society of Chemistry.

At first glance the SR values look to be quite large compared to previous SVA studies where the SR has been monitored [105], [116], [117], [119]. The optimal processing window for the 188 kg/mol PS–P2VP presented in Figure 4.8 was approximately 3.2–3.5 meaning that the solvent content in the film was over 70 %. One explanation arises from the high χN value of these polymers. A high-χN BCP can withstand exceeding amounts of solvent before reaching the order–disorder limit, χN < 10.5, and falling into disorder (see Equation 3.5). There is not much data available on the swelling of high-molecular weight BCPs in the literature. Many previous studies have used

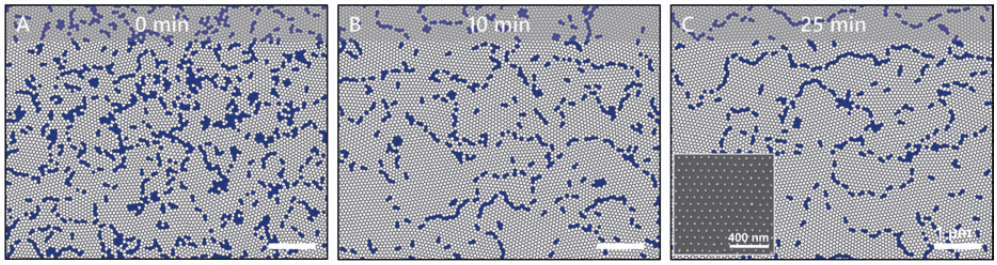

Figure 4.9 Colour maps of the grains in cylinder-forming 258 kg/mol PS–P2VP thin films after annealing in THF with a dwell time of (a) 0 min, (b) 10 min, and (c) 25 min. The swelling ratio was held constant at 3.53 during the dwell regime. The grain boundaries (defects) are depicted in blue while a perfect hexagonal lattice is in grey. Adapted from **P3** with permission from the Royal Society of Chemistry.

unmonitored static SVA. However, a couple SVA studies of high-molecular weight PS–PMMA do support the findings that large SR values are needed in the assembly of > 200 kg/mol BCPs and that well-selected SR values can be used to induce accelerated ordering in the early stages of annealing [6], [128]. It must be noted though that there is a risk of dewetting occurring at large swelling ratios during extended annealing [128].

One of the aims of this work was to reduce the required annealing time. The effect of the annealing time at constant SR was studied in **Publication III**. Colour maps in Figure 4.9 illustrate the improvement of the long-range order and the elimination of lattice defects in cylinder-forming (258 kg/mol) PS–P2VP thin films after annealing in THF for a predetermined dwell time. The pattern order could be improved by extending the annealing time. However, a decent grain size could be obtained already after a dwell time of 3 to 10 min, depending somewhat on the molecular weight of the polymer. High-molecular weight polymers were slower to achieve long-range order than short chain polymers, which is quite understandable. Most of the time the whole annealing process lasted less than 15 minutes. This is significantly better than usual. The annealing time in many static and flow SVA systems has been in the timescale of hours. Unexpectedly, micron-sized grains could be obtained also with a zero-minute dwell time if the SR value was large enough (see Figure 4.8d). In other words, it was sufficient to merely swell the film up to the target level and then immediately quench it. Potentially, this could be used for extremely quick solvent vapour annealing that could be done in minutes or even seconds.

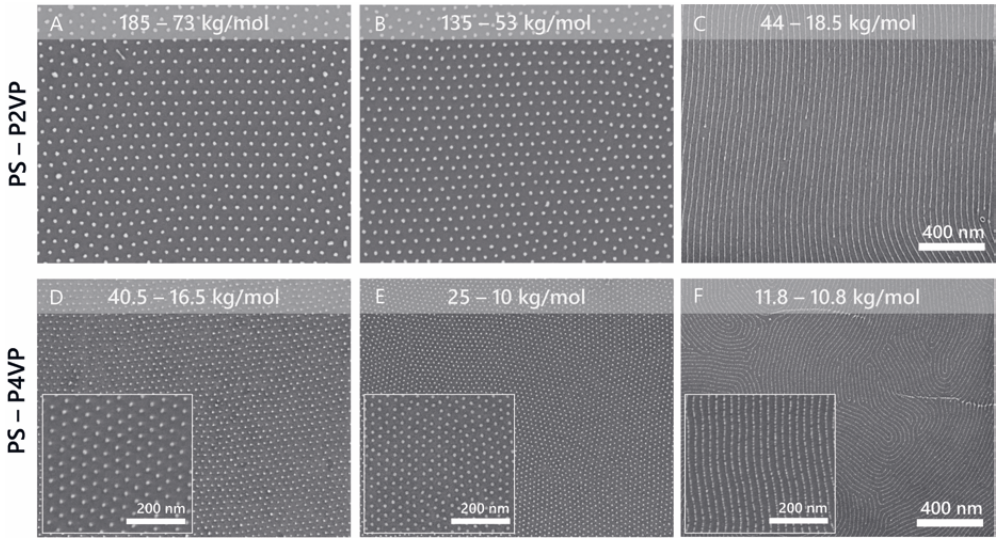

Figure 4.10 SEM images of self-assembled high-molecular weight and low-molecular weight PS–P2VP (a-c) and PS–P4VP (d-f) thin films on silicon. Patterns were obtained using controlled SVA in THF with a dwell time of 10 min. The swelling ratios for the different BCPs during the dwell regime were (a) 3.53, (b) 3.42, (c) 2.43, (d) 3.32, (e) 2.40 and (f) 2.75. For imaging, the PVP domains were doped with Pt or Au and the BCP was removed with oxygen plasma.

As previously mentioned, a range of PS–P2VP and PS–P4VP polymers with varying molecular weights were tested during the thesis project. Figure 4.10 shows a collection of successful PS–PVP patterns achieved using controlled solvent vapour annealing in THF with a 10 min dwell time. High-molecular weight cylinder-forming PS–P2VP 185–73 kg/mol (A) and 135–53 kg/mol (B) formed perpendicular cylinders with an approximate periodicity of 79 nm and 74 nm, respectively. The perpendicular domain orientation was obtained by using BCP films that were thinner than the periodicity of the pattern. The aforementioned BCPs could also be made to form in-plane cylinders by altering the original film thickness. PS–P2VP 44–18.5 kg/mol (C) assembled only into in-plane cylinders that were parallel to the Si substrate resulting in line structures with a periodicity of 38 nm. Perpendicular cylinders could not be achieved using THF annealing. Further research would be needed to see whether the orientation could be changed by using mixed solvents or substrate functionalization.

All other low-molecular weight polymers available during the thesis project were PS–P4VPs. The PS-P4VP 40.5–16.5 kg/mol and 25–10 kg/mol polymers illustrated in Figure 4.10 (D) and (E) produced perpendicularly oriented cylinders with periodicities

of 43 nm and 34 nm when annealed in THF. The lowest molecular weight polymer that was successfully self-assembled was lamella-forming PS-P4VP 11.8–10.8 kg/mol (F). This BCP could be used to obtain sub-10 nm pattern features (L_0 = 15nm). Perpendicularly oriented lamella were obtained when the original film thickness was smaller than the periodicity of the pattern. Thick films of PS–P4VP 11.8–10.8 kg/mol resulted in stacked in-plane lamella sheets.

5 FABRICATION OF PHOTONIC NANOSTRUCTURES

Micro- and nanofabrication technologies have been utilized for decades to mass produce integrated circuits for various consumer electronics devices. The same methods are being used in the manufacturing of optoelectronic devices such as semiconductor lasers and light-emitting diodes or nanophotonic materials such as anti-reflection coatings, metasurfaces and photonic crystals. Different lithography techniques can be used to create patterns with a feature size ranging from a few nanometers up to several millimeters. Photolithography or nanoimprint lithography are examples of techniques that use photomasks or moulds to fabricate patterns over large surface areas simultaneously. The fixed mask pattern is replicated in one exposure step onto a film of polymer (i.e. resist) that is on the substrate. Other techniques such as electron beam lithography and focused ion beam milling can produce patterns by direct-writing. Any type of arbitrary pattern can be drawn onto the resist/substrate and no pre-made photomask is needed. The price for the added flexibility of such methods is lower throughput.

Self-assembly methods fall somewhere in between the aforementioned lithography techniques in terms of pattern production. Self-assembly can produce patterns over large surface areas simultaneously. However, the pattern shapes that it can produce are somewhat restricted due to the nature of self-assembly. Self-assembly techniques can be thought to include block copolymers but also colloidal lithography where nano-objects such as spheres are assembled into tightly packed layers [129]. By definition, self-assembled monolayers (SAMs) can also be included, although the actual patterning does require the use of photolithography, dip pen lithography or microcontact printing [130]. Block copolymer patterning is often used in conjunction

with other lithography techniques in directed self-assembly (DSA). DSA uses either chemical pre-patterns (chemo-epitaxy) or topographic pre-patterns (graphoepitaxy) made by other lithography methods as templates that guide the self-assembly of the polymer into the desired pattern geometry [131].

Lithography methods are usually combined with other material deposition and etching techniques to fabricate nano- and microstructures with the desired functionality. In complex structures the process is actually a cycle of multiple patterning, material addition and removal steps. Material can be added by depositing thin films using vapour deposition or evaporative methods, solution growth, spin-on methods or epitaxy. Subtractive methods remove material either selectively or uniformly. Typical methods include wet chemical etching, plasma etching, sputtering and various milling and polishing methods.

In the following chapter the fabrication of photonic nanostructures using BCP lithography is discussed. The optical properties and the applications of the produced nanomaterials are discussed later in Chapter 6.

5.1 Pattern preparation

In this work, block copolymers were used as templates for the fabrication of inorganic nanostructures. The polymer patterns were formed by PS-PVP self-assembly using solvent annealing as was described in Chapter 4. The patterns were then turned into a thin film mask by removing the PVP domains, leaving behind a patterned PS thin film. The process is analogous to resist development in traditional photolithography. During immersion in a PVP selective solvent, the PVP domains are dissolved and as a consequence, pores or open structures are created in the film. As the thin film is dried, the PVP chains collapse on the surface leaving the pores open [132]. PS structures remain mostly unchanged during the process. The swelling-induced surface reconstruction process is non-destructive and reversible and it has often been used with PS-PVP polymers [47], [51], [133].

In the beginning of the study the reconstruction treatment was done in ethanol at room temperature for 30 min. This approach produced well-defined holes (cylinders) or lines (lamellae) in the tested thin films (Figure 5.1). In the interest of reducing

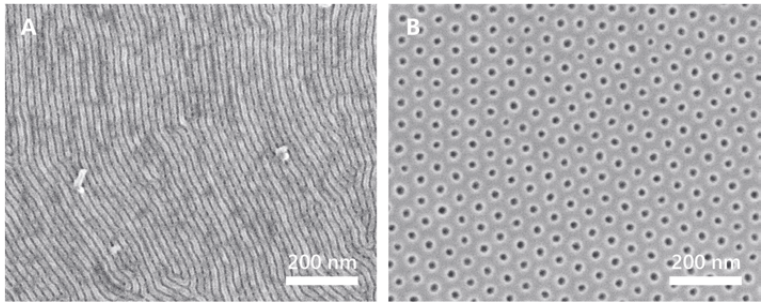

Figure 5.1 SEM images of ethanol reconstructed BCP thin films where the PVP domains have been displaced. (a) Perpendicular line structures formed from lamella-forming PS–P4VP 11.8–10.8 kg/mol. (b) Perpendicular hollow cylinders formed from cylinder-forming PS–P2VP 135–53 kg/mol.

the processing time, shorter treatment times were tested. It was discovered that the immersion time could be safely reduced to 10 min at room temperature and well-defined pattern masks could still be obtained. The shortest treatment that was tested was spin-coating the thin film samples with ethanol for 60 s. For some polymers such as the large molecular weight ones the spin-coating approach worked well. However, occasionally some of the PVP structures would not open up properly during the brief spin-coating and thus the use of this method was discontinued.

Later on, it became important to obtain closely spaced, large holes from cylinder-forming BCPs. The size of the BCP domains is mainly defined by the molecular weight of the polymer. If the molecular weight is increased, the cylinder size increases but so does also the distance between the cylinders (periodicity increase). A technique was adopted from Yin et al. [51] where heated ethanol was used to slightly increase the pore size. The ethanol bath was heated to 30 °C, 50 °C, 60 °C or 65 °C and the samples were immersed in the bath for 2–15 min. The 30 °C and 50 °C treatments produced acceptable results. Temperatures of 60 °C or higher caused the thin films to deform or partially delaminate from the substrate. Yin et al. [51] noticed similar detachment issues for ethanol treatments at 75 °C for 3 h. In accordance with the other study, it was concluded that the immersion time did not significantly influence the pore size. In this case, a 2 min immersion produced just as good structures as a 15 min immersion.

5.2 Dry etching

Pattern transfer of the BCP structures was done using reactive ion etching (RIE). Plasma etching is a technology where reactive gaseous molecules are utilized to remove material from a thin film or substrate. In a RIE chamber the plasma is produced between parallel plates by applying radio frequency (RF) power (13.56 MHz) to the top electrode. The formed electric field ionizes the gas molecules and a DC self-bias pulls the gas species towards the bottom electrode and the substrate surface. The molecules react with the substrate material sputtering off chunks of matter or producing volatile compounds that desorb. The etch is thus typically a combination of chemical reactions and physical ion bombardment. The majority of dry etching processes for silicon and silicon dioxide are based on chlorofluorocarbon plasmas and the fundamentals of these etch chemistries are well documented [134], [135]. To summarize briefly: the Cl^- or F^- ions react with Si on the substrate surface forming volatile reaction products ($SiCl_4$ or SiF_4) that can be then vaporized and transported away from the surface. Fluorine-based plasmas are generally used for isotropic etching whereas chlorine-based are good for anisotropic etching.

5.2.1 Fabrication of nanohole arrays

The fabrication of monodisperse nanoholes in silicon was one of the key concepts in this thesis and it was used in both **Publications I** and **II**. Hexagonally ordered arrays of holes with varying diameters and depths were etched into silicon using cylinder-forming PS–P2VPs. Dry etching of the Si samples was done using a $SF_6 + O_2$ gas mixture with flow rates of 12 + 9 sccm in a PlasmaLab System 100 (Oxford Instruments) reactive ion etcher. The recipe was selected based on the available process gases and the capabilities of the system. It was known from previous experience that the gas flow ratio was suitable from shallow etching of Si. The chamber pressure was kept at 30 mTorr. The recipe was further optimized for BCP masks by tuning the applied RF power. As the RF power is increased the amount of free fluorine atoms in the plasma increases, which leads to increased Si etch rates [136]. This can however also increase the etch rate of the polymer mask. It was discovered that while 80 W of RF power was insufficient to etch Si, RF values 155–170 W were acceptable.

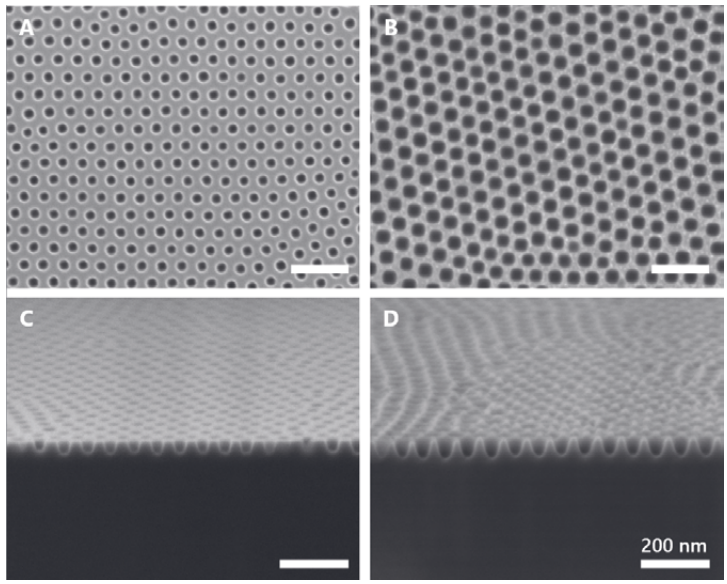

Figure 5.2 SEM top-view (a,b) and cross section view (c,d) of nanoholes in silicon. The difference in hole size was obtained by changing the dry etching time. Adapted with permission from **P1**. Copyright 2017 American Chemical Society.

A more critical parameter turned out to be the etch time. Polymer-based, organic etch masks are normally relatively thick since dry etching also etches away some of the mask material. The resist thickness and the etch resistance therefore puts a limit to the etch depth that can be achieved in the substrate material. Once the resist layer becomes too degraded, the etch begins to eat away also the patterns that were transferred onto the substrate. At 160 W RF power the etch rate of the BCP mask was approximately 90 nm/min. For a 50-nm-thin BCP film the maximum etch time would therefore be around 33 s, after which over-etching of the structures would occur. Over-etching was in fact observed in some of the experimental samples.

In **Publication I** a simple method was used to control the size of the etched pores in silicon. It was discovered that by simply extending the etching time, the pores would grow both laterally and horizontally since the fluorine-based etching was rather isotropic. The only limiting factors were the periodicity of the pattern and the thickness of the BCP thin film. The BCP periodicity limited the size of the pores since obviously neighbouring patterns would begin to merge together if the diameters grew too large. The thin film thickness limited the etch time since once the polymer was gone, the Si would begin to etch uniformly destroying the pore patterns. Using

a 188 kg/mol PS-P2VP pattern with a periodicity of 74 nm, the average diameter of the holes could be varied up to about 58 nm. A 57 kg/mol PS-P4VP pattern with a periodicity of 43 nm could produce hole diameters up to 31 nm. Figure 5.2 illustrates the nanohole structures achieved using a same 188 kg/mol BCP mask layer but with either a short etch time (left) or a longer etch time (right). The applications of nanohole arrays are described later in Chapter 6.

5.3 Template-stripping

Template-stripping is a thin film fabrication method that produces atomically flat and smooth metal surfaces [137], [138]. The procedure takes advantage of naturally flat surfaces such as polished silicon or mica, which are used as templates. A metal layer is deposited onto the template and due to poor adhesion, the deposited material can be peeled off revealing the bottom surface of the metal layer, which is then ultraflat. Gold is a popular material due to its weak adhesion to Si, good stability, advantageous plasmonic properties and its ability to bind a variety of biomolecules. Template-stripped metals have originally been used as substrates for studying biomolecules and self-assembled monolayers with scanning probe microscopy methods [139]–[141]. In addition to gold, the method has also been applied to platinum and palladium [139], and plasmonic metals such as silver, aluminium, and copper [142]. Noble metals work well, but reactive metals tend to bond too well to the Si template for the stripping method to work. One workaround is the deposition of a low surface energy release layer in between the template and the metal. Successful template stripping of nickel [143] and titanium [144] has been demonstrated in this manner.

More recently template-stripping has been utilized in the production of high quality metallic micro- and nanopatterns. The working principle is the same as before, but patterned Si templates are utilized instead of flat Si. The pattern will then be replicated onto the stripped metal surface as an inverse structure. High quality metallic nanostructures such as pyramidal arrays, plasmonic slits and bull's eye structures have been demonstrated using template stripping [145]. The patterned metal films can even be transferred onto flexible, curved or stretchable substrates [146].

5.3.1 Fabrication of structured metal films

The fabrication of patterned metal thin films was a direct continuation of the Si etching studies presented earlier in Section 5.2. We were interested in producing nanostructured gold and silver thin films using the etched Si wafers as templates in a template-stripping process. This research work was the topic of **Publication II**.

The main process of template-stripping is illustrated in Figure 5.3. The BCP pattern was transferred into silicon via reactive ion etching as described in Section 5.2. The remaining BCP mask residue was removed using resist remover solutions and oxygen plasma cleaning. The patterned substrates were coated with gold or silver in an electron-beam metal evaporator (Instrumentti Mattila Oy). The physical vapour deposition works by bombarding the target material with an electron beam causing the atoms to vaporize and accelerate away from the target. A coating is formed on the substrate in a line-of-sight manner. In this case, an excess of metal was deposited onto the patterned substrates so that the metal filled the etched patterns and formed a uniform film on top. The thickness of the deposited metal was varied from 50 nm to 200 nm. Deposition was performed in a high vacuum (~ $1 \cdot 10^{-8}$ mbar) in an attempt to avoid the implantation of impurities into the forming metal coating.

The deposited metal thin films were peeled off from the patterned template in a process similar to conventional template stripping. For mechanical support, the backside of the patterned wafer was first bonded to a thick glass slide. The backside glass provided added support and prevented the wafers from breaking after repeated

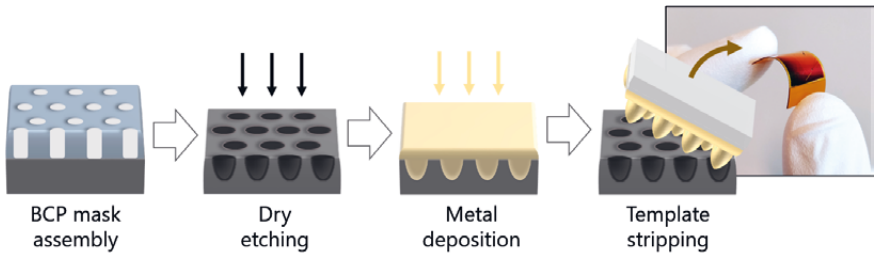

Figure 5.3 The template stripping process. BCP patterns are used as masks for dry etching Si. Metal is uniformly deposited onto the Si template and peeled off onto another substrate. The inset shows a photo of a patterned Au coating (red) on a flexible substrate. Adapted with permission from **P2**. Copyright 2018 American Chemical Society.

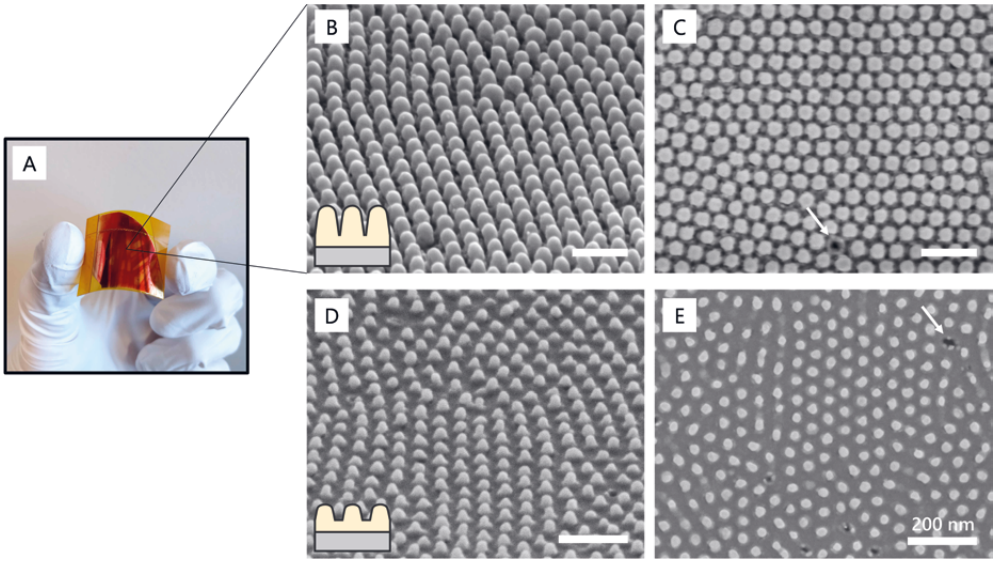

Figure 5.4 (a) Template-stripped gold nanostructures on a yellow polyimide film. Side view and top down view SEM images of hexagonally packed large Au nanodomes (b,c) and small nanodomes (d,e) made by template-stripping from BCP patterned Si moulds. White arrows point to occasionally missing structures. Scale bars 200 nm.

thin film deposition and peel off. A thin glass substrate was bonded onto the topside of the metal film. The UV-curing optical adhesive had excellent adhesion to both metal and glass (NOA 61, Norland Products Inc.). Curing was done in one step in a UV oven with a 400 W UV flood lamp for 5 min. The patterned wafer and the glass were then separated from each other by inserting a scalpel under one edge and lifting gently. Due to the poor adhesion between Si and Au (or Ag), the two substrates tended to break apart at the Si–metal interface. The adhesion was in fact so weak that you could even use tape to peel off the metal layer.

The stripping of metal films onto flexible substrates was also successfully tested. Figure 5.4a displays a patterned gold film that was peeled off onto a thick polyimide film with a silicone adhesive (Kapton tape). The thin metal films could also be made free-standing by depositing a thick metal layer on the backside via electroless plating and peeling off the double metal film. Plating of nickel was done from a heated aqueous solution of the metal salt. Other metals could be used too and technically the free-standing film could be made from solid gold, however that would quickly become rather expensive.

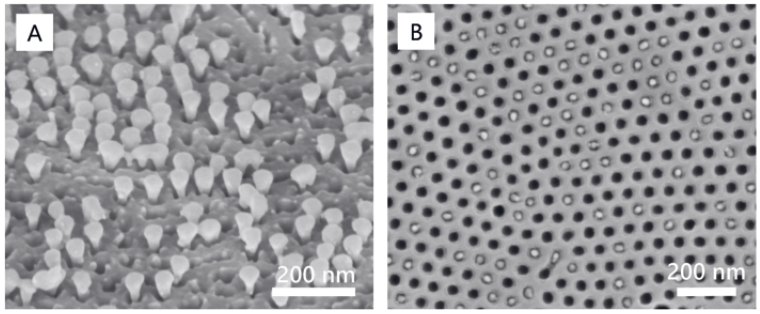

Figure 5.5 Problematic template-stripping of high aspect ratio patterns. (a) Tilted SEM image of teardrop-like Au nanostructures and missing structures (holes). (b) Si mould after template-stripping. Some Au structures (white) have broken off and have not detached from the template.

The etched Si mould determined what type of pattern the metal films would have. BCP patterned Si wafers with conically shaped holes were used to fabricate metal films with conical, dome-like nanostructures. Figure 5.4b-e displays SEM images of small and large gold domes achieved using template-stripping. The difference in size was obtained using Si moulds that were etched during the pattern transfer either for a short time or a slightly longer time. The long template etch time resulted in deeper, wider divots in the Si mould and as a consequence larger and more tightly packed domes in the gold thin film. The dome diameter could be varied from 35 nm to 58 nm using a 188 kg/mol PS-P2VP mask pattern. The maximum dome height that could be achieved was approximately 80 nm.

The fabrication of high aspect ratio nanodomes was attempted unsuccessfully. The formation and detachment of thin and tall domes via template-stripping turned out to be difficult. The filling of the templates during metal deposition tended to be insufficient or non-uniform and template-stripping produced coatings with deformed, teardrop shaped or missing domes (Figure 5.5a). This is likely because the opening in the template shrank as metal was deposited on the edges. Eventually the metal build-up closed the opening and blocked off the cavity resulting in teardrop-like, incomplete filling [147]. When the metal coating was peeled off from the template, the teardrop structures had problems detaching from the mould and they tended to break from the narrow neck area (Figure 5.5b). Ripped off structures were occasionally observed in otherwise well-formed coatings too (Figure 5.4, white arrows).

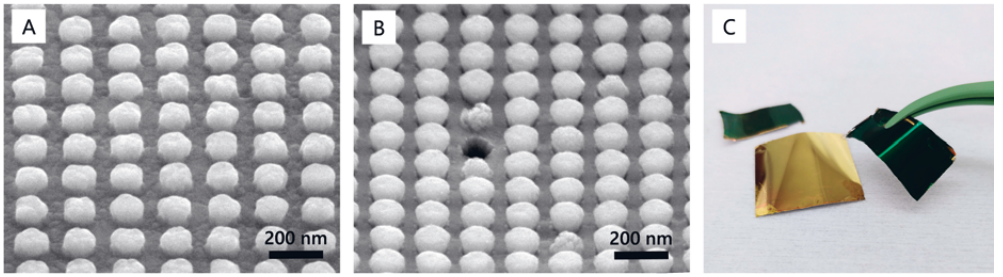

Figure 5.6 Template-stripping from NIL moulds. (a) Silver and (b) gold stripping produced slightly different looking nanostructures from the same template. (c) Free-standing Au films, which appear green due to the nanopatterning.

Template-stripping could be done from any type of patterned silicon or glass wafer. Figure 5.6 depicts gold and silver square-packed domes made from a commercial nanoimprint master mould. The differences in surface quality and filling are likely due to the metals having different thin film growth mechanisms during the deposition. Gold apparently had a tendency to form an air gap around the edge of these structures while silver deposited in a more uniform manner. The template-stripped gold films appeared bright green due to how the structures altered the absorption of light in gold. A further study suggested that the accidentally formed narrow crack around the gold nanostructures could significantly affect the absorption of light in the patterned coatings especially at longer wavelengths [148]. The intentional modification of the absorption of light in the BCP-based metal structures is discussed in Chapter 6.

5.4 Optical characterization

One of the aims of this thesis was to examine how ordered arrays of sub-wavelength nanostructures alter the optical behaviour of the patterned materials. One way to characterize surfaces is to measure the transmittance, absorbance or reflectance of light. Optical measurements were done either using a Lambda 1050 UV–NIR spectrophotometer (PerkinElmer Inc.) or a custom-built integrating sphere spectrometer setup. The total reflectance (specular and diffuse) was measured from the samples at normal incidence or at varying oblique angles. The optical response of the materials

could also be examined using polarized light. Most of the examined samples were non-transparent so the transmittance of light was negligible and thus absorption could be calculated from the reflectance data.

The collective optical properties of photonic nanostructures can often be measured using spectroscopic techniques. However, the measurement results don't really reveal *why* the structures behaved as they did and how the individual structures contributed to it. Simulation methods can be used to shed light on the interactions occurring in the nanoscale. A finite-difference time-domain (FDTD) method was used to simulate the behaviour of the periodic nanostructures. Without going too much into detail, FDTD is a numerical analysis technique that aims to solve Maxwell's equations in discrete spatial and time steps [149]. The structure is essentially divided into small box-shaped cells (mesh) and the electric fields and magnetic fields are computed for the cells in alternating time steps.

In practice, the simulations were carried out in Lumerical FDTD Solutions software (Lumerical Inc.). A unit cell of the periodic structure was built in the solver. The nanostructure was assumed to continue infinitely in the x–y plane. For example, the metal domes were simulated as truncated ellipsoids in a perfect hexagonal lattice with a broadband plane wave as the light source. The downside of using FDTD on small nanostructures was that the mesh had to be extremely fine for the solver to be decently accurate. To lessen the computational load and reduce the required simulation time, axial symmetry rules and boundary conditions could be utilized to reduce the simulation volume. The optical properties as well as the simulation results of the fabricated nanomaterials are further discussed in the following Chapter 6.

6 APPLICATIONS OF PERIODIC SUB-WAVELENGTH NANOSTRUCTURES

Photonics and optoelectronics encompass a wide spectrum of applications including energy conversion devices, telecommunication technologies, quantum information devices, optical sensing, photonic circuits, and optical metamaterials. Many of these applications are based on fundamental material properties such as the refractive index or the plasmonic response of the material. Block copolymers by themselves are not particularly well-suited as they have little to no refractive index contrast or plasmonic properties. However, BCPs can be used as templates to form inorganic hybrid materials that do function as photonic materials.

One avenue of research has been the fabrication of photonic bandgap materials such as 1D, 2D and 3D photonic crystals using nanoparticle doping or selective domain removal and backfilling [8], [150], [151]. Photonic crystals need to have a pattern periodicity close to the length scale of visible wavelengths and thus often require the use of ultra high-molecular weight BCPs (>1000 kg/mol). The other option is photonic materials where the periodicity of the BCP-based structures is in the sub-wavelength regime. The behaviour of these material assemblies is determined by the geometry, size and the composition of the structures. BCPs have been used for example in the making of moth-eye antireflection coatings [13], [152], chiral optical metamaterials [153] and high refractive index surfaces [128], [154]. The following chapter presents the two applications included in this thesis: low refractive index surfaces and coatings that exhibit near perfect light absorption.

6.1 Refractive index modification

The guidance and manipulation of optical waves is often rooted in the reflection and refraction of light. In optical waveguides, light can propagate long distances inside the core material by reflecting between material interfaces. This total internal reflection occurs when the guiding medium has a higher refractive index than the cladding surrounding it. In photonic crystals, certain optical wavelengths are reflected while others are allowed to propagate in the structure. The structure consists of periodic arrangements of high and low index materials. The aforementioned applications are based on the refractive index n of a material, which defines how light gets refracted as it enters the material. The index is material specific and depends on the wavelength of light. When measured at a typical wavelength (~ 633 nm), gases such as air have refractive indices close to 1.0 due to their low density. Polymers such as PS and PMMA have index values around 1.5 while semiconductors are often in the range of 3.0 to 5.0. Low index solid materials are a rarity and materials with a negative refractive index do not naturally exist. Negative refraction can however be achieved in engineered metal-dielectric metamaterials, which have been the subject of intense research efforts [155].

In semiconductor devices, the refractive index is typically changed by either using different materials or by doping a material with suitable impurities. The refractive index can also be altered by introducing sub-wavelength pores into the material layer [156]. Porous semiconductors are composite materials consisting of a matrix of semiconductor and nanoscopic inclusions of air. The dielectric or optical properties of these types of inhomogeneous materials vary in space. To help predict the behaviour of the whole structure, the material can be treated as an *effective medium* with effective properties such as an effective refractive index n_{eff}. The optical properties of inhomogeneous materials can be estimated by effective medium theories. Several different types of effective medium approximations (EMA) have been developed in the past including the popular approaches by Bruggeman, Maxwell-Garnett and Drude [157]. The Lorentz-Lorenz theory, which was used for the calculation of the refractive index of the polymer-solvent mixture in Chapter 4, can also be considered an effective medium approximation.

6.1.1 Effective refractive index of porous silicon

Our approach was to examine the use of BCP lithography in the formation of mesoporous low index silicon. Block copolymers have the distinct advantage of producing porous coatings and membranes with a well-controlled, monodisperse pore size and a uniform spatial distribution of pores. The fabrication and the optical properties of porous Si were studied in **Publication I**. Silicon samples with different surface porosities were fabricated via reactive ion etching as described in Chapter 5. The surface porosity or void fraction was measured by SEM image analysis and according to that, the porosity could be modified from zero (planar Si) to approximately 58 %. This would mean that over half of the surface area would be voids (i.e. air). Theoretically the void fraction could go even higher, but in practice the voids begin to merge together at some point.

To quantify the change in the refractive index, the spectral reflectance curves of the porous Si samples were measured. Figure 6.1a depicts the reflectance of four samples that had an increasing void fraction going from A (f = 0.12) to D (f = 0.34). The reference sample was unmodified planar silicon. Clearly, the addition of voids decreased the overall reflectance of the material especially in the 400 to 600 nm range. The effect of porosity on the effective refractive index of the material was calculated from the obtained data using two effective medium approximations. The

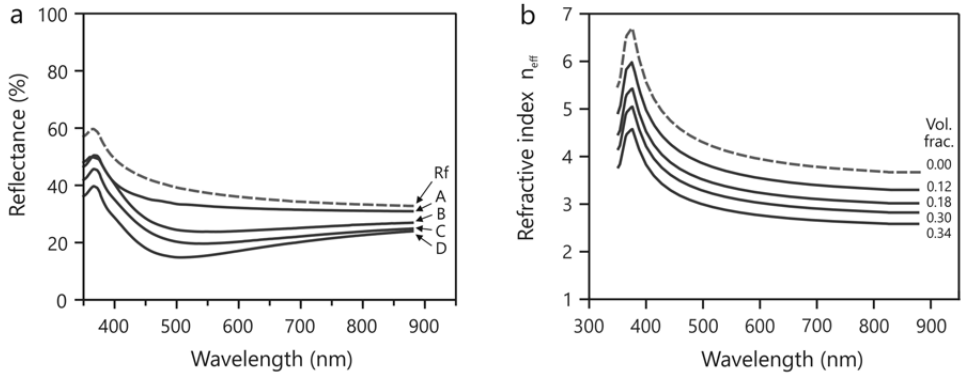

Figure 6.1 (a) Specular and diffuse reflectance of four porous Si samples with increasing degrees of porosity A–D. (b) The real part of the complex effective refractive index of the porous Si samples as estimated by the 2D MGT. The porosity is given as the estimated volume fraction of air. The reflectance and refractive index of the planar Si reference are indicated with the dotted curves.

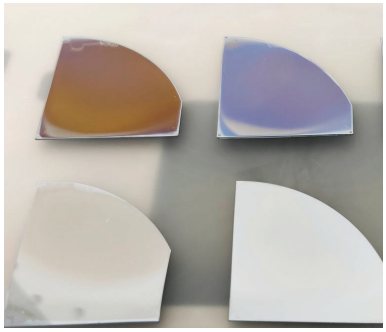

Figure 6.2 Photo of a silicon quarter wafer (bottom right) and three wafers with increasing surface porosities towards the top left. The change in the refractive index is seen as a colour change.

volume-averaging theory (VAT) and the 2D Maxwell-Garnett theory (2D MGT) are explained in more detail in **Publication I**. Both EMAs produced similar estimates of the effective refractive index curves, although the 2D MGT was more accurate in predicting the void fraction. The effective refractive indices as determined by the 2D MGT are reported in Figure 6.1b for the aforementioned cases A–D. So at maximum, an approximately 30 % reduction in the refractive index of Si was obtained going from 3.88 to 2.71 (at 633 nm). The change in the effective refractive index was also visible to the eye. Figure 6.2 shows a photo of planar Si and three Si wafers that have differing surface porosities. High porosity can be seen as a blue or brown colour.

The maximum reduction of the effective refractive index was achieved at a relatively low void fraction of $f = 0.34–0.38$. As mentioned earlier, Si wafers were also fabricated with higher void fractions. However, the porous Si materials with a void fraction larger than 0.40 performed rather badly in the optical measurements. A cross-section analysis revealed that due to (over)etching, the pore shape had changed and the voids had become very shallow. After publishing **Publication I**, the lithography process was further optimized and patterned Si with a high void fraction could be obtained (f = 0.49). The refractive indices of these materials were not determined since the patterned Si wafers were used for other applications.

The research into porous Si indicated that materials and devices that have a varying refractive index could be fabricated simply by tuning the porosity of the material in the desired location. The process presented in **Publication I** was rather straightforward, since the degree of porosity was tuned via the etch time. Etching could be done

in selected areas leading to graded index materials or materials with an ultra-low refractive index. It should be noted that the index tuning method is not limited only to silicon, since the inclusions of voids can change the effective dielectric or optical properties of any material. In fact, porous materials are currently one of the few viable methods to achieve ultra-low dielectric constant ($\kappa < 2.0$) materials for the insulating dielectrics in integrated circuits [158]. In addition to block copolymers, porosity could be introduced via colloidal particles, zeolites or surfactants.

6.2 Perfect optical absorbers

Many photonic components or devices are based on the absorption of light in materials. Colour filters selectively transmit certain wavelengths while absorbing or reflecting the unwanted portion of light. Solar cells try to absorb a broad wavelength range and efficiently convert light into electricity. Photodetectors detect light by absorbing selected wavelength ranges. Perfect optical absorbers are materials or structures that efficiently absorb all or nearly all photons in either a narrow or a broad range of wavelengths. These can be used in for example the aforementioned applications. Often it is preferable that the absorber structures are thin, flat and can be incorporated into other optical or optoelectronic devices. Both narrow band and broadband perfect or near-perfect optical absorbers have been realized using various fabrication schemes [159]–[163].

When illuminated with light, nanostructures made from certain metals exhibit localised surface plasmons (LSP). LSPs are coherent oscillations of the electron cloud of a metal nanoparticle, which arise at the metal–dielectric interface when exited by incident photons [164]. Photons with a frequency (i.e. wavelength) that matches the oscillation frequency are absorbed by the metal particles. Silver and gold are two commonly used plasmonic metals. Their plasmon resonance wavelength is located in the ultra-violet or visible regions. For LSPs, the resonance can be fine-tuned by altering the physical size, shape or arrangement of the metal nanostructures or by changing the local environment [164]. Due to the LSP effect, regions near the metal nanoparticle surface exhibit a greatly enhanced electric field. These regions are colloquially called hot-spots. Field enhancement can be utilized to boost various optical phenomena such as fluorescence, photo-catalysis or energy conversion.

6.2.1 Light absorption in patterned gold coatings

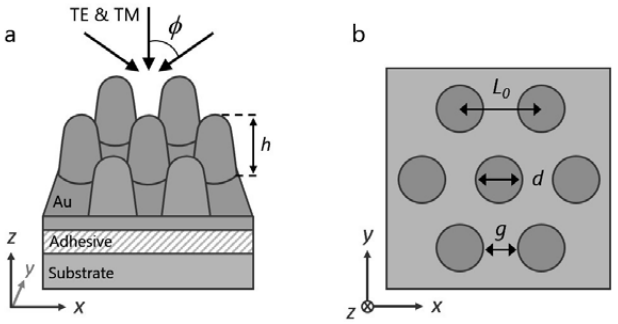

Figure 6.3 Diagram of the broadband optical absorber consisting of arrays of metal nanodomes. (a) Side view and (b) top view of the absorber unit structure. The absorber was illuminated by TE-, TM- and non-polarized light at varying angles of incidence ϕ.

Our approach was to explore the use of sub-wavelength patterned plasmonic metals as optical absorbers. Visible light absorption in nanopatterned metal coatings made via template-stripping was explored in **Publication II**. Figure 6.3 illustrates the structure of the plasmonic absorber. The top metal layer was patterned with a periodic hexagonal array of domes with a periodicity of L_0 and a height and diameter of h and d, respectively. The details of the nanodome fabrication process were discussed in the previous Chapter 5. The metal layer under the patterns was made thick enough that it could be considered non-transparent. For gold a layer thickness of 100–200 nm was sufficient. The patterned metal coating was bonded to the desired substrate using an adhesive layer. The layers under the optically thick metal layer did not affect the absorption properties of the coating.

Figure 6.4a illustrates the absorption of light in three experimentally realized Au nanodome coatings I–III with increasing dome size. Due to the way the domes were fabricated, the increased size brought the domes closer together and decreased the gap between them. It could be observed that the larger and taller the domes were, the better the absorption of light was. The absorption behaviour of the domes was verified via FDTD simulations. The FDTD models used geometric parameters such as height, width and periodicity that were extracted from SEM images (±5 nm). It was possible to relatively well replicate the observed absorption behaviour (Figure 6.4b). This confirmed that the change in absorption originated from the change in the pattern

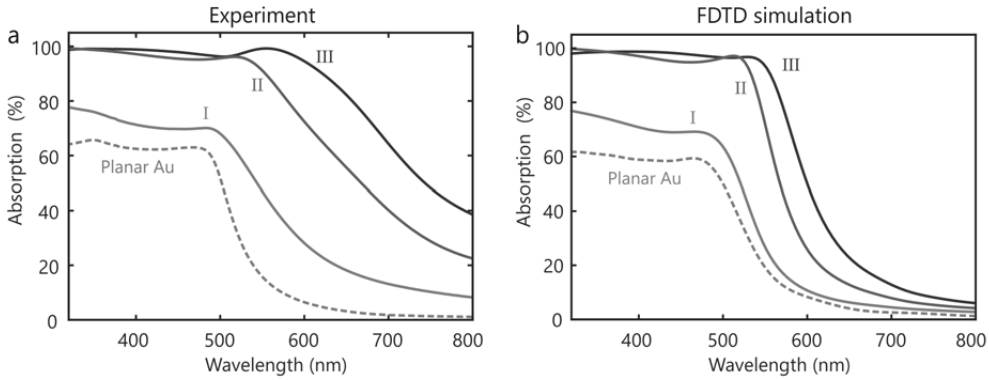

Figure 6.4 (a) Absorption spectra measured at normal incidence from planar, unpatterned gold and three patterned Au nanodome thin films with increasing dome sizes I—III. (b) Simulated absorption spectra of the same three cases I—III assuming a perfect hexagonal lattice. Adapted with permission from **P2**. Copyright 2018 American Chemical Society.

geometry, at least at short wavelengths. At longer wavelengths, the simulation could not so accurately predict the absorption properties of the nanodomes. It was thought that this might be because the FDTD simulations used a perfect, uniform lattice structure and couldn't account for spatial variations such as grains, defects or local variations in the dome geometry. Figure 6.5a shows that multiple resonance peaks appear at longer wavelengths in the spectral response if the gap distance is slightly varied. This could contribute to the response of the experimental samples at longer wavelengths. It's known that the spectral range of plasmon-mediated absorption can be broadened by including structures with varying geometry via collective effects such as plasmon near-field coupling and multiple LSP resonances [165].

Further simulations were done to examine the effects of the dome height, width and periodicity separately. Perfect absorption could be realized when the gap between the domes was smaller than 25 nm and the dome height was at least 70 nm. The periodicity of the structure in itself did not matter as long as the two other conditions (height+gap) were fulfilled. Experimentally, perfect absorption (~97 %, 300–650 nm) was achieved in a dome patterned Au thin film with a gap width of 16 nm and a height of 80 nm (Figure 6.4a case III). Furthermore, the broadband absorption in the plasmonic coating persisted at over 90 % even when the coating was illuminated at oblique angles (8–60°) or using polarized light. This is a significant achievement for a nanostructured plasmonic absorber. Many ultrathin optical absorber designs are only

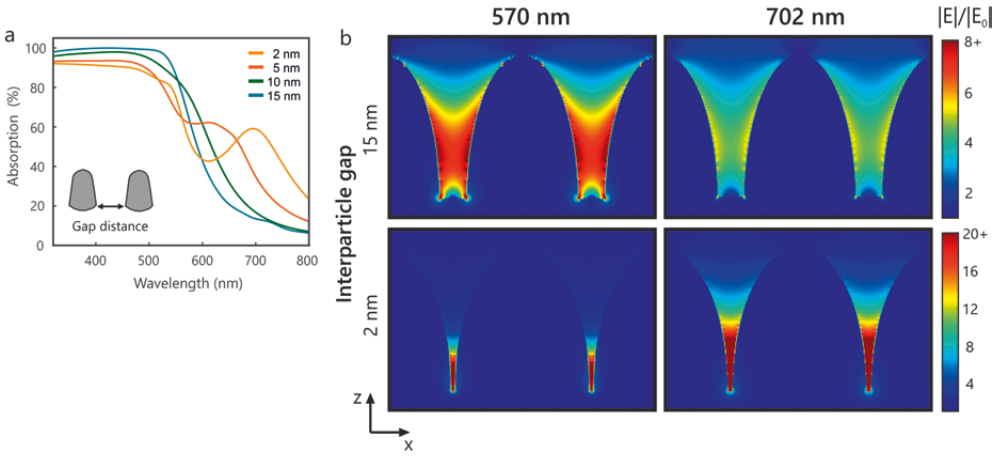

Figure 6.5 (a) Effect of the interparticle distance on the light absorption. (b) The electric field enhancement according to FDTD simulations at 570 nm and 702 nm wavelengths. The dome was modelled as h = 80 nm and L_0 = 75 nm with varying gap distances.

effective for certain angles of incidence or they absorb only the transverse electric (TE) or transverse magnetic (TM) components of the plane wave [166]–[168].

FDTD simulations were used to examine the local electric field enhancement near the nanodomes. The local electric fields close to the nanodomes could achieve strengths that were much higher than that of the incident electric field. Figure 6.5b shows the calculated electric field enhancement at two excitation wavelengths, 570, and 702 nm. The electric field could be seen to be confined in the gap between adjacent domes. If the gap was made narrower, the field localization was seen to move towards the bottom of the gap and the field enhancement increased significantly. This is to be expected as the electric field usually increases as the distance between two plasmonic particles is reduced and the plasmon coupling between them increases [164].

Field enhancement hot-spots are usually formed by placing two plasmonic particles close to each other with a small gap in between [164]. However, the general consensus seems to be that the production of hot-spots is still difficult, especially in terms of reproducibility and controlled gap width. Colloidal assemblies are lacking in reproducibility and while methods such as FIB and EBL are excellent for controlled placement of structures, their throughput is regrettably low. BCP-based methods have only just began to gain interest as viable strategies for the production of plasmonic hot-spot and sensing materials [169], [170]. Hot-spots enable a variety of applications

including single molecule detection and surface enhanced Raman spectroscopy (SERS) [171]. SERS is a surface sensitive measurement method where molecules are placed on a patterned metal surface and probed with a laser beam. The hot-spots on the metal surface enhance the Raman signal enabling the detection of minute amounts of analyte. The rapid detection of trace amounts of molecules and biomarkers is currently in high demand in healthcare as well as in environmental monitoring and biosecurity. Other uses of patterned metals include plasmon mediated catalysis and hot-electron generation for harnessing solar energy [172].

7 CONCLUSIONS AND OUTLOOK

Nanolithography and nanostructures are the core technology and building blocks of modern microelectronics and photonic technologies. Presently, manufacturers are seeking to make smaller, faster and lighter components in the pursuit of more advanced devices. Bottom-up methods, such as the self-assembly of block copolymer molecules, are promising strategies for building photonic or microelectronic devices but they have yet to become mainstream. The motivation behind the development of block copolymer technology is that BCPs provide access to a nanoscale pattern size, extreme pattern density and large-area spatial coverage that is currently difficult to achieve using conventional lithography in a one-step process. Great progress has been made in understanding, controlling and using block copolymers since their discovery in the 1950s and the first lithography demonstrations in the 1990s [173], [174]. In certain areas, such as IC contact size reduction, pitch multiplication and FinFET fin patterning, BCP lithography is slowly becoming a mature patterning technology, the potential of which has been recognized by the International Technology Roadmap for Semiconductors and the International Roadmap for Devices and Systems [4], [5]. Nevertheless, there is still a lot of research to be done especially concerning high-χ and high-molecular weight polymers.

The driving force in this thesis has been the interest to study how high-molecular weight polystyrene–polyvinylpyridine polymers can be used in the fabrication of nanophotonic materials. A lot of work has been put into controlling the self-assembly and obtaining useable patterns over large surface areas using solvent vapour annealing. The self-assembly behaviour of block copolymers during solvent vapour annealing is complex and can be influenced by many environmental factors. Currently, one of the main challenges in SVA is acquiring the desired, defect-free pattern morphology in a reproducible way. This thesis has presented the development

of a computer-controlled solvent vapour annealing device that has precise control of the film swelling process. The annealing process functions using a feedback loop, which should minimize user-related variances and be able to correct for fluctuations arising from external factors such as room temperature variations. These issues have usually made manually controlled systems unreliable. A key result shown in this thesis is that the outcome of solvent annealing is highly dependent on two factors: the swelling ratio and the time that the thin film is held at a constant swelling ratio. It is also shown that high-molecular weight BCPs can in fact self-assemble in minutes when correct swelling parameters are used. The results indicate that it would be highly beneficial to move onward from static solvent annealing, where the process and the film swelling is poorly controlled, to fully automated, computer-controlled and -monitored systems.

The second part of this thesis has focussed on the fabrication and characterization of photonic nanostructures made using block copolymer lithography. BCP-templated inorganic nanostructures can be used as building blocks for novel nanoscale sensors and emitters, catalytic materials, or functional coatings. A method for producing mesoporous silicon with easily tunable pore size and void fraction was introduced. The void fraction could be altered by changing the dry etching time since the pores grew in both lateral and horizontal directions due to the isotropic etching. The introduction of nanoscale voids changed the effective optical properties of the semiconductor as determined by reflectometry and effective medium approximation calculations. The findings indicate that it is possible to tune the refractive index of materials in a controlled manner using block copolymer lithography.

The lithography process was further developed to produce high-quality plasmonic metasurfaces patterned with sub-wavelength nanodomes. The absorption of visible light in the patterned coatings could be manipulated by changing the dimensions of the domes. A key result is that with the correct dimensions, perfect broadband absorption of visible light could be achieved in the material. Furthermore, the absorption was shown to be omnidirectional meaning that light rays coming in from oblique angles would also be absorbed. Since the fabricated metasurface is a thin coating, it could theoretically be applied to any kind of substrate or surface. Perfect absorber coatings would be advantageous in solar energy conversion devices or plasmon-enhanced sensing applications.

To conclude the work, it remains uncertain when the self-assembly of BCPs via solvent annealing will spread beyond laboratory research into device manufacturing. In that sense thermal annealing methods are already several steps ahead and have raised the interest of IC companies like Tokyo Electron, IMEC and IBM [42], [64], [175]. However, the interest in high-χ BCPs has been driving the SVA research forward. A critical perspective on SVA [176] has summarized three key aspects that need to be addressed. We need better controlled annealing systems for improved reproducibility. There should be better modeling of the dynamics and kinetics of BCP phase separation. And finally, BCP lithography should be implemented in real-life applications. Hopefully, this thesis has contributed to two of those three key areas and shown that despite the challenges there is great potential in solvent annealing and block copolymers.

REFERENCES

[1] T. Inoue, T. Soen, T. Hashimoto and H. Kawai, Thermodynamic interpretation of domain structure in solvent-cast films of A-B type block copolymers of styrene and isoprene, *Journal of Polymer Science Part A-2: Polymer Physics*, vol. 7, no. 8, 1283–1301, 1969.

[2] A. Lane, X. Yang, M. Maher, G. Blachut, Y. Asano, Y. Someya, A. Mallavarapu, S. Sirard, C. Ellison and G. Willson, Directed self-assembly and pattern transfer of five nanometer block copolymer lamellae, *ACS Nano*, vol. 11, no. 8, 7656–7665, 2017.

[3] J. Kennemur, L. Yao, F. Bates and M. Hillmyer, Sub-5 nm domains in ordered poly(cyclohexyl ethylene)-block-poly(methyl methacrylate) block polymers for lithography, *Macromolecules*, vol. 47, no. 4, 1411–1418, 2014.

[4] ITRS. (2015). 'The International Technology Roadmap for Semiconductors 2.0,' [Online]. Available: `http://www.itrs2.net/` (visited on 26/04/2020).

[5] IRDS. (2017). 'International Roadmap for Devices and Systems 2017 - Emerging research materials,' [Online]. Available: `https://irds.ieee.org/editions/2017` (visited on 25/04/2020).

[6] S. Park, Y. Kim, H. Ahn, J. Kim, P. Yoo and D. Ryu, Giant gyroid and templates from high-molecular-weight block copolymer self-assembly, *Scientific Reports*, vol. 6, 36326, 2016.

[7] H. Ahn, S. Park, S.-W. Kim, P. Yoo, D. Ryu and T. Russell, Nanoporous block copolymer membranes for ultrafiltration: A simple approach to size tunability, *ACS Nano*, vol. 8, no. 11, 11745–11752, 2014.

[8] T. Deng, C. Chen, C. Honeker and E. Thomas, Two-dimensional block copolymer photonic crystals, *Polymer*, vol. 44, no. 21, 6549–6553, 2003.

[9] J. Dolan, M. Saba, R. Dehmel, I. Gunkel, Y. Gu, U. Wiesner, O. Hess, T. Wilkinson, J. Baumberg, U. Steiner and B. Wilts, Gyroid optical metamaterials: Calculating the effective permittivity of multidomain samples, *ACS Photonics*, vol. 3, no. 10, 1888–1896, 2016.

[10] H.-B. Seo, Y.-G. Yu, C.-G. Chae, M.-J. Kim and J.-S. Lee, Synthesis of ultrahigh molecular weight bottlebrush block copolymers of w-end-norbornyl polystyrene and polymethacrylate macromonomers, *Polymer*, vol. 177, 241–249, 2019.

[11] J. Mapas, T. Thomay, A. Cartwright, J. Ilavsky and J. Rzayev, Ultrahigh molecular weight linear block copolymers: Rapid access by reversible-deactivation radical polymerization and self-assembly into large domain nanostructures, *Macromolecules*, vol. 49, no. 10, 3733–3738, 2016.

[12] Y.-W. Chiang, C.-Y. Chou, C.-S. Wu, E.-L. Lin, J. Yoon and E. Thomas, Large-area block copolymer photonic gel films with solvent-evaporation-induced red- and blue-shift reflective bands, *Macromolecules*, vol. 48, no. 12, 4004–4011, 2015.

[13] P. Mokarian-Tabari, R. Senthamaraikannan, C. Glynn, T. Collins, C. Cummins, D. Nugent, C. O'Dwyer and M. Morris, Large block copolymer self-assembly for fabrication of subwavelength nanostructures for applications in optics, *Nano Letters*, vol. 17, no. 5, 2973–2978, 2017.

[14] C. Banbury, J. Rickard, S. Mahajan and P. Goldberg Oppenheimer, Tunable metamaterial-like platforms for surface-enhanced Raman scattering via three-dimensional block copolymer-based nanoarchitectures, *ACS Applied Materials & Interfaces*, vol. 11, no. 15, 14437–14444, 2019.

[15] M. Szwarc, M. Levy and R. Milkovich, Polymerization initiated by electron transfer to monomer. A new method of formation of block polymers, *Journal of the American Chemical Society*, vol. 78, no. 11, 2656–2657, 1956.

[16] A. Pitto-Barry and N. Barry, Pluronic block-copolymers in medicine: From chemical and biological versatility to rationalisation and clinical advances, *Polymer Chemistry*, vol. 5, no. 10, 3291–3297, 2014.

[17] J. Rzayev, Synthesis of polystyrene-polylactide bottlebrush block copolymers and their melt self-assembly into large domain nanostructures, *Macromolecules*, vol. 42, no. 6, 2135–2141, 2009.

[18] B. Runge and N. Bowden, Synthesis of high molecular weight comb block copolymers and their assembly into ordered morphologies in the solid state, *Journal of the American Chemical Society*, vol. 129, no. 34, 10551–10560, 2007.

[19] A. Matsuo, T. Watanabe and A. Hirao, Synthesis of well-defined dendrimer-like branched polymers and block copolymer by the iterative approach involving coupling reaction of living anionic polymer and functionalization, *Macromolecules*, vol. 37, no. 17, 6283–6290, 2004.

[20] R. Ruiz, H. Kang, F. Detcheverry, E. Dobisz, D. Kercher, T. Albrecht, J. de Pablo and P. Nealey, Density multiplication and improved lithography by directed block copolymer assembly, *Science*, vol. 321, no. 5891, 936–939, 2008.

[21] A. Tavakkoli, S. Nicaise, K. Gadelrab, A. Alexander-Katz, C. Ross and K. Berggren, Multilayer block copolymer meshes by orthogonal self-assembly, *Nature Communications*, vol. 7, no. 10518, 2016.

[22] A. Rahman, P. Majewski, G. Doerk, C. Black and K. Yager, Non-native three-dimensional block copolymer morphologies, *Nature Communications*, vol. 7, 13988, 2016.

[23] H. Jung, W. Shin, T. Park, Y. Choi, Y. Yoon, S. Park, J.-H. Lim, J.-D. Kwon, J. Lee, S.-H. Kwon, G. Seong, K. Kim and W. Park, Hierarchical multi-level block copolymer patterns by multiple self-assembly, *Nanoscale*, vol. 11, no. 17, 8433–8441, 2019.

[24] F. Bates and G. Fredrickson, Block copolymer thermodynamics: theory and experiment, *Annual Review of Physical Chemistry*, vol. 41, no. 1, 525–557, 1990.

[25] E. Helfand, Block copolymer theory. III. Statistical mechanics of the microdomain structure, *Macromolecules*, vol. 8, no. 4, 552–556, 1975.

[26] E. Helfand and Z. Wasserman, Block copolymer theory. 4. Narrow interphase approximation, *Macromolecules*, vol. 9, no. 6, 879–888, 1976.

[27] D. Meier, Theory of block copolymers. I. Domain formation in A-B block copolymers, *Journal of Polymer Science Part C: Polymer Symposia*, vol. 26, no. 1, 81–98, 1969.

[28] S. Edwards, The statistical mechanics of polymers with excluded volume, *Proceedings of the Physical Society*, vol. 85, no. 4, 1965.

[29] M. Matsen and M. Schick, Stable and unstable phases of a diblock copolymer melt, *Physical Review Letters*, vol. 72, no. 16, 2660–2663, 1994.

[30] M. Matsen, Fast and accurate SCFT calculations for periodic block-copolymer morphologies using the spectral method with Anderson mixing, *European Physical Journal E*, vol. 30, no. 4, 361–369, 2009.

[31] L. Leibler, Theory of microphase separation in block copolymers, *Macromolecules*, vol. 13, no. 6, 1602–1617, 1980.

[32] A. Semenov, Contribution to the theory of microphase layering in block copolymer melts, *Journal of Experimental and Theoretical Physics*, vol. 88, 1242–1256, 1985.

[33] L. Sperling, Dilute solution thermodynamics, molecular weights, and sizes, *Introduction to Physical Polymer Science*. John Wiley & Sons, 2005, ch. 3, 71–143.

[34] W. Zha, C. Han, D. Lee, S. Han, J. Kim, J. Kang and C. Park, Origin of the difference in order-disorder transition temperature between polystyrene- block-poly(2-vinylpyridine) and polystyrene- block- poly(4-vinylpyridine) copolymers, *Macromolecules*, vol. 40, no. 6, 2109–2119, 2007.

[35] T. Lodge, K. Hanley, B. Pudil and V. Alahapperuma, Phase behavior of block copolymers in a neutral solvent, *Macromolecules*, vol. 36, no. 3, 816–822, 2003.

[36] T. Russell, R. Hjelm and P. Seeger, Temperature dependence of the interaction parameter of polystyrene and poly(methyl methacrylate), *Macromolecules*, vol. 23, no. 3, 890–893, 1990.

[37] K. Dai and E. Kramer, Determining the temperature-dependent Flory interaction parameter for strongly immiscible polymers from block copolymer segregation measurements, *Polymer*, vol. 35, no. 1, 157–161, 1994.

[38] A. Zalusky, R. Olayo-Valles, J. Wolf and M. Hillmyer, Ordered nanoporous polymers from polystyrene-polylactide block copolymers, *Journal of the American Chemical Society*, vol. 124, no. 43, 12761–12773, 2002.

[39] E. Cochran, D. Morse and F. Bates, Design of ABC triblock copolymers near the ODT with the random phase approximation, *Macromolecules*, vol. 36, no. 3, 782–792, 2003.

[40] G. Alberda van Ekenstein, R. Meyboom, G. ten Brinke and O. Ikkala, Determination of the Flory-Huggins interaction parameter of styrene and 4-vinylpyridine using copolymer blends of poly(styrene-co-4-vinylpyridine) and polystyrene, *Macromolecules*, vol. 33, no. 10, 3752–3756, 2000.

[41] L. Wan, R. Ruiz, H. Gao, K. Patel, T. Albrecht, J. Yin, J. Kim, Y. Cao and G. Lin, The limits of lamellae-forming PS-b-PMMA block copolymers for lithography, *ACS Nano*, vol. 9, no. 7, 7506–7514, 2015.

[42] C.-C. Liu, E. Franke, Y. Mignot, R. Xie, C. Yeung, J. Zhang, C. Chi, C. Zhang, R. Farrell, K. Lai, H. Tsai, N. Felix and D. Corliss, Directed self-assembly of block copolymers for 7 nanometre FinFET technology and beyond, *Nature Electronics*, vol. 1, no. 10, 562–569, 2018.

[43] H. Tsai, J. Pitera, H. Miyazoe, S. Bangsaruntip, S. Engelmann, C.-C. Liu, J. Cheng, J. Bucchignano, D. Klaus, E. Joseph, D. Sanders, M. Colburn and M. Guillorn, Two-dimensional pattern formation using graphoepitaxy of PS-b-PMMA block copolymers for advanced FinFET device and circuit fabrication, *ACS Nano*, vol. 8, no. 5, 5227–5232, 2014.

[44] C.-J. Lee and J. Cheng, Method for integrated circuit manufacturing with directed self-assembly (DSA), US patent US10418245B2, 2019.

[45] M. Aizawa and J. Buriak, Block copolymer-templated chemistry on Si, Ge, InP, and GaAs surfaces, *Journal of the American Chemical Society*, vol. 127, no. 25, 8932–8933, 2005.

[46] J. Chai and J. Buriak, Using cylindrical domains of block copolymers to self-assemble and align metallic nanowires, *ACS Nano*, vol. 2, no. 3, 489–501, 2008.

[47] C. Cummins, A. Gangnaik, R. Kelly, D. Borah, J. O'Connell, N. Petkov, Y. Georgiev, J. Holmes and M. Morris, Aligned silicon nanofins via the directed self-assembly of PS-b-P4VP block copolymer and metal oxide enhanced pattern transfer, *Nanoscale*, vol. 7, no. 15, 6712–21, 2015.

[48] W. Wei, L. Samad, J. Choi, Y. Joo, A. Way, M. Arnold, S. Jin and P. Gopalan, Synthesis of molybdenum disulfide nanowire arrays using a block copolymer template, *Chemistry of Materials*, vol. 28, no. 11, 4017–4023, 2016.

[49] C. Cummins, A. Bell and M. Morris, Creating active device materials for nanoelectronics using block copolymer lithography, *Nanomaterials*, vol. 7, no. 10, 304, 2017.

[50] S. Kochuveedu, Y. Jang, Y. Jang and D. Kim, Visible light active photocatalysis on block copolymer induced strings of ZnO nanoparticles doped with carbon, *Journal of Materials Chemistry A*, vol. 1, no. 3, 898–905, 2013.

[51] J. Yin, X. Yao, J. Liou, W. Sun, Y. Sun and Y. Wang, Membranes with highly ordered straight nanopores by selective swelling of fast perpendicularly aligned block copolymers, *ACS Nano*, vol. 7, no. 11, 9961–9974, 2013.

[52] K. Sparnacci, D. Antonioli, V. Gianotti, M. Laus, F. Ferrarese Lupi, T. Giammaria, G. Seguini and M. Perego, Ultrathin random copolymer-grafted layers for block copolymer self-assembly, *ACS Applied Materials and Interfaces*, vol. 7, no. 20, 10944–10951, 2015.

[53] S. Ji, C.-C. Liu, J. Son, K. Gotrik, G. Craig, P. Gopalan, F. Himpsel, K. Char and P. Nealey, Generalization of the use of random copolymers to control the wetting behavior of block copolymer films, *Macromolecules*, vol. 41, no. 23, 9098–9103, 2008.

[54] S. Ham, C. Shin, E. Kim, D. Ryu, U. Jeong, T. Russell and C. Hawker, Microdomain orientation of PS-b-PMMA by controlled interfacial interactions, *Macromolecules*, vol. 41, no. 17, 6431–6437, 2008.

[55] S. Ji, G. Liu, F. Zheng, G. Craig, F. Himpsel and P. Nealey, Preparation of neutral wetting brushes for block copolymer films from homopolymer blends, *Advanced Materials*, vol. 20, no. 16, 3054–3060, 2008.

[56] M. Ceresoli, M. Palermo, F. Ferrarese Lupi, G. Seguini, M. Perego, G. Zuccheri, S. Phadatare, D. Antonioli, V. Gianotti, K. Sparnacci and M. Laus, Neutral wetting brush layers for block copolymer thin films using homopolymer blends processed at high temperatures, *Nanotechnology*, vol. 26, no. 415603, 2015.

[57] E. Han, K. Stuen, M. Leolukman, C. Liu, P. Nealey and P. Gopalan, Perpendicular orientation of domains in cylinder-forming block copolymer thick films by controlled interfacial interactions, *Macromolecules*, vol. 42, no. 13, 4896–4901, 2009.

[58] J. Oh, H. Suh, Y. Ko, Y. Nah, J. Lee, B. Yeom, K. Char, C. Ross and J. Son, Universal perpendicular orientation of block copolymer microdomains using a filtered plasma, *Nature Communications*, vol. 10, no. 1, 2019.

[59] D. Borah, M. Ozmen, S. Rasappa, M. Shaw, J. Holmes and M. Morris, Molecularly functionalized silicon substrates for orientation control of the microphase separation of PS-b-PMMA and PS-b-PDMS block copolymer systems, *Langmuir*, vol. 29, no. 9, 2809–2820, 2013.

[60] C. Cummins, D. Borah, S. Rasappa, A. Chaudhari, T. Ghoshal, B. O'Driscoll, P. Carolan, N. Petkov, J. Holmes and M. Morris, Self-assembly of polystyrene-block-poly(4-vinylpyridine) block copolymer on molecularly functionalized silicon substrates: Fabrication of inorganic nanostructured etchmask for lithographic use, *Journal of Materials Chemistry C*, vol. 1, 7941–7951, 2013.

[61] J. Jeong, Y. Hur, H. Kim, J. Kim, W. Park, M. Kim, B. Kim and Y. Jung, Proximity injection of plasticizing molecules to self-assembling polymers for large-area, ultrafast nanopatterning in the sub-10-nm regime, *ACS Nano*, vol. 7, no. 8, 6747–6757, 2013.

[62] C.-C. Liu, E. Han, S. Onses, C. Thode, S. Ji, P. Gopalan and P. Nealey, Fabrication of lithographically defined chemically patterned polymer brushes and mats, *Macromolecules*, vol. 44, no. 7, 1876–1885, 2011.

[63] P. R. Delgadillo, C. Thode, P. Nealey, R. Gronheid, H. Wu, Y. Cao, M. Somervell and K. Nafus, Implementation of a chemo-epitaxy flow for directed self-assembly on 300-mm wafer processing equipment, *Journal of Micro/Nanolithography, MEMS, and MOEMS*, vol. 11, no. 3, 031302, 2012.

[64] B. Rathsack, M. Somervell, J. Hooge, M. Muramatsu, K. Tanouchi, T. Kitano, E. Nishimura, K. Yatsuda, S. Nagahara, I. Hiroyuki, K. Akai and T. Hayakawa, Pattern scaling with directed self assembly through lithography and etch process integration, *Proc. SPIE 8323, Alternative Lithographic Technologies IV*, 2012, 83230B.

[65] M. Stoykovich, H. Kang, K. Daoulas, G. Liu, C.-C. Liu, J. de Pablo, M. Müller and P. Nealey, Directed self-assembly of block copolymers for nanolithography: fabrication of isolated features and essential integrated circuit geometries, *ACS Nano*, vol. 1, no. 3, 168–175, 2007.

[66] M. Maher, J. Self, P. Stasiak, G. Blachut, C. Ellison, M. Matsen, C. Bates and G. Willson, Structure, stability, and reorganization of $0.5L_0$ topography in block copolymer thin films, *ACS Nano*, vol. 10, no. 11, 10152–10160, 2016.

[67] M. Fasolka, P. Banerjee, A. Mayes, G. Pickett and A. Balazs, Morphology of ultrathin supported diblock copolymer films: Theory and experiment, *Macromolecules*, vol. 33, no. 15, 5702–5712, 2000.

[68] A. Knoll, R. Magerle and G. Krausch, Phase behavior in thin films of cylinder-forming ABA block copolymers: Experiments, *The Journal of Chemical Physics*, vol. 120, no. 2, 1105–1116, 2004.

[69] T. Thurn-Albrecht, J. Derouchey, T. Russell and H. Jaeger, Overcoming interfacial interactions with electric fields, *Macromolecules*, vol. 33, no. 9, 3250–3253, 2000.

[70] M.-L. Wu, D. Wang and L.-J. Wan, Directed block copolymer self-assembly implemented via surface-embedded electrets, *Nature Communications*, vol. 7, 10752, 2016.

[71] K. Yager, N. Fredin, X. Zhang, B. Berry, A. Karim and R. Jones, Evolution of block copolymer order through a moving thermal zone, *Soft Matter*, vol. 6, no. 1, 92–99, 2010.

[72] P. Majewski and K. Yager, Millisecond ordering of block copolymer films via photothermal gradients, *ACS Nano*, vol. 9, no. 4, 3896–3906, 2015.

[73] W. Phillip, M. Hillmyer and E. Cussler, Cylinder orientation mechanism in block copolymer thin films upon solvent evaporation, *Macromolecules*, vol. 43, no. 18, 7763–7770, 2010.

[74] S.-M. Hur, V. Thapar, A. Ramírez-Hernández, P. Nealey and J. de Pablo, Defect annihilation pathways in directed assembly of lamellar block copolymer thin films, *ACS Nano*, vol. 12, no. 10, 9974–9981, 2018.

[75] P. Majewski and K. Yager, Reordering transitions during annealing of block copolymer cylinder phases, *Soft Matter*, vol. 12, no. 1, 281–294, 2016.

[76] C. Black and K. Guarini, Structural evolution of cylindrical-phase diblock copolymer thin films, *Journal of Polymer Science Part A: Polymer Chemistry*, vol. 42, no. 8, 1970–1975, 2004.

[77] S. Ji, C.-C. Liu, W. Liao, A. Fenske, G. Craig and P. Nealey, Domain orientation and grain coarsening in cylinder-forming poly(styrene-b-methyl methacrylate) films, *Macromolecules*, vol. 44, no. 11, 4291–4300, 2011.

[78] F. Ferrarese Lupi, T. Giammaria, M. Ceresoli, G. Seguini, K. Sparnacci, D. Antonioli, V. Gianotti, M. Laus and M. Perego, Rapid thermal processing of self-assembling block copolymer thin films, *Nanotechnology*, vol. 24, no. 31, 315601, 2013.

[79] M. Perego, F. Ferrarese Lupi, M. Ceresoli, T. Giammaria, G. Seguini, E. Enrico, L. Boarino, D. Antonioli, V. Gianotti, K. Sparnacci and M. Laus, Ordering dynamics in symmetric PS-b-PMMA diblock copolymer thin films during rapid thermal processing, *Journal of Materials Chemistry C*, vol. 2, no. 32, 6655–6664, 2014.

[80] X. Zhang, K. Harris, N. Wu, J. Murphy and J. Buriak, Fast assembly of ordered block copolymer nanostructures through microwave annealing, *ACS Nano*, vol. 4, no. 11, 7021–7029, 2010.

[81] G. Singh, K. Yager, D. Smilgies, M. Kulkarni, D. Bucknall and A. Karim, Tuning molecular relaxation for vertical orientation in cylindrical block copolymer films via sharp dynamic zone annealing, *Macromolecules*, vol. 45, no. 17, 7107–7117, 2012.

[82] B. Berry, A. Bosse, J. Douglas, R. Jones and A. Karim, Orientational order in block copolymer films zone annealed below the order-disorder transition temperature, *Nano Letters*, vol. 7, no. 9, 2789–2794, 2007.

[83] J. Son, K. Gotrik and C. Ross, High-aspect-ratio perpendicular orientation of PS-b-PDMS thin films under solvent annealing, *ACS Macro Letters*, vol. 1, no. 11, 1279–1284, 2012.

[84] A. Yoshioka and K. Tashiro, Solvent effect on the glass transition temperature of syndiotactic polystyrene viewed from time-resolved measurements of infrared spectra at the various temperatures and its simulation by molecular dynamics calculation, *Macromolecules*, vol. 37, no. 2, 467–472, 2004.

[85] J. Yoon, W. Lee and E. Thomas, Highly oriented thin-film microdomain patterns of ultrahigh molecular weight block copolymers via directional solidification of a solvent, *Advanced Materials*, vol. 18, no. 20, 2691–2694, 2006.

[86] S. Shamsudin, G. Sakaguchi, M. Takenaka and H. Hasegawa, Influence of temperature and type of solvents on the microdomain orientation of PS-b-P2VP ultrathin films by solvent annealing, *Macromolecular Symposia*, vol. 327, no. 1, 72–79, 2013.

[87] Q. Yang and K. Loos, Perpendicular structure formation of block copolymer thin films during thermal solvent vapor annealing: Solvent and thickness effects, *Polymers*, vol. 9, no. 12, 525, 2017.

[88] X. Gu, I. Gunkel, A. Hexemer and T. Russell, Solvent vapor annealing of block copolymer thin films: Removal of processing history, *Colloid and Polymer Science*, vol. 292, no. 8, 1795–1802, 2014.

[89] T. Segal-Peretz, J. Ren, S. Xiong, G. Khaira, A. Bowen, L. Ocola, R. Divan, M. Doxastakis, N. Ferrier, J. de Pablo and P. Nealey, Quantitative three-dimensional characterization of block copolymer directed self-assembly on combined chemical and topographical prepatterned templates, *ACS Nano*, vol. 11, no. 2, 1307–1319, 2017.

[90] J. Mark, Ed., *Physical Properties of Polymers Handbook*, 2nd ed. New York: Springer Science & Business Media, 2007.

[91] P. Flory, *Principles of Polymer Chemistry*. New York: Cornell University Press, 1954.

[92] J. Emerson, D. Toolan, J. Howse, E. Furst and T. Epps, Determination of solvent-polymer and polymer-polymer Flory-Huggins interaction parameters for poly(3-hexylthiophene) via solvent vapor swelling, *Macromolecules*, vol. 46, no. 16, 6533–6540, 2013.

[93] S. Xiong, L. Wan, Y. Ishida, Y. Chapuis, G. Craig, R. Ruiz and P. Nealey, Directed self-assembly of triblock copolymer on chemical patterns for sub-10-nm nanofabrication via solvent annealing, *ACS Nano*, vol. 10, no. 8, 7855–7865, 2016.

[94] K. Hanley, T. Lodge and C.-I. Huang, Phase behavior of a block copolymer in solvents of varying selectivity, *Macromolecules*, vol. 33, no. 16, 5918–5931, 2000.

[95] Y. Li, H. Huang, T. He and Y. Gong, Solvent vapor induced morphology transition in thin film of cylinder forming diblock copolymer, *Applied Surface Science*, vol. 257, no. 18, 8093–8101, 2011.

[96] A. Hannon, W. Bai, A. Alexander-Katz and C. Ross, Simulation methods for solvent vapor annealing of block copolymer thin films, *Soft Matter*, vol. 11, no. 19, 3794–805, 2015.

[97] M. Chavis, D.-M. Smilgies, U. Wiesner and C. Ober, Widely tunable morphologies in block copolymer thin films through solvent vapor annealing using mixtures of selective solvents, *Advanced Functional Materials*, vol. 25, no. 20, 3057–3065, 2015.

[98] M. Paik, J. Bosworth, D.-M. Smilgies, E. Schwartz, X. Andre and C. Ober, Reversible morphology control in block copolymer films via solvent vapor processing: An in situ GISAXS study, *Macromolecules*, vol. 43, no. 9, 4253–4260, 2010.

[99] S. Rasappa, L. Schulte, D. Borah, H. Hulkkonen, S. Ndoni, T. Salminen, R. Senthamaraikannan, M. Morris and T. Niemi, Morphology evolution of PS-b-PDMS block copolymer and its hierarchical directed self-assembly on block copolymer templates, *Microelectronic Engineering*, vol. 192, 1–7, 2018.

[100] W. Bai, A. Hannon, K. Gotrik, H. Choi, K. Aissou, G. Liontos, K. Ntetsikas, A. Alexander-Katz, A. Avgeropoulos and C. Ross, Thin film morphologies of bulk-gyroid polystyrene-block-polydimethylsiloxane under solvent vapor annealing, *Macromolecules*, vol. 47, no. 17, 6000–6008, 2014.

[101] D. Lee, H. Cho, S. Yoo and S. Park, Ordering evolution of block copolymer thin films upon solvent annealing process, *Journal of Colloid and Interface Science*, vol. 383, no. 1, 118–123, 2012.

[102] J. Zhao, S. Jiang, X. Ji, L. An and B. Jiang, Study of the time evolution of the surface morphology of thin asymmetric diblock copolymer films under solvent vapor, *Polymer*, vol. 46, no. 17, 6513–6521, 2005.

[103] S. Dinachali, W. Bai, K.-H. Tu, H. Choi, J. Zhang, M. Kreider, L.-C. Cheng and C. Ross, Thermo-solvent annealing of polystyrene-polydimethylsiloxane block copolymer thin films, *ACS Macro Letters*, vol. 4, no. 5, 500–504, 2015.

[104] C. Sinturel, D. Grosso, M. Boudot, H. Amenitsch, M. Hillmyer, A. Pineau and M. Vayer, Structural transitions in asymmetric polystyrene-block-polylactide thin films induced by solvent vapor exposure, *ACS Applied Materials & Interfaces*, vol. 6, no. 15, 12146–12152, 2014.

[105] C. Jin, B. Olsen, E. Luber and J. Buriak, Nanopatterning via solvent vapor annealing of block copolymer thin films, *Chemistry of Materials*, vol. 29, no. 1, 176–188, 2017.

[106] B. Stahl, E. Kramer, C. Hawker and N. Lynd, Controlled co-solvent vapor annealing and the importance of quenching conditions in thin-film block copolymer self-assembly, *Journal of Polymer Science Part B: Polymer Physics*, vol. 55, no. 15, 1125–1130, 2017.

[107] K. Cavicchi and T. Russell, Solvent annealed thin films of asymmetric polyisoprene-polylactide diblock copolymers, *Macromolecules*, vol. 40, no. 4, 1181–1186, 2007.

[108] K. Gotrik, A. Hannon, J. Son, B. Keller, A. Alexander-Katz and C. Ross, Morphology control in block copolymer films using mixed solvent vapors, *ACS Nano*, vol. 6, no. 9, 8052–8059, 2012.

[109] J. Cushen, L. Wan, G. Pandav, I. Mitra, G. Stein, V. Ganesan, R. Ruiz, G. Willson and C. Ellison, Ordering poly(trimethylsilyl styrene-block-D,L-lactide) block copolymers in thin films by solvent annealing using a mixture of domain-selective solvents, *Journal of Polymer Science, Part B: Polymer Physics*, vol. 52, no. 1, 36–45, 2014.

[110] K. Gotrik and C. Ross, Solvothermal annealing of block copolymer thin films, *Nano Letters*, vol. 13, no. 11, 5117–5122, 2013.

[111] J. Albert, W.-S. Young, R. Lewis, T. Bogart, J. Smith and T. Epps, Systematic study on the effect of solvent removal rate on the morphology of solvent vapor annealed ABA triblock copolymer thin films, *ACS Nano*, vol. 6, no. 1, 459–466, 2012.

[112] D. Hoang, J. Yang, K. Paeng, Y. Kwon, O. Kweon and L. Kaufman, In situ multimodal monitoring of solvent vapor swelling in polymer thin films, *Review of Scientific Instruments*, vol. 87, no. 1, 015106, 2016.

[113] R. Lundy, S. Flynn, C. Cummins, S. Kelleher, M. Collins, E. Dalton, S. Daniels, M. Morris and R. Enright, Controlled solvent vapor annealing of a high-χ block copolymer thin film, *Physical Chemistry Chemical Physics*, vol. 19, no. 4, 2805–2815, 2017.

[114] A. Stenbock-Fermor, A. Knoll, A. Böker and L. Tsarkova, Enhancing ordering dynamics in solvent-annealed block copolymer films by lithographic hard mask supports, *Macromolecules*, vol. 47, no. 9, 3059–3067, 2014.

[115] G. Nelson, C. Drapes, M. Grant, R. Gnabasik, J. Wong and A. Baruth, High-precision solvent vapor annealing for block copolymer thin films, *Micromachines*, vol. 9, no. 6, 271, 2018.

[116] X. Gu, I. Gunkel, A. Hexemer and T. Russell, Controlling domain spacing and grain size in cylindrical block copolymer thin films by means of thermal and solvent vapor annealing, *Macromolecules*, vol. 49, no. 9, 3373–3381, 2016.

[117] A. Baruth, M. Seo, C. Lin, K. Walster, A. Shankar, M. Hillmyer and C. Leighton, Optimization of long-range order in solvent vapor annealed poly(styrene)-block-poly(lactide) thin films for nanolithography, *ACS Applied Materials & Interfaces*, vol. 6, no. 16, 13770–81, 2014.

[118] B. Gowd, T. Koga, M. Endoh, K. Kumar and M. Stamm, Pathways of cylindrical orientations in PS-b-P4VP diblock copolymer thin films upon solvent vapor annealing, *Soft Matter*, vol. 10, no. 39, 7753–7761, 2014.

[119] X. Gu, I. Gunkel, A. Hexemer, W. Gu and T. Russell, An in situ grazing incidence X-ray scattering study of block copolymer thin films during solvent vapor annealing, *Advanced Materials*, vol. 26, no. 2, 273–281, 2014.

[120] Y.-H. Wu, T.-Y. Lo, M.-S. She and R.-M. Ho, Morphological evolution of gyroid-forming block copolymer thin films with varying solvent evaporation rate, *ACS Applied Materials & Interfaces*, vol. 7, no. 30, 16536–16547, 2015.

[121] G. Kim and M. Libera, Morphological development in solvent-cast polystyrene-polybutadiene-polystyrene (SBS) triblock copolymer thin films, *Macromolecules*, vol. 31, no. 8, 2569–2577, 1998.

[122] S. Kim, M. Misner, T. Xu, M. Kimura and T. Russell, Highly oriented and ordered arrays from block copolymers via solvent evaporation, *Advanced Materials*, vol. 16, no. 3, 226–231, 2004.

[123] D. Posselt, J. Zhang, D.-M. Smilgies, A. Berezkin, I. Potemkin and C. Papadakis, Restructuring in block copolymer thin films: In situ GISAXS investigations during solvent vapor annealing, *Progress in Polymer Science*, vol. 66, 80–115, 2017.

[124] R. Mehra, Application of refractive index mixing rules in binary systems of hexadecane and heptadecane with n-alkanols at different temperatures, *Journal of Chemical Sciences*, vol. 115, no. 2, 147–154, 2003.

[125] N. de Nevers, Appendix A: Useful tables and charts, *Physical and Chemical Equilibrium for Chemical Engineers*, Hoboken: John Wiley & Sons, Inc., 2012, 303–317.

[126] J. Chai, D. Wang, X. Fan and J. Buriak, Assembly of aligned linear metallic patterns on silicon, *Nature Nanotechnology*, vol. 2, no. 8, 500–506, 2007.

[127] C. Rueden, J. Schindelin, M. Hiner, B. DeZonia, A. Walter, E. Arena and K. Eliceiri, ImageJ2: ImageJ for the next generation of scientific image data, *BMC Bioinformatics*, vol. 18, no. 1, 529, 2017.

[128] J. Kim, Y. Hur, J. Jeong, T. Nam, J. Lee, K. Jeon, Y. Kim and Y. Jung, Block copolymer with an extremely high block-to-block interaction for a significant reduction of line-edge fluctuations in self-assembled patterns, *Chemistry of Materials*, vol. 28, no. 16, 5680–5688, 2016.

[129] Y. Wang, M. Zhang, Y. Lai and L. Chi, Advanced colloidal lithography: From patterning to applications, *Nano Today*, vol. 22, 36–61, 2018.

[130] R. Smith, P. Lewis and P. Weiss, Patterning self-assembled monolayers, *Progress in Surface Science*, vol. 75, no. 1-2, 1–68, 2004.

[131] H. Hu, M. Gopinadhan and C. Osuji, Directed self-assembly of block copolymers: A tutorial review of strategies for enabling nanotechnology with soft matter, *Soft Matter*, vol. 10, no. 22, 3867, 2014.

[132] Y. Wang and F. Li, An emerging pore-making strategy: Confined swelling-induced pore generation in block copolymer materials, *Advanced Materials*, vol. 23, no. 19, 2134–2148, 2011.

[133] S. Park, J.-Y. Wang, B. Kim, J. Xu and T. Russell, A simple route to highly oriented and ordered nanoporous block copolymer templates, *ACS Nano*, vol. 2, no. 4, 766–772, 2008.

[134] A. van Roosmalen, J. Baggerman and S. Brader, *Dry Etching for VLSI*. Boston: Springer Science & Business Media, 1991.

[135] M. Madou, *Fundamentals of Microfabrication: The Science of Miniaturization*, 2nd ed. Boca Raton: CRC Press LLC, 2002.

[136] R. Legtenberg, H. Jansen, M. de Boer and M. Elwenspoek, Anisotropic reactive ion etching of silicon using $SF_6/O_2/CHF_3$ gas mixtures, *Journal of the Electrochemical Society*, vol. 142, no. 6, 2020–2028, 1995.

[137] H.-J. Butt, T. Müller and H. Gross, Immobilizing biomolecules for scanning force microscopy by embedding in carbon, *Journal of Structural Biology*, vol. 110, no. 2, 127–132, 1993.

[138] M. Hegner, P. Wagner and G. Semenza, Ultralarge atomically flat template-stripped Au surfaces for scanning probe microscopy, *Surface Science*, vol. 291, no. 1-2, 39–46, 1993.

[139] E. Weiss, G. Kaufman, J. Kriebel, Z. Li, R. Schalek and G. Whitesides, Si/SiO_2 -templated formation of ultraflat metal surfaces on glass, polymer, and solder supports: Their use as substrates for self-assembled monolayers, *Langmuir*, vol. 23, no. 19, 9686–9694, 2007.

[140] S. Lee, S.-S. Bae, G. Medeiros-Ribeiro, J. Blackstock, S. Kim, D. Stewart and R. Ragan, Scanning tunneling microscopy of template-stripped Au surfaces and highly ordered self-assembled monolayers, *Langmuir*, vol. 24, no. 12, 5984–5987, 2008.

[141] L.-H. Guo, J. Facci, G. McLendon and R. Mosher, Effect of gold topography and surface pretreatment on the self-assembly of alkanethiol monolayers, *Langmuir*, vol. 10, no. 12, 4588–4593, 1994.

[142] K. McPeak, S. Jayanti, S. Kress, S. Meyer, S. Iotti, A. Rossinelli and D. Norris, Plasmonic films can easily be better: Rules and recipes, *ACS Photonics*, vol. 2, no. 3, 326–333, 2015.

[143] K. Senthilkumar, L. Jiang and C. Nijhuis, Fabrication of ultra-smooth and oxide-free molecule-ferromagnetic metal interfaces for applications in molecular electronics under ordinary laboratory conditions, *RSC Advances*, vol. 7, no. 24, 14544–14551, 2017.

[144] F. Rossetti, I. Reviakine and M. Textor, Characterization of titanium oxide films prepared by the template-stripping method, *Langmuir*, vol. 19, no. 24, 10116–10123, 2003.

[145] P. Nagpal, N. Lindquist, S.-H. Oh and D. Norris, Ultrasmooth patterned metals for plasmonics and metamaterials, *Science*, vol. 325, no. 5940, 594–597, 2009.

[146] D. Yoo, T. Johnson, S. Cherukulappurath, D. Norris and S.-H. Oh, Template-stripped tunable plasmonic devices on stretchable and rollable substrates, *ACS Nano*, vol. 9, no. 11, 10647–10654, 2015.

[147] J. Kontio, H. Husu, J. Simonen, M. Huttunen, J. Tommila, M. Pessa and M. Kauranen, Nanoimprint fabrication of gold nanocones with 10 nm tips for enhanced optical interactions, *Optics Letters*, vol. 34, no. 13, 1979, 2009.

[148] P. Peijari, Change of color in metals due to nanostructures [in Finnish], B.Sc. thesis, Tampere University, Department of Engineering and Natural Sciences, 2020, 33p. Eprint available: `http://urn.fi/URN:NBN:fi:tuni-202005115185`.

[149] K. Yee, Numerical solution of initial boundary value problems involving Maxwell's equations in isotropic media, *IEEE Transactions on Antennas and Propagation*, vol. 14, no. 3, 302–307, 1966.

[150] D. Song, C. Li, W. Li and J. Watkins, Block copolymer nanocomposites with high refractive index contrast for one-step photonics, *ACS Nano*, vol. 10, no. 1, 1216–1223, 2016.

[151] A. Urbas, M. Maldovan, P. DeRege and E. Thomas, Bicontinuous cubic block copolymer photonic crystals, *Advanced Materials*, vol. 14, no. 24, 1850–1853, 2002.

[152] S. Rasappa, H. Hulkkonen, L. Schulte, S. Ndoni, J. Reuna, T. Salminen and T. Niemi, High molecular weight block copolymer lithography for nanofabrication of hard mask and photonic nanostructures, *Journal of Colloid and Interface Science*, vol. 534, 420–429, 2019.

[153] S. Vignolini, N. Yufa, P. Cunha, S. Guldin, I. Rushkin, M. Stefik, K. Hur, U. Wiesner, J. Baumberg and U. Steiner, A 3D optical metamaterial made by self-assembly, *Advanced Materials*, vol. 24, no. 10, OP23–OP27, 2012.

[154] A. Alvarez-Fernandez, K. Aissou, G. Pécastaings, G. Hadziioannou, G. Fleury and V. Ponsinet, High refractive index in low metal content nanoplasmonic surfaces from self-assembled block copolymer thin films, *Nanoscale Advances*, vol. 1, no. 2, 849–857, 2019.

[155] Z. Wong, Y. Wang, K. O'Brien, J. Rho, X. Yin, S. Zhang, N. Fang, T.-J. Yen and X. Zhang, Optical and acoustic metamaterials: superlens, negative refractive index and invisibility cloak, *Journal of Optics*, vol. 19, no. 8, 084007, 2017.

[156] A. Pap, K. Kordás, J. Vähäkangas, A. Uusimäki, S. Leppävuori, L. Pilon and S. Szatmári, Optical properties of porous silicon. Part III: Comparison of experimental and theoretical results, *Optical Materials*, vol. 28, no. 5, 506–513, 2006.

[157] N. Hutchinson, T. Coquil, A. Navid and L. Pilon, Effective optical properties of highly ordered mesoporous thin films, *Thin Solid Films*, vol. 518, no. 8, 2141–2146, 2010.

[158] B. Hatton, K. Landskron, W. Hunks, M. Bennett, D. Shukaris, D. Perovic and G. Ozin, Materials chemistry for low-k materials, *Materials Today*, vol. 9, no. 3, 22–31, 2006.

[159] Y. Yang, J. Yang, C. Liang and H. Wang, Ultra-broadband enhanced absorption of metal surfaces structured by femtosecond laser pulses, *Optics Express*, vol. 16, no. 15, 11259–11265, 2008.

[160] A. Christiansen, G. Caringal, J. Clausen, M. Grajower, H. Taha, U. Levy, A. Mortensen and A. Kristensen, Black metal thin films by deposition on dielectric antireflective moth-eye nanostructures, *Scientific Reports*, vol. 5, no. 1, 1–9, 2015.

[161] J. Hao, J. Wang, X. Liu, W. Padilla, L. Zhou and M. Qiu, High performance optical absorber based on a plasmonic metamaterial, *Applied Physics Letters*, vol. 96, no. 25, 251104, 2010.

[162] A. Tittl, P. Mai, R. Taubert, D. Dregely, N. Liu and H. Giessen, Palladium-based plasmonic perfect absorber in the visible wavelength range and its application to hydrogen sensing, *Nano Letters*, vol. 11, no. 10, 4366–4369, 2011.

[163] C. Hägglund, G. Zeltzer, R. Ruiz, I. Thomann, H.-B.-R. Lee, M. Brongersma and S. Bent, Self-assembly based plasmonic arrays tuned by atomic layer deposition for extreme visible light absorption, *Nano Letters*, vol. 13, 3352–3357, 2013.

[164] S. Ghosh and T. Pal, Interparticle coupling effect on the surface plasmon resonance of gold nanoparticles: From theory to applications, *Chemical Reviews*, vol. 107, no. 11, 4797–4862, 2007.

[165] Z. Liu, X. Liu, S. Huang, P. Pan, J. Chen, G. Liu and G. Gu, Automatically acquired broadband plasmonic-metamaterial black absorber during the metallic film-formation, *ACS Applied Materials & Interfaces*, vol. 7, no. 8, 4962–4968, 2015.

[166] B. Sturmberg, T. Chong, D.-Y. Choi, T. White, L. Botten, K. Dossou, C. Poulton, K. Catchpole, R. McPhedran and M. de Sterke, Total absorption of visible light in ultrathin weakly absorbing semiconductor gratings, *Optica*, vol. 3, no. 6, 556, 2016.

[167] S. Kim, J. Park, M. Esfandyarpour, E. Pecora, P. Kik and M. Brongersma, Superabsorbing, artificial metal films constructed from semiconductor nanoantennas, *Nano Letters*, vol. 16, no. 6, 3801–3808, 2016.

[168] C. Hu, L. Liu, Z. Zhao, X. Chen and X. Luo, Mixed plasmons coupling for expanding the bandwidth of near-perfect absorption at visible frequencies, *Optics Express*, vol. 17, no. 19, 16745–16749, 2009.

[169] G. Akinoglu, S. Mir, R. Gatensby, G. Rydzek and P. Mokarian-Tabari, Block copolymer derived vertically coupled plasmonic arrays for surface-enhanced Raman spectroscopy, *ACS Applied Materials & Interfaces*, vol. 12, no. 20, 23410–23416, 2020.

[170] H. Jin, J. Kim, M. Heo, S.-J. Jeong, B. Kim, S. Cha, K. Han, J. Kim, G. Yang, J. Shin and S. Kim, Ultralarge area sub-10 nm plasmonic nanogap array by block copolymer self-assembly for reliable high-sensitivity SERS, *ACS Applied Materials & Interfaces*, vol. 10, no. 51, 44660–44667, 2018.

[171] M. Rycenga, X. Xia, C. Moran, F. Zhou, D. Qin, Z.-Y. Li and Y. Xia, Generation of hot spots with silver nanocubes for single-molecule detection by surface-enhanced Raman scattering, *Angewandte Chemie International Edition*, vol. 50, no. 24, 5473–5477, 2011.

[172] H. Robatjazi, S. Bahauddin, C. Doiron and I. Thomann, Direct plasmon-driven photoelectrocatalysis, *Nano Letters*, vol. 15, no. 9, 6155–6161, 2015.

[173] M. Park, C. Harrison, P. Chaikin, R. Register and D. Adamson, Block copolymer lithography: Periodic arrays of ~ 10^{11} holes in 1 square centimeter, *Science*, vol. 276, no. 5317, 1401–1404, 1997.

[174] C. M. Bates and F. Bates, 50th Anniversary perspective: Block polymers - Pure potential, *Macromolecules*, vol. 50, no. 1, 3–22, 2017.

[175] M. Somervell, R. Gronheid, J. Hooge, K. Nafus, P. Rincon Delgadillo, C. Thode, T. Younkin, K. Matsunaga, B. Rathsack, S. Scheer and P. Nealey, Comparison of

directed self-assembly integrations, *Proc. SPIE 8325, Advances in Resist Materials and Processing Technology XXIX*, 2012, 83250G.

[176] C. Sinturel, M. Vayer, M. Morris and M. Hillmyer, Solvent vapor annealing of block polymer thin films, *Macromolecules*, vol. 46, no. 14, 5399–5415, 2013.

PUBLICATIONS

PUBLICATION I

Block copolymer patterning for creating porous silicon thin films with tunable refractive indices

H. Hulkkonen, T. Salminen and T. Niemi

ACS Applied Materials & Interfaces, vol. 9, no. 37, (2017), 31260–31265
DOI: 10.1021/acsami.6b16110

ACS APPLIED MATERIALS & INTERFACES

Forum Article

www.acsami.org

Block Copolymer Patterning for Creating Porous Silicon Thin Films with Tunable Refractive Indices

Hanna H. Hulkkonen,* Turkka Salminen, and Tapio Niemi

Optoelectronics Research Centre, Tampere University of Technology, Korkeakoulunkatu 3, 33720 Tampere, Finland

Supporting Information

ABSTRACT: We investigated the use of block copolymer (BCP) self-assembly for tuning the optical properties of silicon. We fabricated porous silicon by etching a hexagonally ordered pore pattern onto the surface of silicon wafers using poly(styrene-2-vinylpyridine) to prepare the etch mask. Contrary to typical BCP lithography, we did not need to use a range of different polymers to vary the pore size. We used the dry etching time as a way to increase the pore diameter and thus the porosity. The optical properties of the fabricated porous thin films were characterized by two effective medium approximations. Both the volume-averaging theory and the 2D Maxwell−Garnett theory gave similar effective refractive index values, although the latter was more accurate in predicting the film porosity. The refractive indices of the produced thin films could be varied by controlling the porosity. A maximum decrease of 30% in the refractive index was observed at 34% porosity compared to bulk silicon. We also demonstrated over a 60% decrease in the reflectance of silicon at 500 nm wavelength. The presented BCP method can be used to tailor semiconductor and dielectric layers for photonic applications without the size limitations of conventional lithography or the unpredictability of other pore-forming fabrication methods.

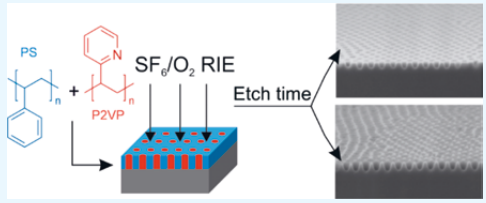

KEYWORDS: *block copolymer, nanolithography, porous silicon, tunable refractive index, effective medium approximation*

INTRODUCTION

Block copolymers (BCPs) have been of interest in the fabrication of porous media because of their ability to self-assemble into highly ordered periodic structures. The cylindrical morphology is of particular interest because it allows the minor domain to be selectively removed to form an organized array of evenly sized holes. The size of the holes is usually controlled by selecting a BCP with the appropriate molecular weight. Subtle changes to the polymer microdomain size can be done by blending in homopolymers that segregate to the cylindrical domains and enlarge their size.[1] The domain removal conditions can also affect the size of the fabricated pores, as shown by Yin et al. in a study that used selective swelling of one polymer domain at varying temperatures.[2] The method used for domain removal depends on the BCP chemistry and includes processes such as selective swelling,[2] ozonolysis,[3] or degradation by UV irradiation, followed by solvent treatment.[4] The versatility of BCPs has made them desirable tools to produce precisely tailored nanoporous materials that can be of use in multiple applications including filtration,[5] catalysis,[6] and nanolithography.[7]

Lithographic patterning of semiconductors using BCPs was demonstrated early on by Park et al.[3] Since then, BCPs have proven to be very useful as templates for fabricating dense arrays of dotted and line patterns and, more recently, also gyroidal structures with unique optical properties.[8] The BCP pattern is transferred onto the underlying substrate either by etching or by using the BCP as a template for material deposition. Typical BCPs are not very resistant to etching methods so successful pattern transfer may be problematic. A comprehensive review by Cummins et al. lists various strategies, including sequential infiltration synthesis, atomic layer deposition, and metal evaporation, that can be used to incorporate inorganic materials into BCP films and enhance the durability of the BCP etch masks.[9] Etch-resistant BCP patterns can also be made directly using polymers in which one block contains inorganic moieties such as in poly(dimethylsiloxane), which forms a durable silicon oxide hard mask after oxidation. However, we are more interested in BCPs containing a multipurpose poly(vinylpyridine) (PVP) block that can be either bonded with etch contrast agents or selectively removed without etching. For the mask to function correctly, the BCP features have to be oriented perpendicular to the substrate surface. The orientation and alignment of cylindrical domains have been extensively studied using neutral brush layers,[10] topographic confinement,[11] electrical fields,[12] and solvent evaporation treatments.[13]

The incorporation of holes into a bulk semiconductor significantly affects the optical and electrical properties of the material. The porous thin film is considered a nanocomposite

Special Issue: Block Copolymers for Nanotechnology Applications

Received: December 15, 2016
Accepted: February 2, 2017
Published: February 14, 2017

DOI: 10.1021/acsami.6b16110
ACS Appl. Mater. Interfaces 2017, 9, 31260−31265

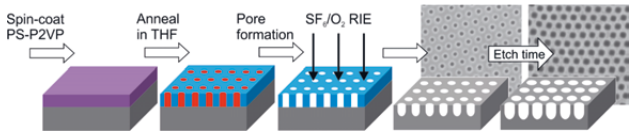

Figure 1. Experimental procedure for preparing porous thin-film masks from PS-P2VP and controlling the porosity of silicon by reactive-ion etching.

consisting of a solid matrix with nanoscale inclusions of air. The size of the inclusions must be much smaller than the wavelength of light so that the light only experiences the collective response of the composite material and not that of the individual structures. Gases, such as air, have very low refractive indices because of their low density. The addition of air effectively reduces the refractive index of the porous material. The effective electromagnetic properties of nanoporous materials can be described using numerous effective medium approximations (EMAs). Some of the most common EMAs are the Maxwell−Garnett theory, Bruggeman's model, the Lorentz−Lorenz equation, and the volume-averaging theory (VAT).[14] Most EMAs have been derived for certain nanocomposite architectures and measuring arrangements. Owing to the amount of models available and their validity limitations, there is some uncertainty on what models to use when describing nanoporous materials. A study by Braun and Pilon concluded that for cylindrically shaped pores the effective optical properties could be calculated based solely on the porosity and that the film thickness, pore shape, and distribution were insignificant.[15] We observed based on experimental and theoretical works[14−17] that, depending on the optical measurement setup and light polarization, the effective refractive index predictions that best complied with porous silicon were achieved using either the VAT or 2D Maxwell−Garnett theory (2D MGT). The VAT assumes arbitrarily shaped and distributed inclusions, while the 2D MGT is derived for films with monodisperse, cylindrical inclusions.[14,17]

Porous silicon thin films have found use as refractive-index-tailored waveguides, antireflection coatings, Bragg reflectors, and biosensors because of their tunable properties and the ease of integration into semiconductor device fabrication. The effective properties can be controlled by altering the degree of porosity, but the typical porous silicon fabrication methods produce somewhat unpredictable pore structures. Porous silicon has typically been fabricated by electrochemical anodization of doped silicon in solutions containing hydrofluoric acid. The resultant pore structure and size distribution depend on processing conditions such as the current density, electrolyte concentration, substrate doping, etch time, and temperature.[18]

Here we demonstrate a straightforward way of fabricating silicon thin films with controlled porosity and a highly organized pore structure using poly(styrene-2-vinylpyridine) BCP lithography. We characterize the fabricated porous thin films using spectrophotometry with transverse electric (TE) polarized light and estimate the optical properties of the porous films using the VAT and 2D MGT.

EXPERIMENTAL SECTION

Materials. The asymmetrical BCP poly(styrene-2-vinylpyridine) (PS-P2VP; M_n = 135 and 53 kg/mol for PS and P2VP, respectively, and PDI = 1.18) was purchased from Polymer Source Inc. and used as received without purification. Anhydrous toluene and tetrahydrofuran (THF) were purchased from Sigma-Aldrich. Commercial, laboratory-grade 2-propanol and ethanol were also used.

Fabrication of a BCP Mask. Silicon wafers were cleaned with 2-propanol and used with the native oxide layer intact. Due to the relatively high molecular weight of the PS-P2VP, the polymer was dissolved in a 70:30 mixture of toluene and THF and stirred for over 12 h to ensure complete dissolution. A 1−1.5 w/v-% solution was spin-coated onto the substrates at 3000 rpm for 60s. We used a closed chamber SSE OPTIcoat spinner for better film uniformity. Samples were immediately baked on a hot plate at 125 °C for 2 min followed by controlled solvent-vapor annealing in THF for 5 to 10 min. The PS-P2VP created a hexagonally arranged dot pattern with an average center-to-center distance of 74 nm.

Silicon Etching Using a BCP Mask. To fabricate the nanoporous template, P2VP domains were selectively swelled and made to collapse, creating cylindrical, perpendicularly oriented pores. Selective swelling was done by immersing the samples in ethanol at room temperature for 30 min, after which the samples were blow-dried with nitrogen. The highly ordered porous templates were then used as dry etch masks without further treatment. Dry etching of silicon was carried out using reactive-ion etching in SF_6/O_2 plasma with either 80 or 160 W radio-frequency (RF) power (12/9 sccm, 30 mTorr pressure, Oxford Plasmalab System 100). We investigated the effect of different etching times on the pattern transfer. After silicon etching, polymer residues were removed during a brief O_2 plasma treatment (30 sccm, 100 W RF power, 100 mTorr pressure). The workflow of the BCP nanopatterning process is illustrated in Figure 1.

Film Characterization. The surface morphologies of the annealed BCP thin films and the etched silicon wafers were examined using a field-emission scanning electron microscope (Zeiss Ultra 55) with 0.8−3 kV acceleration voltage. For quality control, the thickness of the BCP masks was determined using a laser ellipsometer (Rudolph Research AutoEL III) with a helium−neon laser at a 70° incident angle. Porosity and pore-size analysis was performed on 3.8 × 2.85 μm SEM images using Fiji, an open-source scientific image processing software based on *ImageJ*. Automatic image thresholding was used to minimize user bias, and a particle analysis tool was used to calculate the porosity, average pore size, and standard deviation from the converted binary images.

Optical Measurements. Reflectance of the etched silicon wafers was measured using a PerkinElmer Lambda 1050 spectrophotometer with a universal reflectance accessory. We used an incident angle of 8°, a rectangular beam shape with an area of 5 × 5 mm^2, and TE polarization, where the electric field vector is perpendicular to the cylinders. The reflectance data were fitted to a model consisting of a bulk silicon substrate and a layer with an effective refractive index determined by the layer porosity. Fitting was done using a transfer-matrix method that used the volume fraction of air f_v and film thickness h as fitting parameters.[19]

The effective refractive index was determined by applying the VAT and 2D MGT[14] and utilizing refractive index values for bulk silicon and air.[20] These theories approximate the complex refractive index, where the real part n is the refractive index and the imaginary part k is the extinction coefficient of the nanocomposite thin film. The complex effective refractive index ($n_{eff} - jk_{eff}$) given by the VAT is defined by

$$n_{eff}^2 = \frac{1}{2}\left(A + \sqrt{A^2 + B^2}\right) \quad (1)$$

$$k_{eff}^2 = \frac{1}{2}\left(-A + \sqrt{A^2 + B^2}\right) \quad (2)$$

DOI: 10.1021/acsami.6b16110
ACS Appl. Mater. Interfaces 2017, 9, 31260−31265

where

$$A = f_v(n_{air}^2) + (1 - f_v)(n_{Si}^2 - k_{Si}^2)$$

and

$$B = 2n_{Si}k_{Si}(1 - f_v)$$

and by the 2D MGT, it is

$$(n_{eff} - jk_{eff})^2 = n_c^2\left[1 - \frac{2f_v(n_c^2 - n_i^2)}{n_c^2 + n_i^2 + f_v(n_c^2 - n_i^2)}\right] \quad (3)$$

The complex notations $n_c = n_{Si} - jk_{Si}$ and $n_i = n_{air} - jk_{air} = n_{air}$ contain the refractive indices and extinction coefficients of silicon (subscript "Si") and air (subscript "air"). The volume fraction (porosity) of air in the thin film is denoted as f_v.

RESULTS AND DISCUSSION

PS-P2VP was spin-coated onto solvent-cleaned silicon wafers, resulting in polymer films with an initially disorganized morphology and a film thickness of 43−55 nm. The BCP films were subjected to controlled solvent-vapor flow annealing using a metal chamber and a N_2-bubbler system similar to the one presented by Jin et al.[21] A perpendicular orientation of the P2VP cylinders was achieved by annealing in THF for 10 min, followed by fast quenching.

The selective swelling of P2VP in room temperature ethanol for 30 min produced an open-pore polymer mask with an estimated hole diameter of 27 nm. The prevailing theory explaining the pore formation in PS-P2VP is that, because of the constriction of the PS matrix, the selective solvent swells the P2VP chains up and out from the cylinders, and after drying, the chains collapse onto the film surface and pore walls.[2] The holes in our BCP films were spatially arranged in a highly ordered hexagonal pattern in similarly oriented grains (grain diameter of 1 μm or larger) that covered the whole substrate surface. No dewetting was observed on the 1 and 4 cm^2 wafer pieces. The mask fabrication could easily be scaled up to larger wafers, and the main limiting factor is the solvent annealing chamber that currently fits a maximum wafer size of 2 in.

We were able to fabricate silicon thin films with increasing pore sizes without having to use a wide range of BCPs with different molecular weights. The silicon thin films with pore diameters ranging from 26 to 58 nm were all created using a single polymer and an etch mask that always had the same initial hole diameter (approximately 27 nm). The change in the pore size arose from the tuning of the dry etching time, which was varied from 15 s to a maximum of 50 s. The gradual lateral etching of the BCP mask widened the hole openings, which resulted in larger pores etched into silicon until neighboring pores began to limit the growth. The lateral widening was more apparent after longer etching times, as seen in Table 1. In addition to variations in the pore width, also the pore depth varied with the etching time from 42 nm to a maximum of 60 nm for lightly etched samples (Figure 2A,B). A loss of pore depth and a change in the pore profile were observed after longer etching times, which was likely a result of etching away first the BCP mask and then the cylinder structures (Figure 2C). We also tried using a lower RF power of 80 W instead of 160 W, but the etch was too isotropic and did not produce clear pore structures.

Optical Characterization. The progressive increase in the pore diameter resulted in an increase in the film porosity, as calculated by image analysis. All porous thin films displayed a decrease in the measured reflectance compared to bare silicon (Figure 3). Furthermore, the decrease in the overall reflectance at 500−900 nm was observed to follow the increase in the film porosity up to a point (Figure 3A−D). A visible color change was observed in the samples starting from a light-blue tint and reaching a dark-blue color at approximately 34% porosity (pore diameter 45 nm). The dark-blue films also had the lowest reflectance, with a maximum 62% decrease in reflectance at 500 nm wavelength.

Table 1. Characteristics of the Porous Thin Films Based on SEM Image Analysis and Model Fitting[a]

	image analysis		modeling		
etching time [s]	pore diameter [nm]	porosity [%]	2D MGT f_v [%]	VAT f_v [%]	h [nm]
15	26.2 ± 1.9	11.7	11.9	20.7	21
20	30.5 ± 2.1	17.1	19.2	31.3	30
15	31.6 ± 1.6	18.0	22.0	35.0	34
20	40.9 ± 2.8	29.4	29.2	44.1	36
20	44.8 ± 2.6	34.0	38.4	54.5	38
40	49.2 ± 3.5	42.9	29.3	44.0	26
30	57.6 ± 6.4	57.8	31.8	47.4	25

[a] f_v = volume fraction of air; h = modeled layer thickness.

However, thin films with over 40% estimated porosity did not follow the trend in decreasing reflectance, and a relapse of the reflectance toward that of pure silicon was seen (Figure 3E,F). This behavior can be explained by examining the cross sections of the porous thin films. The thin films that appear to have a high porosity in top-down SEM images have actually lost the cylindrical pore shape and only have very shallow (25−35 nm) spherical indentations due to mask erosion and over-etching (Figure 2C). Therefore, surface image analysis did not give a realistic approximation of the porosity for these thin films. Because the actual film porosity was lower than estimated, the overall decrease in the reflectance was not as large as was expected.

To further study the optical properties of the thin films, they were modeled as homogeneous layers with a thickness h and an air volume fraction f_v according to the VAT and 2D MGT. The fitted reflectance models agreed very well with the measurement data, as seen in Figure 3 (the 2D MGT fit displayed). Both the VAT and 2D MGT models produced similar fits with a maximum difference of 0.8%. There is a discrepancy between the measured and modeled reflectance in the ultraviolet region, and the effect is more pronounced as the pore size grows. At shorter wavelengths, the pores are likely becoming too large to be considered subwavelength nanostructures for modeling using the effective medium approach. Similarly, Pap et al. observed a difference between the experimental and theoretical reflectance and attributed it to enhanced Rayleigh scattering from the pores at short wavelengths.[16] The EMAs do not account for the intensity loss caused by scattering.

The 2D MGT was accurate in calculating the volume fraction f_v of the cylindrically porous thin films under 40% porosity (Figure 4A). The volume fraction f_v ranging from 11.9 to 38.4 was observed to correspond to porosity values of 11.7−34.0% estimated via SEM image analysis. The small variations between the measured and modeled porosities can be attributed to uncertainties in the image analysis method. The VAT was not as effective in calculating the porosity, and it overestimated the film porosity in increasing amounts (Figure 4A). The

DOI: 10.1021/acsami.6b16110
ACS Appl. Mater. Interfaces 2017, 9, 31260−31265

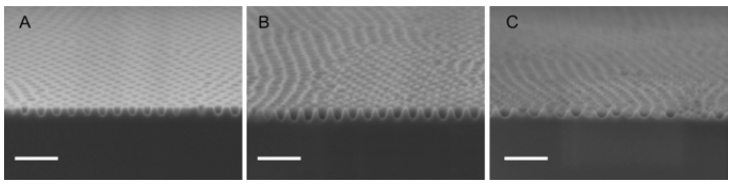

Figure 2. Etch profile of porous silicon thin films with (A) 15, (B) 20, and (C) 40 s of etching in SF_6/O_2. A lateral widening of the pores is seen, and overetching is apparent after longer etching times. The scale bars are 200 nm.

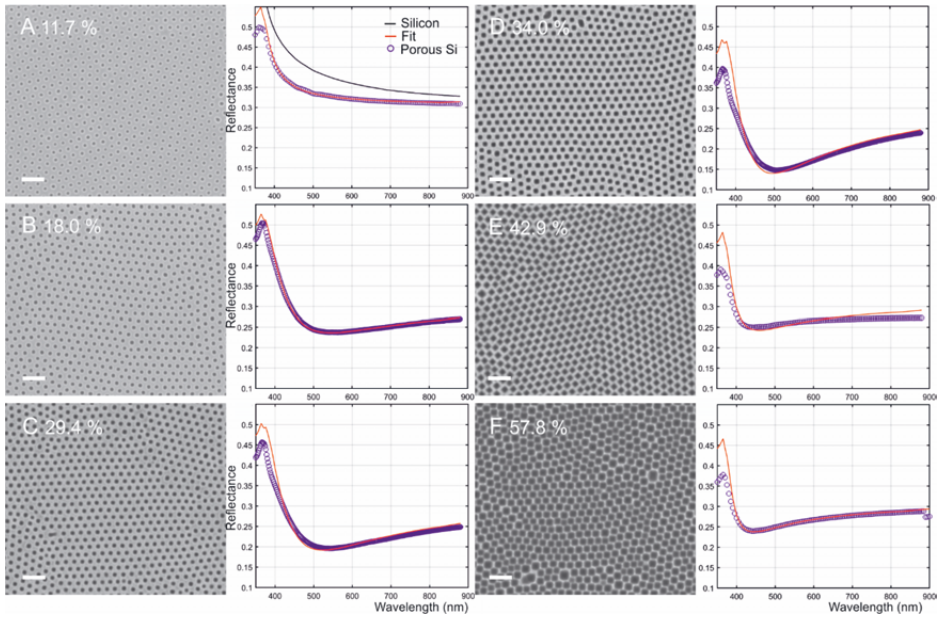

Figure 3. SEM images and measured reflectance spectra from porous silicon thin films with porosities of (A) 11.7%, (B) 18.0%, (C) 29.4%, (D) 34.0%, (E) 42.9%, and (F) 57.8%. The reflectance of all porous films (blue) differed from the bare silicon reference (A, black). The reflectance was also modeled (red) using the porosity f_v and thickness h as fitting parameters. The scale bars are 200 nm.

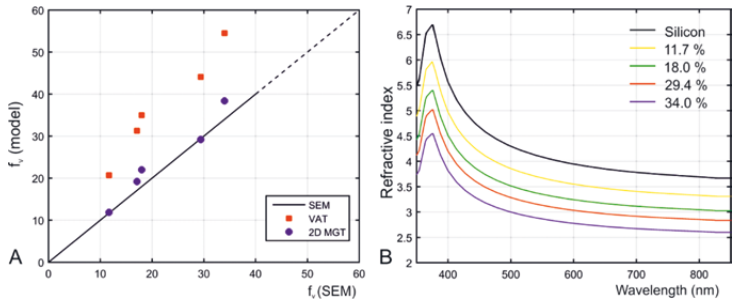

Figure 4. (A) Comparison of the porosity values acquired via data fitting of the VAT and 2D MGT. The line labeled "SEM" is a guide to the eye. (B) Effective refractive indices of porous silicon calculated by fitting the 2D MGT of the thin films to the optical reflectance.

differences between the two models arise from the differing assumptions concerning the pore structure. Another concern is that the measurement configuration and light polarization affect the reflectance and predicted properties of cylindrically porous films because of the anisotropy of the thin films.[14] Here we note that when using light polarization where the electric field

DOI: 10.1021/acsami.6b16110
ACS Appl. Mater. Interfaces 2017, 9, 31260−31265

vector is perpendicular to the cylinders, the 2D MGT has better predictive power. The estimated pore size, the porosity of the thin films, and the 2D MGT and VAT fitting parameters are summarized in Table 1.

For overetched films (diameter >49 nm, porosity >40%), both models computed a decreased optical thickness and a reduced volume fraction. Because the profile of the pores changed during overetching, the reliability of the EMAs is questionable. For example, the 2D MGT model is derived for cylindrical inclusions, and it will likely not give reliable predictions concerning the physical and optical properties of films with spherical indentations. We think that the simple EMAs for a single thin-film layer are not appropriate for comparing samples with different 3D architectures.

Despite their differences in interpreting the volume fraction, both EMAs gave acceptable predictions concerning the complex refractive indices. The relative differences between the indices given by the two models were under 0.5%. The extinction coefficient k showed little change as a result of increased porosity (Figures S1 and S2). However, at short wavelengths, scattering and pore-size-related losses likely caused aberrations to the models. In principle, most EMAs have been developed for estimating the real part of the effective refractive index. Nevertheless, the imaginary part can also be estimated with some restrictions, as proposed by Hutchinson et al.[14]

A gradual decrease in the effective refractive index was observed in cylindrically porous silicon thin films, as shown in Figure 4B. The lowest refractive index was achieved with a surface porosity of 34%, and the thin film displayed a 30% change compared to bulk silicon. Low-index materials are particularly desirable in broad-band antireflection coatings and optical devices that require a high-index contrast such as waveguides and microresonators.[22] Solid, naturally occurring semiconductor materials with indices smaller than 1.4 do not really exist. Extremely low-index semiconductors could be realized by selecting substrate materials that already have a low refractive index and incorporating air-filled pores onto the substrate surface using BCP lithography. The fact that the substrate and porous surface layer are both from the same material reduces the processing steps needed and is an advantage in semiconductor device fabrication.

CONCLUSIONS

In conclusion, we have demonstrated that the optical properties of silicon can be tuned using a simple process of BCP lithography. First, arrays of perpendicularly oriented cylinders were obtained with a brief solvent-vapor treatment, where no substrate surface modifications or neutral layers were needed. Second, etch masks were formed by the selective removal of one BCP component, and the resulting hole structure was transferred to silicon using SF_6/O_2 etching. The etched pore structure was spatially highly ordered and uniform over the whole wafer surface. The diameter of the pores, and hence the porosity of silicon, could be increased with the etching time up to a point where the neighboring pores began to limit the growth. The method presented here allows a broad porosity range to be reached with a single BCP. The molecular weight of the selected BCP determines the periodicity of the pores and sets the minimum accessible pore size. The effective refractive indices of porous silicon thin films could be determined by fitting either the 2D MGT or VAT model parameters to the measured reflectance spectra. Both EMAs agreed on the refractive index values, but the 2D MGT was more realistic in estimating the film porosity.

By increasing the porosity, we were able to decrease the reflectance and lower the refractive index of silicon. We demonstrated at maximum a 62% decrease in the reflectance and a 30% decrease in the refractive index of silicon at 500 nm wavelength using porous films. The optical properties can be further tuned by selecting BCPs with higher or lower molecular weights or by further optimizing the dry etching process. The proposed method can also easily be extended to suit other substrate materials and wafer sizes, thus offering a universal way to manipulate the optical properties of semiconductor and dielectric materials.

ASSOCIATED CONTENT

Supporting Information

The Supporting Information is available free of charge on the ACS Publications website at DOI: 10.1021/acsami.6b16110.

Wavelength-dependent extinction coefficients of porous silicon films estimated using the 2D MGT (PDF)

AUTHOR INFORMATION

Corresponding Author

*E-mail: hanna.hulkkonen@tut.fi.

ORCID

Hanna H. Hulkkonen: 0000-0003-1206-3060

Author Contributions

The manuscript was written through contributions of all authors. All authors have given approval to the final version of the manuscript.

Funding

We acknowledge funding from the Academy of Finland via the projects Photonics QCA (Decision No. 263594) and PerforMant (Decision No. 284652).

Notes

The authors declare no competing financial interest.

REFERENCES

(1) Peng, J.; Gao, X.; Wei, Y.; Wang, H.; Li, B.; Han, Y. Controlling the Size of Nanostructures in Thin Films via Blending of Block Copolymers and Homopolymers. *J. Chem. Phys.* **2005**, *122*, 1−7.

(2) Yin, J.; Yao, X.; Liou, J. Y.; Sun, W.; Sun, Y.; Wang, Y. Membranes with Highly Ordered Straight Nanopores by Selective Swelling of Fast Perpendicularly Aligned Block Copolymers. *ACS Nano* **2013**, *7*, 9961−9974.

(3) Park, M.; Harrison, C.; Chaikin, P. M.; Register, R. A.; Adamson, D. H. Block Copolymer Lithography: Periodic Arrays of Periodic Arrays of ∼ 10^{11} Holes in 1 Square Centimeter. *Science* **1997**, *276*, 1401−1404.

(4) Xu, T.; Kim, H.-C.; DeRouchey, J.; Seney, C.; Levesque, C.; Martin, P.; Stafford, C. M.; Russell, T. P. The Influence of Molecular Weight on Nanoporous Polymer Films. *Polymer* **2001**, *42*, 9091−9095.

(5) Phillip, W. A.; O'Neill, B.; Rodwogin, M.; Hillmyer, M. A.; Cussler, E. L. Self-Assembled Block Copolymer Thin Films as Water Filtration Membranes. *ACS Appl. Mater. Interfaces* **2010**, *2*, 847−853.

(6) Hilke, R.; Pradeep, N.; Madhavan, P.; Vainio, U.; Behzad, A. R.; Sougrat, R.; Nunes, S. P.; Peinemann, K.-V. Block Copolymer Hollow Fiber Membranes with Catalytic Activity and pH-Response. *ACS Appl. Mater. Interfaces* **2013**, *5*, 7001−7006.

(7) Bang, J.; Jeong, U.; Ryu, D. Y.; Russell, T. P.; Hawker, C. J. Block Copolymer Nanolithography: Translation of Molecular Level Control to Nanoscale Patterns. *Adv. Mater.* **2009**, *21*, 4769−4792.

DOI: 10.1021/acsami.6b16110
ACS Appl. Mater. Interfaces 2017, 9, 31260−31265

(8) Salvatore, S.; Demetriadou, A.; Vignolini, S.; Oh, S. S.; Wuestner, S.; Yufa, N. A.; Stefik, M.; Wiesner, U.; Baumberg, J. J.; Hess, O.; Steiner, U. Tunable 3D Extended Self-Assembled Gold Metamaterials with Enhanced Light Transmission. *Adv. Mater.* **2013**, *25*, 2713−2716.
(9) Cummins, C.; Ghoshal, T.; Holmes, J. D.; Morris, M. A. Strategies for Inorganic Incorporation Using Neat Block Copolymer Thin Films for Etch Mask Function and Nanotechnological Application. *Adv. Mater.* **2016**, *28*, 5586−5618.
(10) Ham, S.; Shin, C.; Kim, E.; Ryu, D. Y.; Jeong, U.; Russell, T. P.; Hawker, C. J. Microdomain Orientation of PS-B-PMMA by Controlled Interfacial Interactions. *Macromolecules* **2008**, *41*, 6431−6437.
(11) Durand, W. J.; Carlson, M. C.; Maher, M. J.; Blachut, G.; Santos, L. J.; Tein, S.; Ganesan, V.; Ellison, C. J.; Willson, C. G. Experimental and Modeling Study of Domain Orientation in Confined Block Copolymer Thin Films. *Macromolecules* **2016**, *49*, 308−316.
(12) Thurn-Albrecht, T.; Derouchey, J.; Russell, T. P.; Jaeger, H. M. Overcoming Interfacial Interactions with Electric Fields. *Macromolecules* **2000**, *33*, 3250−3253.
(13) Kim, S. H.; Misner, M. J.; Xu, T.; Kimura, M.; Russell, T. P. Highly Oriented and Ordered Arrays from Block Copolymers via Solvent Evaporation. *Adv. Mater.* **2004**, *16*, 226−231.
(14) Hutchinson, N. J.; Coquil, T.; Navid, A.; Pilon, L. Effective Optical Properties of Highly Ordered Mesoporous Thin Films. *Thin Solid Films* **2010**, *518*, 2141−2146.
(15) Braun, M. M.; Pilon, L. Effective Optical Properties of Non-Absorbing Nanoporous Thin Films. *Thin Solid Films* **2006**, *496*, 505−514.
(16) Pap, A. E.; Kordás, K.; Vähäkangas, J.; Uusimäki, A.; Leppävuori, S.; Pilon, L.; Szatmári, S. Optical Properties of Porous Silicon. Part III: Comparison of Experimental and Theoretical Results. *Opt. Mater. (Amsterdam, Neth.)* **2006**, *28*, 506−513.
(17) Navid, A.; Pilon, L. Effect of Polarization and Morphology on the Optical Properties of Absorbing Nanoporous Thin Films. *Thin Solid Films* **2008**, *516*, 4159−4167.
(18) Sailor, M. Fundamentals of Porous Silicon Preparation. *Porous Silicon in Practice: Preparation, Characterization and Applications*; Wiley-VCH: Weinheim, Germany, 2012; pp 1−42.
(19) Yeh, P. *Optical Waves in Layered Media*; Wiley-Interscience: Hoboken, NJ, 2005.
(20) Aspnes, D. E.; Studna, A. A. Dielectric Functions and Optical Parameters of Si, Ge, GaP, GaAs, GaSb, InP, InAs, and InSb from 1.5 to 6.0 eV. *Phys. Rev. B: Condens. Matter Mater. Phys.* **1983**, *27*, 985−1009.
(21) Jin, C.; Olsen, B. C.; Luber, E. J.; Buriak, J. M. Nanopatterning via Solvent Vapor Annealing of Block Copolymer Thin Films. *Chem. Mater.* **2017**, *29*, 176−188.
(22) Schubert, E. F.; Kim, J. K.; Xi, J.-Q. Low-Refractive-Index Materials: A New Class of Optical Thin-Film Materials. *Phys. Status Solidi B* **2007**, *244*, 3002−3008.

DOI: 10.1021/acsami.6b16110
ACS Appl. Mater. Interfaces 2017, 9, 31260−31265

PUBLICATION II

All-metal broadband optical absorbers based on block copolymer nanolithography

H. Hulkkonen, A. Sah and T. Niemi

ACS Applied Materials & Interfaces, vol. 10, no. 49, (2018), 42941–42947
DOI: 10.1021/acsami.8b17294

ACS APPLIED MATERIALS & INTERFACES

Research Article

Cite This: ACS Appl. Mater. Interfaces 2018, 10, 42941−42947

www.acsami.org

All-Metal Broadband Optical Absorbers Based on Block Copolymer Nanolithography

Hanna Hulkkonen,* Aashish Sah, and Tapio Niemi

Laboratory of Photonics, Tampere University of Technology, P. O. Box 692, 33101 Tampere, Finland

Supporting Information

ABSTRACT: The growing interest in solar energy during recent years has spurred on the development of high-efficiency optical absorbers using emerging concepts in plasmonics and metamaterials. Most absorber designs require patterning on a subwavelength scale, making large-scale fabrication expensive or impractical. This study presents an all-metal metasurface with tightly packed, sub-80 nm nanodomes fabricated by template-stripping thin gold films from reusable silicon templates. Subwavelength patterning was achieved via molecular self-assembly of block copolymers, which enables large-area, periodic patterning with nanometer precision. The proposed nanodome surface acts as an optical absorber capable of absorbing 97% of incident light in the visible range 320−650 nm, and still more than 90% at high incidence angles. We demonstrate both experimentally and theoretically that the absorption behavior of the thin film can be controlled by changing the size of the nanodomes, namely, the gap between the structures. The enhanced absorption of light is attributed to localized particle plasmon and gap plasmon resonances. This research provides a straightforward and cost-effective strategy to design and fabricate thin, large-area, light-absorbing coatings that can be transferred onto nearly any rigid or flexible substrate. The all-metal metasurfaces are a promising candidate for plasmon-induced hot electron generation for efficient solar energy conversion in photovoltaic and photocatalytic devices.

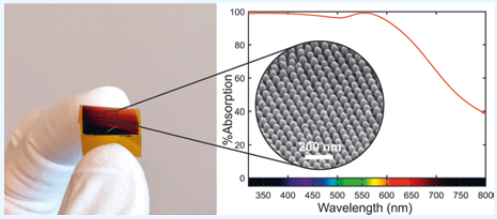

KEYWORDS: *ultrathin plasmonic absorbers, broadband optical absorption, localized surface plasmon resonance, subwavelength structures, template-stripping, block copolymer lithography*

INTRODUCTION

Photon absorption is a fundamental part of the operation of photodetectors, solar cells, photothermal devices, and optical filters. Considerable effort has been put into creating perfect absorbers—materials that efficiently absorb light either in a narrow or broad wavelength range. Various schemes for realizing absorption using metal structures have been introduced. Perfect optical absorbers have been achieved using thick porous foams,[1,2] lossy thin films on metal substrates to improve impedance matching,[3] and metallic nanopillars[4] or needles[5] with a gradual refractive index change. Advances in nanofabrication methods have led to the rise of metamaterial and metasurface absorbers with tunable properties. These types of absorbers are based on subwavelength elements and are often characterized as effective materials. Previous absorber designs are variations of a triple-layer stack consisting of a periodic metal pattern, a dielectric spacer, and a bottom reflector. These metal−insulator−metal structures (MIMs) have been used to demonstrate perfect absorption first at infrared[6,7] and later also at visible frequencies.[8,9] However, in a MIM structure, near-unity absorption typically occurs only within a very narrow wavelength range defined by the thickness of the spacer. Broader absorption bands have been achieved using asymmetric or mixed-size nanostructures in the top metal layer to excite multiple resonances.[10−14]

A less explored method for achieving broadband visible light absorption is to pattern plasmonic metals. The benefit of these single-layer, all-metal metasurfaces is their simplicity, and their optical performance can be tuned by changing the dimensions of the structures. Søndergaard et al.[15] proposed an all-metal broadband absorber based on adiabatic focusing of gap surface plasmons in ultra-sharp, V-shaped grooves. The groove depth, width, and inclination angle were observed to influence the absorption behavior. Crossed groove structures milled into thick gold achieved an average absorption of 96% in the visible range. A few years later, the study was repeated for nickel (about 95% absorption) and palladium (about 97%).[16] Similarly tall and tapered circular grooves were explored by Mo et al.[17] to realize more than 93% polarization-independent optical absorption. However, the experimentally fabricated coaxial hole arrays fell slightly short of the predicted values. Both groups noted that although a very accurate fabrication method, focused ion beam milling was notably time-consuming. This limits the feasible size of the absorbers. Recently, Ng et al.[18] have presented a scalable fabrication process in which gap plasmon-based absorbers were made

Received: October 4, 2018
Accepted: November 13, 2018
Published: November 13, 2018

DOI: 10.1021/acsami.8b17294
ACS Appl. Mater. Interfaces 2018, 10, 42941−42947

using a sacrificial porous alumina template (AAO). Absorption of more than 92% of incident light in the 300−600 nm spectral range was obtained. Recent theoretical studies have proposed all-metal Au absorbers consisting of ordered nanotriangle arrays[19] and concentric nanoring arrays,[20] which could be realized using standard lithography techniques.

Successful use of new absorbers in commercial products requires the fabrication to be simple, fast, low-cost, and easily integratable into existing processes. However, as the subwavelength patterns become smaller and more complex, fabrication also becomes more complicated and expensive. Another prominent issue with many nanostructured absorbers today is their sensitivity to the polarization and/or angle of incidence of the incoming light. Thus, for practical applications, the optical absorber should be easy to fabricate over large areas, and absorption should be omnidirectional, broadband, and polarization-independent. Combining these four criteria seems to still pose a challenge.

We present a strategy for designing and creating an all-metal broadband, wide-angle, polarization-independent optical absorber using the self-assembly of block copolymers (BCPs). Block copolymers (BCPs) are long chain molecules that organize into highly uniform, periodic patterns due to microphase separation. The pattern morphology is determined by the volume fraction of the block segments, whereas the size and periodicity of the patterns are dictated by the molecular weight.[21] BCP lithography enables the fabrication of extremely dense patterns and small features ranging from several tens of nanometers to even sub-5 nm dimensions.[22] The BCP patterns can be used either as masks for etching[23−25] or as scaffolds for nanostructure formation.[26−29] This bottom-up patterning strategy combined with template-stripping of Au enabled us to fabricate large-area Au nanodome arrays, where the optical properties could be controlled via the size of the domes. We achieved broadband wide-angle absorption of visible light with subwavelength structures that are only a fraction of the size typically needed in single-material absorbers. In addition, the metasurface can be transferred onto any rigid or flexible substrate.

RESULTS AND DISCUSSION

Fabrication of Monolithic Metasurfaces. Figure 1a illustrates the main fabrication steps of the metasurface absorber, which consists of periodic gold nanodomes on top of a gold thin film. First, a high-molecular-weight block copolymer was used to form a hexagonal dot pattern, which was then transferred onto Si using SF_6/O_2 reactive-ion etching. The isotropic etch caused the BCP mask holes to widen progressively, resulting in conically shaped cavities etched into silicon, as seen in Figure 1b. A longer etch produced deeper and wider cavities, making the gap between neighboring structures smaller, as shown previously.[30] When a BCP mask with a pattern periodicity L_0 of 74 nm was used, the base diameter D could be varied from approximately 30 nm up to 60 nm. If larger than that, the etched cavities began to merge with one another.

In the next step, the cavities and the surface were covered with a uniform layer of Au, and a glass support was attached on top with UV-curing epoxy. Due to the poor adhesion of Au on Si, the metal film could be peeled off from the Si template, revealing a patterned Au surface (Figure 1c). Template-stripping has typically been used to produce ultra-smooth metal films but, more recently, has also been used to fabricate high-quality, low-loss plasmonic nanostructures.[31,32] Should the epoxy adhesive cause issues, template-stripped films can be adhered onto substrates using temperature-assisted bonding[33,34] or be made into free-standing films via electrodeposition.[31] We also demonstrated the peeling off of the patterned metal films using flexible substrates, as shown in Figure 1d.

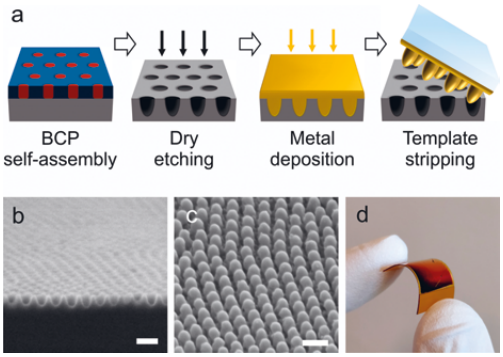

Figure 1. (a) Schematic showing the main fabrication steps of the plasmonic metasurfaces. (b) Side-view scanning electron microscopy (SEM) image of the BCP pattern etched into silicon. (c) SEM image of the final template-stripped Au thin film with nanodome-like structures. Scale bars 100 nm. (d) The patterned Au thin films displayed different colors depending on the nanostructure size. Au thin films could also be transferred onto flexible substrates.

The side-view scanning electron microscopy (SEM) images in Figure 2a reveal the morphology of the template-stripped metals. The smallest nanostructures resemble half-spheres (D = 35 ± 2.2 nm, height about 44 nm), whereas the largest structures begin to form a miniature moth-eye-like surface (D = 53 ± 3.3 nm, h about 67 nm and D = 58 ± 4.2 nm, h about 81 nm). The Si templates can be reused multiple times to produce identical patternings. Nagpal et al. reported making more than 30 replicas from the same template without any damage.[31] Another advantage of template-stripping is that the whole patterned metal film is monolithic, and there are no interfacial boundaries between the nanostructures and the underlying gold film. Noble metal structures fabricated with top-down lithography often require a thin interfacial layer of titanium or chromium to improve the adhesion of the structures to the substrate. For plasmonic structures, the adhesion layer can cause significant interface plasmon damping.[35]

Optical Characterization. The specular reflectance and diffuse reflectance (R) from the Au metasurfaces were measured with UV−vis spectroscopy. The comparison of the reflectance data confirmed that there was negligible diffuse reflectance from the metallic nanodomes. Therefore, light is absorbed and not scattered. This result was expected due to the small size of the nanostructures (h < 80 nm). Light transmittance (T) was also negligible due to the optically thick Au underlayer. The absorption (A) of the surfaces was determined as $A = 100\% - R_{specular} - T$ (with $T = 0$). The measured absorption at normal incidence of three metasurfaces with increasing nanodome size (diameter D = 35, 53, and 58 nm) is plotted in Figure 2c. A planar template-stripped film with no nanodomes produced a spectrum comparable to bulk

DOI: 10.1021/acsami.8b17294
ACS Appl. Mater. Interfaces 2018, 10, 42941−42947

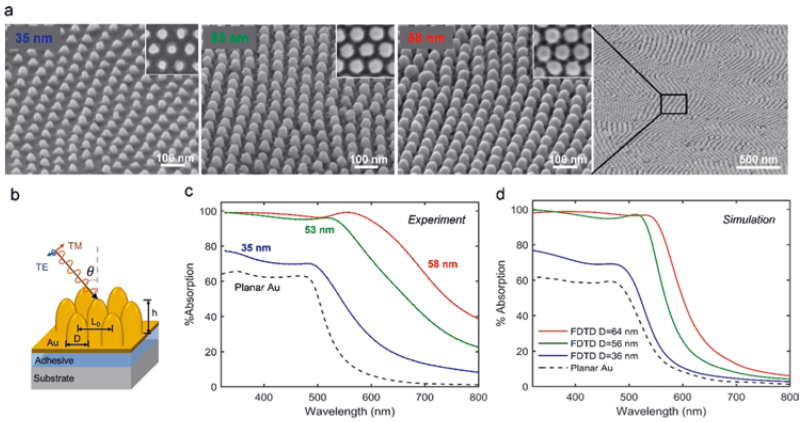

Figure 2. (a) Tilted-view SEM images of Au nanodome films produced via gold-stripping from patterned templates. The increase in the dome diameter from 35 to 58 nm is visible in the top-view insets. The far-right image illustrates the large-area assembly and grain structure of the patterns. (b) Schematic of the absorber structure and ultraviolet−visible (UV−vis) reflectance measurement. (c) Measured and (d) calculated absorption spectra of the nanodome films at normal incidence.

Au. Bulk Au is highly reflective above the 500 nm wavelength, whereas below 500 nm, the absorption is increased due to the Au interband transitions.[36] This causes the yellow color of gold. The introduction of nanodomes onto the Au surface modified the optical behavior. A progressive increase in visible light absorption was observed as the nanodome size increased. Broadband absorption close to unity was particularly evident with the large nanodomes. To demonstrate the versatility of the fabrication method, the same template-stripping technique was applied to fabricate nanodome thin films from silver. Bulk silver is an almost perfect reflector. The Ag nanodome thin films exhibited significantly improved absorption behavior with a peak absorption of 87% close to the plasmon resonance wavelength (see Supporting Information Figure S1).

The promisingly high absorption of the largest moth-eye-like nanodomes prompted us to investigate their sensitivity to light polarization and oblique illumination. The optical performance of the Au absorber was studied at different oblique incident angles under transverse magnetic (TM) and transverse electric (TE) polarized light. For TE polarized light, the electric field aligns perpendicular to the plane of incidence, whereas for TM light, the electric field aligns parallel, as depicted in Figure 2b. The symmetric configuration of the nanostructures was assumed to result in the same optical response for both polarizations. The measured reflectance spectra are plotted in Figure 3a. As expected, near the normal incidence ($\theta = 8°$), the nanostructured surface was insensitive to the polarization. As the incidence angle became larger than 25°, the reflectance for the TE polarization began to increase. A similar effect was observed with planar Au films.

For devices that harvest solar energy, omnidirectional or wide-angle absorption is a desired feature that ensures light is efficiently collected. Figure 3b displays the effects of the light incidence angle on the optical absorption characteristics of large nanodomes. Near-perfect absorption persists for a large range of incidence angles. At 55° incidence, the average absorption is still more than 90% in the 320−650 nm wavelength range. For normal incidence, the average absorption in this range is 97% with a peak absorption of

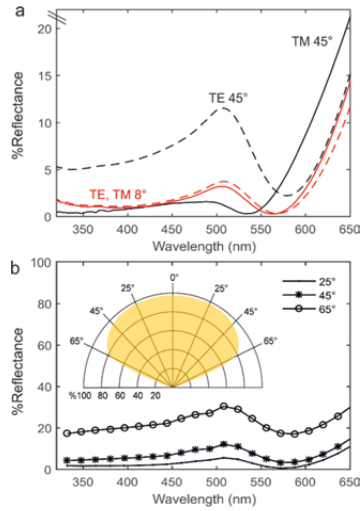

Figure 3. (a) Reflectance of Au metasurfaces with large nanodomes (D = 58 nm, h about 81 nm) measured using TE and TM polarized light to investigate polarization dependence for direct (red) and oblique incidence (45°, black). (b) Au thin film light reflectance at 25, 45, and 65° angles of incidence. The inset displays the average absorption of the film in the 320−650 nm range.

99%, which is a remarkable result considering the simplicity and small size of these Au absorber structures. To the best of our knowledge, this is one of the highest visible light absorption values achieved in plasmonic single-material absorbers thus far. Søndergaard et al.[15] achieved a similar average absorption of 96% in the 450−850 nm range using Au arrays of crossing convex grooves. The surface of the groove arrays resembled square-packed nanodomes. However, the size of the domes was approximately 5 times larger than in the

DOI: 10.1021/acsami.8b17294
ACS Appl. Mater. Interfaces 2018, 10, 42941−42947

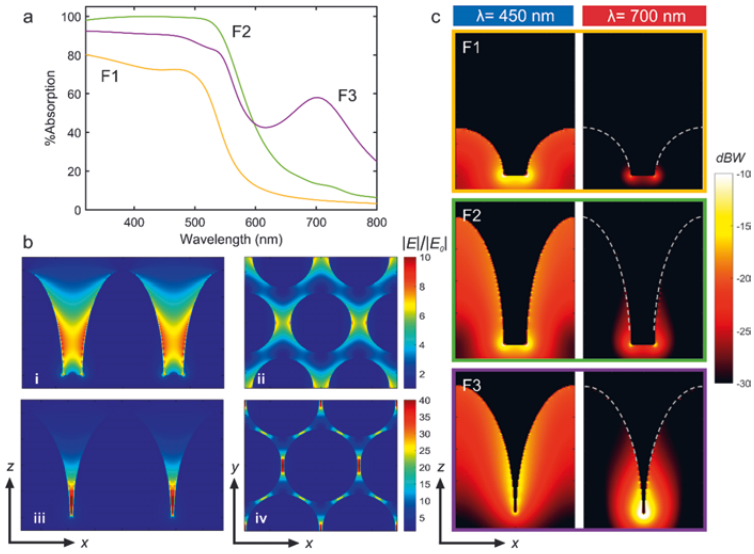

Figure 4. (a) Simulated absorption spectra of different nanodome geometries (F1) D = 60 nm, h = 30 nm, (F2) D = 60 nm, h = 80 nm and (F3) D = 73 nm, h = 80 nm. Periodicity in all structures is set to 75 nm. (b) Maximum enhancement of the near-field for nanodome geometries (F2) at 570 nm (i, ii) and (F3) at 700 nm (iii, iv). The horizontal crosscut (z = 10 nm) of the field distribution shows the emergence of a gap resonance as the gap width is decreased (iv). Notice the difference in scale between the top and bottom rows. (c) The cross-section colormaps describe the absorption in the structures (F1)−(F3) at short and long wavelengths. Brighter areas correspond to regions with higher absorption.

present absorber, and surface coverage was limited by the fabrication method.

Origin of Broadband Absorption. To understand the absorption behavior and to optimize the design of the absorber, numerical finite-difference time-domain (FDTD) simulations were performed. The patterned thin film was modeled as an infinite surface of perfectly arranged hemispheroids. The absorption spectra simulated using geometric parameters obtained from the SEM images were in excellent agreement with the experimental measurements at short wavelengths (Figure 2c,d). At longer wavelengths (λ > 600 nm), the experimentally measured absorption was greater than what was predicted. As seen in Figure 2a, the patterned films consist of large grains in which the nanodomes are aligned in the same direction. The FDTD model cannot account for grains, grain boundaries, or possible plasmonic coupling over long chains of structures. Discrepancies may also arise from imperfections in the pattern, such as size variations, point defects, and surface roughness. The size variation is one likely explanation for the broadened absorption spectra, and it will be discussed in more detail later.

The FDTD simulations support the experimental findings that the optical response can be tuned by altering the geometry of the nanostructures. The simulated structures with decreasing periodicity or an increasing dome diameter produced almost identical absorption spectra, as seen in Supporting Information Figure S2. Therefore, the optical behavior of the nanodome absorbers was deduced not to depend on the structure periodicity or dome diameter but mainly on the sharp gap region between the particles. It was discovered that an increase in dome height or a decrease in the width of the gap resulted in enhanced absorption. Simulations verified the experimentally observed phenomenon that absorption in the visible range was maximized when the gap width was 15−25 nm and the dome height was 70−80 nm (Supporting Information Figure S3a). Further increase in the dome height resulted in deteriorating absorption at short wavelengths but a slight improvement at longer wavelengths (λ > 600 nm). For extremely narrow gap widths (<5 nm), multiple absorption peaks appear at longer wavelengths, and absorption is enhanced as the dome height is increased (Supporting Information Figure S3b). Optical absorption in these types of ultranarrow, high aspect ratio gaps has been previously analyzed and demonstrated by Søndergaard et al.[15]

We suspected that tightly packed nanodomes could support gap plasmon modes inside the small gap cavities between the particles. Narrow gaps and sharp tips in subwavelength metal nanostructures are known to enhance the electric fields because the energy is confined in a small volume.[37] The gap effect was investigated via electric field simulations and absorption cross-section maps. The maximum field enhancements for two dome geometries at 570 and 700 nm are displayed in Figure 4b. A dipole-like field is induced between the particles following the polarization of the source. As the gap is made narrower, the field enhancement can also be observed symmetrically in the six gaps, although the enhancement is still strongest in the direction of the source polarization. Quantitatively, the enhancement factor of about 10−40 is modest compared to recent results obtained with optical nanoantennas.[38,39]

The two-dimensional absorption maps presented in Figure 4c display power damping in the nanostructures where 0 dB represents the absorption of all input power, −10 dB a 10× reduction in absorbed power, and so forth. The cross-section

DOI: 10.1021/acsami.8b17294
ACS Appl. Mater. Interfaces 2018, 10, 42941−42947

maps show that at short wavelengths (450 nm), power is absorbed throughout the particle but especially in the gap region between two particles. As the particle height increases or the gap decreases, the absorption becomes more localized on the particle surface and in the gap region. In the case of small particles or large gap widths, incoming light excites the dipole particle plasmon resonance that causes absorption. Larger particles cause stronger absorption of light. For gap widths of less than 5 nm, coupling between neighboring particles becomes evident, and multiple absorption peaks appear in the absorption spectra (Figure 4a and Supporting Information Figure S3b). The location of the peaks is highly sensitive to the gap size and the particle height. At the peak wavelength, the absorption of light is significantly enhanced in the gap region, supporting the theory of gap plasmons (Figure 4b, sample (F3)). These sub-80 nm nanodomes do not satisfy the criteria for adiabatic nanofocusing of propagating gap plasmon modes,[15] and thus, we interpret the absorption mechanism as related to localized resonances of nanoparticles and gaps.

CONCLUSIONS

We have demonstrated a simple, high-throughput method for fabricating large-area, ultrathin plasmonic absorbers using gold-stripping from BCP patterned silicon templates. The all-metal absorbers consisted of hexagonally packed, elongated nanodomes that gradually widened toward the bottom. Absorbers of about 1 and 4 cm^2 were demonstrated, but due to the scalability of BCP thin-film processing, nanodome absorbers could be realized on a wafer scale. Furthermore, the thin film could be transferred onto any rigid or flexible substrate making the thin film an excellent coating for devices that collect solar energy. As the dimensions, and especially the distance from the absorption point to the ambient, remain small, we expect structures like these to enable the extraction of hot carriers for energy, catalysis, or sensing-related applications. We have shown that an 80 nm tall Au nanodome pattern is capable of absorbing more than 97% of visible light at direct incidence and still more than 90% when illuminated at a high angle of incidence. Due to the structure symmetry, the all-metal absorber was also shown to be insensitive to the polarization of light. FDTD simulations support the findings that the absorption behavior could be tuned by changing the width of the gap between neighboring nanodomes. Experimentally, this could be done by varying the time the pattern template was plasma-etched. The simulations suggest that the enhanced absorption is related to localized surface plasmons on the nanodome surfaces and the formation and absorption of gap plasmons in the gaps between the nanostructures. Contrary to typical plasmonic black gold absorbers, the nanodome thin films appeared dark red due to the higher reflectivity around 700 nm wavelengths. It should be possible to extend the absorption band into the red and near infrared wavelengths by exciting multiple resonance modes via nanostructures with 10−20 nm variations in structure size and spacing.

MATERIALS AND METHODS

Sample Fabrication. Patterned templates were fabricated from native-oxide-covered Si(100) wafers using block copolymer lithography and dry etching. Asymmetric poly(styrene-vinyl-2-pyridine) (PS−P2VP) with a styrene fraction of 0.72 (M_n = 188 000 g/mol, PDI = 1.18) was purchased from Polymer Source Inc. and used as received. Toluene and anhydrous tetrahydrofuran (THF) were obtained from Sigma-Aldrich. PS−P2VP was dissolved in a 7:3 mixture of toluene and THF, stirred overnight, and filtered through a 0.2 μm syringe filter before use. The wafers were spin-coated with the BCP solution at 2000−3000 rpm to form thin films that were about 45 nm thick. A 2 min soft bake was performed at 125 °C to remove all residual solvent. To promote self-assembly and obtain vertically aligned cylinders, the BCP films were annealed in THF vapor in a custom-made controlled annealing system similar to the setup described by Lundy et al.[40]

The P2VP domains were selectively swelled by ethanol to open up cylindrical pores in the film.[41] Samples were immersed in ethanol for 5−15 min and carefully washed with deionized water. The porous BCP mask was then used to transfer the pattern into silicon with isotropic SF_6/O_2 reactive-ion etching at 160 W for 15−30 s, as described previously.[30] The isotropic etching process was utilized to progressively widen the patterns in the BCP mask and create tapered cone structures in Si. Finally, the BCP mask was removed with a brief 60 s oxygen plasma treatment.

Gold and silver films that were 50−200 nm thick were deposited on the cleaned Si templates in an Instrumentti Mattila Oy electron-beam evaporator. To minimize contamination by residual oxygen and water vapor, the chamber vacuum was pumped below 1.0×10^{-7} mbar. The depositions were performed at a rate of 1−2 Å/s for Au and 3 Å/s for Ag. After the deposition, a transparent top plate was attached to the metal surface with a UV-curing adhesive (Norland Optical Adhesive 61), and the plate and the patterned metal film were manually peeled off from the Si template. The Si templates can be reused multiple times.

Characterization. The surfaces of the Si templates and the template-stripped Au films were examined with scanning electron microscopy (Carl Zeiss ULTRA 55), and the resulting images were analyzed using ImageJ2[42] software. The SEM images were converted into binary black-and-white images with automatic thresholding, and a particle analysis tool was used to calculate the average diameter of the structures. The periodicity of the patterns was determined using fast Fourier transform analysis.

The optical properties were measured using a PerkinElmer Lambda 1050 UV−vis spectrophotometer with a universal reflectance accessory, a tungsten-halogen light source, and polarizing filters. Absolute specular reflectance (R) at normal and oblique incidence was recorded in a wavelength range of 320−880 nm using a beam spot size of 4×4 mm^2. The measurement configuration is self-referencing (the V−N method), and thus, no calibration standards were needed. Reflectance measurements were also performed with a 150 mm integrating sphere module at an incidence angle of 8° to determine the amount of light scattering. Absorption A was calculated as $A = 100\% - R - T$, where R is the total reflectance and T is the transmittance of the thin film.

Optical Modeling. The effect of the structure size on the optical properties was studied using three-dimensional FDTD modeling (FDTD Solutions, Lumerical). The structures were estimated to be elongated (prolate) hemispheroids in a hexagonal lattice on top of a planar metal film. The radius (short axis length), hemispheroid height (long axis), and periodicity were varied. To simulate an infinitely periodic array and to reduce the simulation space, symmetric and anti-symmetric boundary conditions were used on the unit cell sides. The material properties were defined by Johnson and Christy optical constants for Au.[43] The simulated unit cell was excited by a plane wave as a short pulse covering a wavelength range of 250−900 nm and propagating along the z-axis. Two power monitors were set to detect the total reflectance and the transmittance. Electric field distributions were also recorded at various horizontal and vertical cross-sectional planes. Absorption in the material per unit volume was calculated from the divergence of the Poynting vector and was automatically performed in the simulation program. The acquired value was normalized with the incident power density over the unit cell. The mesh grid was 0.5 nm around the gold nanostructures.

DOI: 10.1021/acsami.8b17294
ACS Appl. Mater. Interfaces 2018, 10, 42941−42947

■ ASSOCIATED CONTENT

Supporting Information

The Supporting Information is available free of charge on the ACS Publications website at DOI: 10.1021/acsami.8b17294.

Measured absorption spectra of template-stripped silver thin films; simulated absorption spectra of Au nanodomes with varying height, diameter, and periodicity (PDF)

■ AUTHOR INFORMATION

Corresponding Author

*E-mail: hanna.hulkkonen@tut.fi.

ORCID

Hanna Hulkkonen: 0000-0003-1206-3060

Notes

The authors declare no competing financial interest.

■ ACKNOWLEDGMENTS

Financial support for this work was provided by Tampere University of Technology, TUT, Grant number 83026.

■ REFERENCES

(1) Vorobyev, A. Y.; Guo, C. Enhanced Absorptance of Gold Following Multipulse Femtosecond Laser Ablation. *Phys. Rev. B* **2005**, *72*, No. 195422.

(2) Yang, Y.; Yang, J.; Liang, C.; Wang, H. Ultra-Broadband Enhanced Absorption of Metal Surfaces Structured by Femtosecond Laser Pulses. *Opt. Express* **2008**, *16*, 11259−11265.

(3) Kats, M. A.; Blanchard, R.; Genevet, P.; Capasso, F. Nanometre Optical Coatings Based on Strong Interference Effects in Highly Absorbing Media. *Nat. Mater.* **2013**, *12*, 20−24.

(4) Vitrey, A.; Alvarez, R.; Palmero, A.; González, M. U.; García-Martín, J. M. Fabrication of Black-Gold Coatings by Glancing Angle Deposition with Sputtering. *Beilstein J. Nanotechnol.* **2017**, *8*, 434−439.

(5) Christiansen, A. B.; Caringal, G. P.; Clausen, J. S.; Grajower, M.; Taha, H.; Levy, U.; Asger Mortensen, N.; Kristensen, A. Black Metal Thin Films by Deposition on Dielectric Antireflective Moth-Eye Nanostructures. *Sci. Rep.* **2015**, *5*, No. 10563.

(6) Liu, N.; Mesch, M.; Weiss, T.; Hentschel, M.; Giessen, H. Infrared Perfect Absorber and Its Application as Plasmonic Sensor. *Nano Lett.* **2010**, *10*, 2342−2348.

(7) Hao, J.; Wang, J.; Liu, X.; Padilla, W. J.; Zhou, L.; Qiu, M. High Performance Optical Absorber Based on a Plasmonic Metamaterial. *Appl. Phys. Lett.* **2010**, *96*, No. 251104.

(8) Hägglund, C.; Zeltzer, G.; Ruiz, R.; Thomann, I.; Lee, H.; Brongersma, M. L.; Bent, S. F. Self-Assembly Based Plasmonic Arrays Tuned by Atomic Layer Deposition for Extreme Visible Light Absorption. *Nano Lett.* **2013**, *13*, 3352−3357.

(9) Tittl, A.; Mai, P.; Taubert, R.; Dregely, D.; Liu, N.; Giessen, H. Palladium-Based Plasmonic Perfect Absorber in the Visible Wavelength Range and Its Application to Hydrogen Sensing. *Nano Lett.* **2011**, *11*, 4366−4369.

(10) Liu, Z.; Liu, X.; Huang, S.; Pan, P.; Chen, J.; Liu, G.; Gu, G. Automatically Acquired Broadband Plasmonic-Metamaterial Black Absorber during the Metallic Film-Formation. *ACS Appl. Mater. Interfaces* **2015**, *7*, 4962−4968.

(11) Aydin, K.; Ferry, V. E.; Briggs, R. M.; Atwater, H. Broadband Polarization-Independent Resonant Light Absorption Using Ultrathin Plasmonic Super Absorbers. *Nat. Commun.* **2011**, *2*, No. 517.

(12) Hedayati, M. K.; Javaherirahim, M.; Mozooni, B.; Abdelaziz, R.; Tavassolizadeh, A.; Chakravadhanula, V. S. K.; Zaporojtchenko, V.; Strunkus, T.; Faupel, F.; Elbahri, M. Design of a Perfect Black Absorber at Visible Frequencies Using Plasmonic Metamaterials. *Adv. Mater.* **2011**, *23*, 5410−5414.

(13) Walter, R.; Tittl, A.; Berrier, A.; Sterl, F.; Weiss, T.; Giessen, H. Large-Area Low-Cost Tunable Plasmonic Perfect Absorber in the Near Infrared by Colloidal Etching Lithography. *Adv. Opt. Mater.* **2015**, *3*, 398−403.

(14) Hu, C.; Liu, L.; Zhao, Z.; Chen, X.; Luo, X. Mixed Plasmons Coupling for Expanding the Bandwidth of Near-Perfect Absorption at Visible Frequencies. *Opt. Express* **2009**, *17*, 16745−16749.

(15) Søndergaard, T.; Novikov, S. M.; Holmgaard, T.; Eriksen, R. L.; Beermann, J.; Han, Z.; Pedersen, K.; Bozhevolnyi, S. I. Plasmonic Black Gold by Adiabatic Nanofocusing and Absorption of Light in Ultra-Sharp Convex Grooves. *Nat. Commun.* **2012**, *3*, No. 969.

(16) Beermann, J.; Eriksen, R. L.; Holmgaard, T.; Pedersen, K.; Bozhevolnyi, S. I. Plasmonic Black Metals via Radiation Absorption by Two-Dimensional Arrays of Ultra-Sharp Convex Grooves. *Sci. Rep.* **2014**, *4*, No. 6904.

(17) Mo, L.; Yang, L.; Nadzeyka, A.; Bauerdick, S.; He, S. Enhanced Broadband Absorption in Gold by Plasmonic Tapered Coaxial Holes. *Opt. Express* **2014**, *22*, 32233−32244.

(18) Ng, C.; Yap, L. W.; Roberts, A.; Cheng, W.; Gómez, D. E. Black Gold: Broadband, High Absorption of Visible Light for Photochemical Systems. *Adv. Funct. Mater.* **2017**, *27*, No. 1604080.

(19) Gong, J.; Yang, F.; Zhang, X. A Novel Wideband Optical Absorber Based on All-Metal 2D Gradient Nanostructures. *J. Phys. D: Appl. Phys.* **2017**, *50*, No. 455105.

(20) Fu, G.; Liu, X.; Huang, Z.; Chen, J.; Liu, Z. Metallic Metasurfaces for Light Absorbers. *IEEE Photonics Technol. Lett.* **2017**, *29*, 47−50.

(21) Bates, F. S.; Fredrickson, G. H. Block Copolymer Thermodynamics: Theory and Experiment. *Annu. Rev. Phys. Chem.* **1990**, *41*, 525−557.

(22) Kennemur, J. G.; Yao, L.; Bates, F. S.; Hillmyer, M. A. Sub-5 Nm Domains in Ordered Poly(Cyclohexylethylene)- Block -Poly-(Methyl Methacrylate) Block Polymers for Lithography. *Macromolecules* **2014**, *47*, 1411−1418.

(23) Gu, X.; Liu, Z.; Gunkel, I.; Chourou, S. T.; Hong, S. W.; Olynick, D. L.; Russell, T. P. High Aspect Ratio Sub-15 Nm Silicon Trenches from Block Copolymer Templates. *Adv. Mater.* **2012**, *24*, 5688−5694.

(24) Hirai, T.; Leolukman, M.; Liu, C. C.; Han, E.; Kim, Y. J.; Ishida, Y.; Hayakawa, T.; Kakimoto, M. A.; Nealey, P. F.; Gopalan, P. One-Step Direct-Patterning Template Utilizing Self-Assembly of POSS-Containing Block Copolymers. *Adv. Mater.* **2009**, *21*, 4334−4338.

(25) Jung, Y. S.; Lee, J. H.; Lee, J. Y.; Ross, C. A. Fabrication of Diverse Metallic Nanowire Arrays Based on Block Copolymer Self-Assembly. *Nano Lett.* **2010**, *10*, 3722−3726.

(26) Shin, K.; Leach, K. A.; Goldbach, J. T.; Kim, D. H.; Jho, J. Y.; Tuominen, M.; Hawker, C. J.; Russell, T. P. A Simple Route to Metal Nanodots and Nanoporous Metal Films. *Nano Lett.* **2002**, *2*, 933−936.

(27) Chai, J.; Buriak, J. M. Using Cylindrical Domains of Block Copolymers to Self-Assemble and Align Metallic Nanowires. *ACS Nano* **2008**, *2*, 489−501.

(28) Peng, Q.; Tseng, Y. C.; Darling, S. B.; Elam, J. W. Nanoscopic Patterned Materials with Tunable Dimensions via Atomic Layer Deposition on Block Copolymers. *Adv. Mater.* **2010**, *22*, 5129−5133.

(29) Tseng, Y.-C.; Peng, Q.; Ocola, L. E.; Elam, J. W.; Darling, S. B. Enhanced Block Copolymer Lithography Using Sequential Infiltration Synthesis. *J. Phys. Chem. C* **2011**, *115*, 17725−17729.

(30) Hulkkonen, H. H.; Salminen, T.; Niemi, T. Block Copolymer Patterning for Creating Porous Silicon Thin Films with Tunable Refractive Indices. *ACS Appl. Mater. Interfaces* **2017**, *9*, 31260−31265.

(31) Nagpal, P.; Lindquist, N. C.; Oh, S.-H.; Norris, D. J. Ultrasmooth Patterned Metals for Plasmonics and Metamaterials. *Science* **2009**, *325*, 594−597.

(32) Yoo, D.; Johnson, T. W.; Cherukulappurath, S.; Norris, D. J.; Oh, S.-H. Template-Stripped Tunable Plasmonic Devices on Stretchable and Rollable Substrates. *ACS Nano* **2015**, *9*, 10647−10654.

(33) Lee, K.-L.; Chen, P.-W.; Wu, S.-H.; Huang, J.-B.; Yang, S.-Y.; Wei, P.-K. Enhancing Surface Plasmon Detection Using Template-Stripped Gold Nanoslit Arrays on Plastic Films. *ACS Nano* **2012**, *6*, 2931−2939.
(34) Mosley, D. W.; Chow, B. Y.; Jacobson, J. M. Solid-State Bonding Technique for Template-Stripped Ultraflat Gold Substrates. *Langmuir* **2006**, *22*, 2437−2440.
(35) Habteyes, T. G.; Dhuey, S.; Wood, E.; Gargas, D.; Cabrini, S.; Schuck, P. J.; Alivisatos, A. P.; Leone, S. R. Metallic Adhesion Layer Induced Plasmon Damping and Molecular Linker as a Nondamping Alternative. *ACS Nano* **2012**, *6*, 5702−5709.
(36) Thèye, M.-L. Investigation of the Optical Properties of Au by Means of Thin Semitransparent Films. *Phys. Rev. B* **1970**, *2*, 3060−3078.
(37) Sundaramurthy, A.; Crozier, K. B.; Kino, G. S.; Fromm, D. P.; Schuck, P. J.; Moerner, W. E. Field Enhancement and Gap-Dependent Resonance in a System of Two Opposing Tip-to-Tip Au Nanotriangles. *Phys. Rev. B* **2005**, *72*, No. 165409.
(38) Zhu, Z.; Bai, B.; You, O.; Li, Q.; Fan, S. Fano Resonance Boosted Cascaded Optical Field Enhancement in a Plasmonic Nanoparticle-in-Cavity Nanoantenna Array and Its SERS Application. *Light Sci. Appl.* **2015**, *4*, e296.
(39) Pellegrini, G.; Celebrano, M.; Finazzi, M.; Biagioni, P. Local Field Enhancement: Comparing Self-Similar and Dimer Nanoantennas. *J. Phys. Chem. C* **2016**, *120*, 26021−26024.
(40) Lundy, R.; Flynn, S. P.; Cummins, C.; Kelleher, S. M.; Collins, M. N.; Dalton, E.; Daniels, S.; Morris, M. A.; Enright, R. Controlled Solvent Vapor Annealing of a High: χ Block Copolymer Thin Film. *Phys. Chem. Chem. Phys.* **2017**, *19*, 2805−2815.
(41) Park, S.; Wang, J.-Y.; Kim, B.; Xu, J.; Russell, T. P. A Simple Route to Highly Oriented and Ordered Nanoporous Block Copolymer Templates. *ACS Nano* **2008**, *2*, 766−772.
(42) Rueden, C. T.; Schindelin, J.; Hiner, M. C.; DeZonia, B. E.; Walter, A. E.; Arena, E. T.; Eliceiri, K. W. ImageJ2: ImageJ for the next Generation of Scientific Image Data. *BMC Bioinf.* **2017**, *18*, 529.
(43) Johnson, P. B.; Christy, R. W. Optical Constants of the Noble Metals. *Phys. Rev. B* **1972**, *6*, 4370−4379.

DOI: 10.1021/acsami.8b17294
ACS Appl. Mater. Interfaces 2018, 10, 42941−42947

PUBLICATION III

Automated solvent vapor annealing with nanometer scale control of film swelling for block copolymer thin films

H. Hulkkonen, T. Salminen and T. Niemi

Soft Matter, vol. 15, no. 39, (2019), 7909–7917
DOI: 10.1039/c9sm01322a

Soft Matter

PAPER

View Article Online
View Journal | View Issue

Cite this: *Soft Matter*, 2019, **15**, 7909

Automated solvent vapor annealing with nanometer scale control of film swelling for block copolymer thin films†

Hanna Hulkkonen, *[a] Turkka Salminen [b] and Tapio Niemi *[a]

Received 2nd July 2019,
Accepted 13th September 2019

DOI: 10.1039/c9sm01322a

rsc.li/soft-matter-journal

Molecular self-assembly of block copolymers has been pursued as a next generation high-resolution, low-cost lithography technique. Solvent vapor annealing is a promising way of achieving self-assembled patterns from polymers with high interaction parameters, χ, or high molecular weights. Compared to thermal annealing, the assembly in a solvated state can be much faster, but the film swelling process is typically challenging to control and reproduce. We report the design and implementation of an automated solvent annealing system that addresses these issues. In this system the film swelling is controlled *via* local heating or cooling, which enables exceptionally fast and precise modulation of the swelling. The swelling of the polymer films follows preprogrammed annealing profiles with the help of a feedback loop that compares and tunes the film thickness with respect to the set point. The system therefore enables complex annealing profiles such as rapid cyclic swelling and deswelling. We show that the orientation of the pattern morphology and the amount of lattice defects are influenced by the used annealing profile. We demonstrate that optimized profiles significantly shorten the annealing time (<15 min) of high-χ and high-molecular weight poly(styrene-*b*-2-vinylpyridine).

Introduction

Fabrication of nanostructures is becoming steadily more important as nanotechnology is being adopted into all types of manufacturing processes. Many devices and systems used in the modern society are becoming progressively smaller and taking advantage of components with nanoscale dimensions in order to be more efficient. For quite some time, top-down photolithography has been the cornerstone of nanofabrication but in some fields, it is now reaching its limitations. The emergence of sophisticated bottom-up methods is offering new possibilities to let the 2D and 3D nanomaterials and nanodevices build themselves using self-assembling processes. One promising strategy is block copolymer (BCP) self-assembly where chemically dissimilar polymer molecules are driven to phase-separate into periodic, three-dimensional nanostructures.[1–4] The size of the structures can be scaled up or down by tuning the molecular weight and the chemical dissimilarity, known as the Flory–Huggins parameter χ, of the BCPs. Currently BCP patterns in the 5 to 200 nm size range can be produced.[5,6] However, the pattern dimensions are only truly limited by the present-day polymer synthesis methods and self-assembly kinetics. Theoretically, patterns with domains as small as 1 nm or larger than 300 nm could be made using ultra-low or ultra-high molecular weight BCPs.[7–9] Considerable effort has been put into directing the self-assembly (DSA) of low molecular weight BCPs into sub-10 nm sized structures for semiconductor industry applications including high-density memory devices,[10,11] integrated circuit layouts,[12,13] and most recently, Fin field-effect transistors (FinFETs).[14] High molecular weight BCPs have found their uses in applications where dense patterning and large-area coverage is needed such as in filtration membranes,[15] antireflective coatings,[16,17] and optical metamaterials.[18,19]

For application purposes, the main challenges of BCP-based nanofabrication have been related to self-assembly; control of the pattern features and minimization of defects.[20] Chemically or topographically pre-patterned substrates are often used to control the orientation and the long-range lateral alignment of the BCP patterns.[21–24] The self-assembly of BCPs also requires annealing to enhance polymer mobility and facilitate the phase separation. In thermal annealing the BCP films are heated above the glass transition temperature (T_g) for increased mobility.[25,26] Another alternative is solvent vapor annealing (SVA) where the solvent vapor swells and plasticizes the BCP, reducing the T_g below the room temperature, screening unfavorable interactions and reducing the time needed for self-assembly.[27] Inherently SVA is very simple and can be done in a sealed chamber that contains a solvent reservoir and the sample.[28,29]

[a] *Nanophotonics, Faculty of Engineering and Natural Sciences, Tampere University, 33101 Tampere, Finland. E-mail: hanna.hulkkonen@tuni.fi, tapio.niemi@tuni.fi*
[b] *Tampere Microscopy Center, Tampere University, 33101 Tampere, Finland*

† Electronic supplementary information (ESI) available. See DOI: 10.1039/c9sm01322a

Non-equilibrium BCP morphologies can be obtained using selective or mixed solvents.[3,30,31] Solvothermal annealing processes have also been explored, and in this method both the solvent and the sample are heated to shorten the required annealing time.[32–34] SVA is particularly interesting for assembling BCPs that display slow self-assembly dynamics due to high molecular weight[6] (high-MW) or high Flory–Huggins interaction parameters (high-χ).[35]

Despite the huge potential of SVA, it has previously not been attractive for the semiconductor technology industry due to the lack of reproducibility compared to thermal annealing. Even minor changes in the environment, such as fluctuations in the ambient humidity or temperature, can drastically change the outcome of SVA. It has then been identified *via* grazing-incidence small angle scattering (GISAXS) that the degree of swelling of the film is a critical factor that affects the BCP morphology. Order–order and order–disorder transitions (ODT) have been shown to occur at precise, polymer-specific swelling ratios.[30,36] The degree of swelling also affects the lateral ordering of the BCP patterns, with the best order obtained when the film solvent content is close to the order–disorder transition concentration.[37,38] Better control of the film swelling has been achieved using flow SVA systems where the solvent vapor is fed continuously into the chamber using a carrier gas flow. The film swelling is controlled by changing the partial vapor pressure inside the chamber by mixing multiple gas streams.[39–41] Typically, sample chambers have had to be minuscule to compensate for the tardiness of the control *via* gas-flow mixing. Initially, it can take up to 15 to 30 min for the chamber to reach a saturated atmosphere and for the film to reach a steady swollen state.[37,41,42] Further changes implemented *via* gas mixing can take up to 3 to 5 min to occur.[43] The total annealing time has been in the range of hours.

Several actively-controlled annealing systems with some degree of automation have been introduced during the past couple of years. Jin *et al.*[44] demonstrated control of film swelling *via* argon flow that was adjusted using a feedback loop. Lundy *et al.*[45] suggested feedback-controlled annealing to maintain a constant temperature differential between the solvent and the substrate to obtain supersaturation conditions. Since film swelling was not monitored, it is unclear how stable or accurate the method is. Nelson *et al.*[46,47] presented an alternative way of computer controlling the chamber pressure by adjusting the flow rates at both the inlet and outlet valves. Solvent could be quickly pushed into the film using increased chamber pressure, which was done by setting the inlet flow higher than the flow at the outlet. Feedback control was not yet implemented, but extremely constant swollen film thickness could be maintained *via* manual corrections.

It seemed necessary to develop a SVA system that is fast and precise and has the potential for wafer-scale processing. Furthermore, repeatability and applicability of solvent annealing could be improved by minimizing user- and environment-related variations. In this article, we report the design and implementation of an automated SVA device that can achieve high swelling ratios and fast swelling modulation by regulating the solvent vapor atmosphere near the wafer either by heating or cooling the local environment. The swelling of the polymer thin films is monitored and computer-controlled making it possible to use predetermined swelling profiles. The applicability of the SVA device is demonstrated using high-MW, high-χ poly(styrene-*b*-2-vinylpyridine) (PS–P2VP) thin films. The diffusivity of these high segregation strength polymers is typically low and the order–disorder transition limit high, leading to slow self-assembly kinetics and poor ordering.

Results and discussion

SVA system setup

We built an automated SVA system (Fig. 1) that allows for precision control of the annealing process with the fastest modulation of the film swelling that has been demonstrated so far. The setup consists of a custom-made annealing chamber with a cylindrical body ($\varnothing$ = 75 mm, $V \sim$ 100 ml) that can fit semiconductor wafers up to 2 inch in diameter. The copper stage inside the chamber can be heated or cooled using a thermoelectric cooler (TEC). Thermoelectric heating/cooling enables extremely fast and accurate temperature modulations. In our setup, the stage temperature range is from −10 °C to +70 °C and the mean absolute deviation from the temperature set point was measured to be ±0.005 °C. The temperature of the sample stage is monitored with a temperature transducer. The solvent vapor is generated in a bubbler system, where dry nitrogen carrier gas is bubbled through a temperature-stabilized solvent reservoir and fed into the chamber. Contrary to conventional flow annealing devices, the gas stream is not diluted using a secondary N_2 gas line. However, a pure N_2 stream can be directed into the chamber for purging.

The chamber lid is fully detachable and has a quartz window for optical monitoring. Spectroscopic reflectometry was used to monitor the swelling of the film *via* the change in film thickness. Spectral reflectance is measured every 30 ms over a 320–800 nm wavelength range. The thickness of the film is determined by continuously fitting the measured spectrum to a model of a single thin film on a substrate. The optical constants of a dry BCP thin film

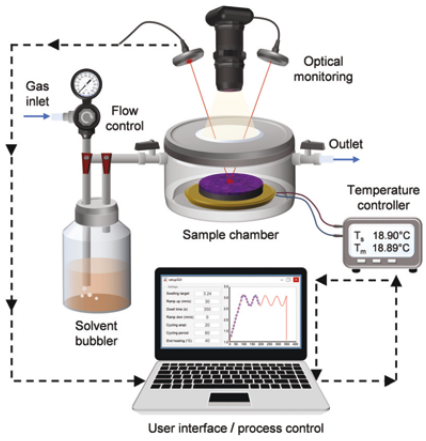

Fig. 1 Schematic of the automated solvent vapor flow annealing system.

were assumed to follow the dispersion relation of the majority-component polymer. The thickness prior to SVA was also measured using an ellipsometer. In the case of dry PS–P2VP thin films (~45 nm), the reflectometry and ellipsometry results differed from each other on average only by 1.1 nm proving that the chosen thin film model is valid. For swollen films, the spectral reflectance fitting worked best when the thin film was assumed to have a refractive index that changed with the addition of solvent. A video of the real-time thickness fitting during SVA can be found in the ESI† (Video SV1).

A CMOS camera with a long working distance objective operating in dark-field illumination provides live video of the thin film during annealing. The video feed can be used to monitor the quality of the films and quantify film dewetting. The largest area that can be viewed is ~1 cm × 1 cm. Thus, in case of small wafer pieces, the whole sample surface could be monitored. Similar video monitoring of film dewetting has been implemented by Jin *et al.*[44] with a more limited field of view. Other possible *in situ* characterization methods include epifluorescence microscopy, quartz crystal microbalances[42] and GISAXS.[30,36,37]

Control of film swelling

According to our understanding, the swelling of the thin films in our system is controlled by changing the relative saturation of the solvent vapor using temperature. It has been shown that higher relative saturation increases the swelling of polymer films.[41,48,49] The extent of the swelling depends on the solubility of the polymer in the solvent.[50] In our SVA system, the relative saturation can be increased in the vicinity of the sample by decreasing the stage temperature, which pushes more solvent into the BCP film. An increase in the temperature has the opposite effect. This type of swelling control mechanism is very fast and remarkably precise if the feedback loop and temperature response of the sample stage are fast enough.

The relative saturation P/P_{eq} is the ratio of the partial pressure of the solvent in the chamber to the equilibrium vapor pressure. As displayed in Fig. 2a, both pressures can be altered by changing the temperature. The equilibrium vapor pressure of a solvent is given by the semi-empirical Antoine equation:

$$P_{eq}\,[\mathrm{mmHg}] = 10^{A-B/(C+T)} \quad (1)$$

where T is the temperature in degrees Celsius. For the chosen annealing solvent tetrahydrofuran (THF) the Antoine parameters are A = 6.995, B = 1202.29 and C = 226.25.[51] In our qualitative model, which excludes the spatial variation of the atmosphere in the annealing chamber, the partial pressure of the annealing solvent is estimated using the ideal gas law $P = nRT/V$. Fig. 2a shows four different cases of THF partial pressures P(t1)–P(t4) that correspond to different amounts of THF in the chamber. The pressure P(t4) represents the partial pressure of THF, which is at saturation at room temperature (22 °C), and P(t1)–P(t3) are lower vapor concentrations. The temperature dependent relative saturation $P(t2)/P_{eq}$ is also displayed. The dew point is the temperature where the relative saturation reaches 100% and it is obviously sensitive to the vapor concentration of THF in the chamber.

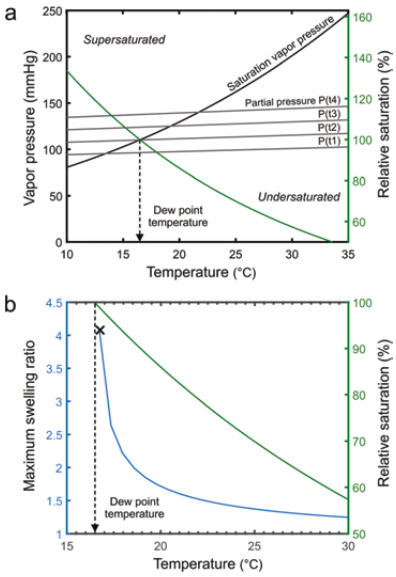

Fig. 2 (a) Temperature dependence of the saturation vapor pressure and the partial pressure of THF in the chamber. The four different P(t1)–P(t4) scenarios represent increasing filling of the chamber with THF vapor. The relative saturation $P(t2)/P_{eq}$ changes with the temperature. (b) The maximum calculated sorption of THF into a PS thin film increases with increasing relative saturation. Vapor begins to condense close to the dew point temperature ($P(t2)/P_{eq}$ = 100%) and the polymer dewets.

The swelling behavior of polymer thin films can be modelled as a dissolution process according to regular solution theory. At a relative saturation P/P_{eq}, the maximum equilibrium sorption of solvent into a homopolymer thin film can be described as:[50]

$$\ln\left(\frac{P}{P_{eq}}\right) = \ln\left(1-\frac{d_0}{d_{max}}\right) + \left(1-\frac{V_s}{V_p}\right)\frac{d_0}{d_{max}} + \chi\left(\frac{d_0}{d_{max}}\right)^2 \quad (2)$$

where d_0/d_{max} is the polymer volume fraction or alternatively the reciprocal of the maximum swelling ratio. The parameters V_s and V_p are the molar volumes of the solvent and polymer respectively. For simplicity's sake, the model calculations are done using values for polystyrene instead of those of PS-majority PS–P2VP. The Flory–Huggins parameter χ describes the interaction between the polymer and the solvent. In the evaluated temperature and concentration range it can be assumed constant, χ(PS–THF) = 0.414.[52]

The maximum equilibrium sorption of THF into a PS thin film is modelled in Fig. 2b. It can be observed that the swelling ratio becomes highly sensitive to the relative vapor saturation as the dew point temperature is approached. Close to the dew point, minute changes in the temperature ($T < \pm 0.5$ °C) are enough to drastically modulate the swelling ratio. Our SVA device with its temperature-controlled stage can operate in this region, a few tenths of a degree from the dew point, without issues

with solvent condensation. The tuning of the P/P_{eq} is effective primarily in the vicinity of the sample and stage surface (ESI,† Fig. S1 shows a measurement for water vapor). Since the solvent vapor is not close to the dew point elsewhere in the chamber, the chamber walls, lid and gas pipes do not need to be heated to prevent unwanted condensation. However, should the stage temperature decrease below the dew point, solvent vapor will condense on the stage and thin film swelling will become uncontrollable.

Automated annealing

One of our aims was to improve the reliability of SVA, which is essential for an industrially viable lithography technique. Therefore, a MATLAB based script was written to handle the annealing process from data collection to signal processing, computation and instrument control. The Instrument Controller Toolbox of MATLAB was set to communicate with the spectrometer, TEC module and the CMOS camera. A user-friendly graphical interface was built on top where the user could design the annealing run and set the relevant parameters. During the annealing run the thickness of the BCP thin film follows a predetermined swelling profile. The swelling of the thin film is actively controlled *via* the temperature of the sample stage. The thickness of the swollen film is compared to the target set point and the temperature is adjusted accordingly *via* a PID (proportional-integral-derivative) control feedback mechanism. The feedback loop is capable of controlling the film swelling every 30 ms. Mean deviation from the thickness target set point is typically smaller than ±0.2 nm. The swelling ratio SR is calculated as the thickness of the swollen film d divided by the original film thickness d_0.

Fig. 3 displays the optically measured swelling of a high-molecular weight PS–P2VP thin film during feedback-controlled and uncontrolled SVA in THF, toluene and acetone. The uncontrolled SVA was performed by keeping the stage at a constant temperature (T = 20 °C) and using a constant vapor flow. The shape of the swelling curve is greatly affected by the set flow rate and the solubility of the BCP in the solvent. According to Hildebrand[53] solubility parameters, toluene (δ_{TOL} = 18.2 $MPa^{1/2}$) is considered a good solvent for the PS-majority PS–P2VP (δ_{PS} = 18.7 $MPa^{1/2}$) and thus the BCP swells more in toluene than in a less-suitable solvent such as acetone (δ_{ACE} = 20.3 $MPa^{1/2}$). Overall, the solvent uptake in uncontrolled SVA is quite slow and the maximum swelling ratio is relatively low. Room temperature fluctuations and seasonal changes are also known to influence the swelling curve when no feedback loop is implemented.[44] The feedback-controlled thin film swelling presented in Fig. 3 and Fig. S2, S3 (ESI†) follows a predetermined swelling profile. The profile consists of an unrestricted solvent uptake period (10–40 s), a linear up-ramping regime at a predetermined rate, a steady dwell regime and a deswelling or quenching regime. The deswelling of the thin film can be done at a controlled rate (nm min^{-1}). Solvent can also be removed instantly (quenching) to preserve the morphology obtained in the swollen state by purging the chamber with N_2. The removal of the residual solvent content can be enhanced by simultaneously heating up the sample stage to 40–50 °C. In this type of feedback-controlled SVA device, BCP thin films can be made to swell quickly and to the desired swelling ratio, irrespective of the type of solvent used. The swelling control method based on relative saturation is applicable to not only different solvents but also different polymers. The controlled swelling of PDMS-majority PS–PDMS is demonstrated in ESI,† Fig. S3. Similar to the PS–P2VP, the uncontrolled film swelling of PS–PDMS in toluene is moderate but with the feedback-control, high SR can be reached. The temperature-controlled feedback system also eliminates the unwanted swelling variations that would arise from seasonal changes or changes in the ambient temperature.

The fast, controlled modulation of the film swelling enables the use of complex annealing profiles. In our SVA device, the steady dwell regime can be replaced with controlled ramping or cycling regimes. Fig. 3(b) demonstrates two annealing profiles, where the film swelling ratio was modulated rapidly in 30 s and 60 s cycles. The cycle period can be as fast as 5 s in feedback-controlled operation and less than 1 s in an open-loop system that does not use the measured SR as a corrective input. Dynamical simulations have suggested that repeating swelling and deswelling cycles could improve the perpendicular orientation of BCP domains in thick BCP films.[54] To the best of our knowledge, this is the first time that fast cyclic solvent annealing has been experimentally realized.

Performance evaluation with high-molecular weight BCPs

The SVA process has notably been susceptible to even minor changes in the annealing conditions or the surrounding environment making reproducibility an issue. Predetermined swelling profiles make it possible to precisely repeat experiments and explore how different process parameters influence the self-organization

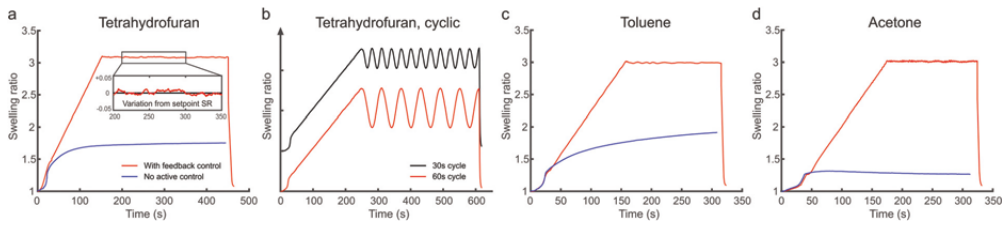

Fig. 3 Solvent annealing profiles of high-molecular weight PS–P2VP thin films annealed in (a) and (b) THF, (c) toluene and (d) acetone. The uncontrolled swelling of the BCP film in each solvent is displayed in blue while feedback-controlled swelling according to a predetermined high-SR swelling profile is in red or black. Inset in (a) displays the deviation of the measured SR from the set point. The possibility of cyclic annealing is shown in (b) with cyclic modulation of the SR in 30 s and 60 s periods. The cyclic profiles are vertically offset for clarity.

behavior of BCPs. The degree of swelling, SR, has been recognized *via* GISAXS studies to dictate order–order and order–disorder transitions in the BCP films, and influence the domain spacing and the degree of lateral ordering.[30,37] To verify the functionality of our annealing device we scrutinized the effect of the SR on the morphology of high-MW PS–P2VP thin films.

In the first experiment 45 nm thick PS–P2VP (M_n = 188 kg mol^{-1}) films were spin-coated on unmodified Si wafers from toluene–THF solutions. Fig. 4 displays scanning electron microscope (SEM) images of the platinum-stained BCP thin films after annealing with increasing swelling ratios using THF as a near-neutral annealing solvent. A ramp up rate of 0.6 SR per min was used and quenching was done immediately when target was reached with no dwell period. The micellar-like as-spun morphology was observed to improve with increasing swelling ratio until SR $\sim$ 3.5. A well-ordered hexagonally packed cylinder morphology with a domain spacing $L_0 \sim 75$ nm could be achieved in 4 minutes – or in little over 2 minutes if the ramp rate was increased to 1.0 SR per min.

With SR $>$ 3.6 the 188 kg mol^{-1} thin films exhibited a mixed morphology consisting of regions with perpendicular and parallel cylinders. The regions appeared to be single- and multi-layer areas that followed spinodal decomposition patterns. The appearance of these areas as well as possible dewetting could be observed during annealing from the camera images. Multilayering or terracing is known to occur due to commensurability issues between the film thickness and the equilibrium domain spacing L_0 of the BCP morphology.[55,56] Here terracing occurred when SR $\times$ d_0 $>$ $2L_0$. With higher SR, the film morphology consisted mainly of parallel cylinders that grew in length but with no significant lateral order. This morphology behavior is consistent with previous research on the effects of SR on low-molecular weight polystyrene–polylactide BCPs (18–75 kg mol^{-1}).[47]

The self-assembly of high-MW BCPs is typically hindered by the low mobility of long-chained polymers. As a result, it is challenging to achieve good lateral ordering of the BCP features, and solvent annealing of high-MW BCPs can take hours[6,15] or even days.[57] We tried annealing 258 kg mol^{-1} PS–P2VP thin films at a maximum feasible SR and then examined the growth of ordered cylinder grains in time. Fig. 5 and Fig. S4a (ESI†) illustrate the defect density of 258 kg mol^{-1} PS–P2VP thin films after 0 min, 10 min and 25 min of annealing dwell time. The blue regions depict locations where the lattice is not perfectly hexagonal, *i.e.* the PVP cylinders have fewer or more than six neighboring cylinders. The lattice defect density after up-ramping was 31.2 defects per μm^2, which deceased to 17.4 μm^{-2} after 10 min and finally to 15.6 μm^{-2} after 25 min of dwell time. This shows that grain coarsening and point defect annihilation is fastest during the first 10 minutes, after which the grain growth slows down. This is consistent with the grain size coarsening following a power-law $\xi \sim t^{\alpha}$ where α = 0.2–0.3 for thin films.[26,58] After 25 min of dwell time there are very few point defects left and most of the lattice imperfections arise from the grain boundaries. Elimination of these grain boundary defects would require significant reorientation of neighboring grains.

Previous research has shown that the highest degree of order and the largest grain sizes are achieved when solvent annealing is done close to the ODT limit.[36,38] Our swelling studies using high segregation strength BCPs were restricted more by the film commensurability than the ODT. SVA was done at an SR value that was just below the multilayering limit. A cautious estimate of the ODT concentration of 258 kg mol^{-1} PS–P2VP ($N \sim 2480$) would be $\phi_{PS-P2VP}$ = 0.136, corresponding to a SR of 7.33 (see ESI† for calculation). Thus, higher SR values could likely be used and larger grains achieved if the cylinder reorientation process was suppressed. This could be done using neutral brush layers or top coats that govern the preferred orientation of the BCP domains.[59–61] On unmodified substrates, the largest grain sizes that we achieved with the high-MW BCPs were in the range of several microns. Long-distance order and alignment can be achieved using substrates with topographic or chemical patterns that direct the self-assembly of the BCPs (DSA). We also tested the feedback-controlled SVA with these

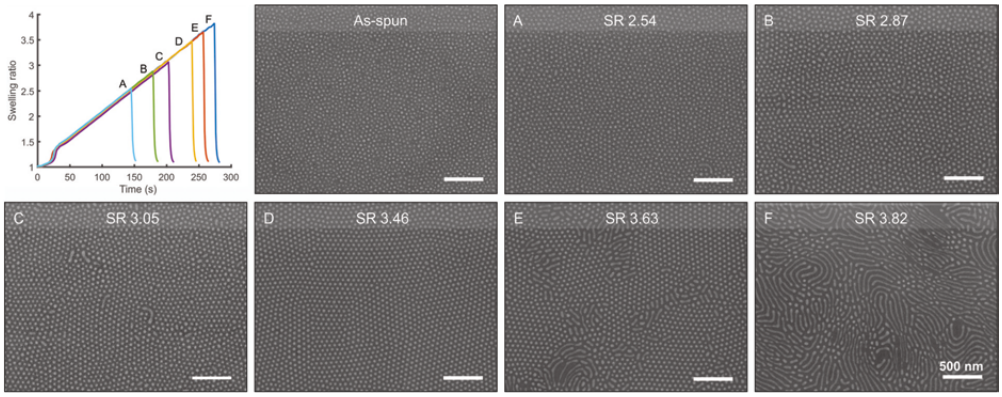

Fig. 4 Cylinder-forming PS–P2VP 188 kg mol^{-1} thin films annealed in THF at increasing swelling ratios. Films were quenched when target SR was reached to preserve the obtained BCP morphology. SEM images (A)–(F) of the platinum stained thin films display the change in BCP morphology with increasing SR values. Perpendicularly oriented and well-ordered cylinders were achieved around SR = 3.5 (D). Terracing occurred with SR $>$ 3.6 (E and F).

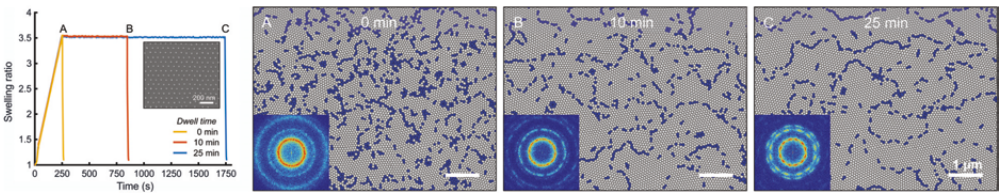

Fig. 5 Cylinder-forming PS–P2VP 258 kg mol^{-1} thin films annealed in THF at same swelling ratio but with increasing dwell times. (A)–(C) Defects in the BCP morphology after 0, 10 and 25 min of annealing dwell time. Perfectly ordered regions are mapped in gray. Defect locations where the hexagonal lattice is not six-fold coordinated are mapped in blue. Insets (A)–(C) show FFT of SEM images.

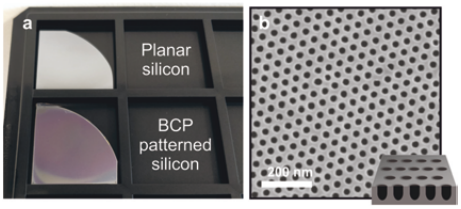

Fig. 6 (a) High-MW BCP self-assembly done on quarter-wafer scale using the automated SVA system. The BCP cylinder pattern is etched into Si causing the wafer color to change due to an effective refractive index change. (b) Top-down SEM image of the dry etched Si surface. The inset depicts the shallow pore structure that is obtained.

types of prepatterned substrates. The DSA of high-MW PS–P2VP on a Si trench pattern is demonstrated in Fig. S4b (ESI†), where highly aligned rows of perpendicular cylinders were achieved along the trench length.

The possibility of large area self-assembly was also explored since BCP lithography would be ideal for engineering materials with new surface properties. Subwavelength BCP patterns have been already used to produce nanostructured antireflective coatings[17] and anisotropic refractive index metamaterials.[19] So far, we have managed to optimize the whole BCP self-assembly and SVA process for quarter pieces of 2-inch Si wafers. Perpendicularly oriented BCP cylinders with a large grain size could be achieved over the quarter wafer by combining a high SR value ($3.0 < SR < 3.5$) with a 10–15 min annealing dwell time. Fig. 6a shows an unpatterned Si quarter wafer and a wafer where the 188 kg mol^{-1} PS–P2VP cylinder pattern has been etched into the Si surface. The shallow pores depicted in Fig. 6b modify the refractive index of the Si surface,[62] which can be seen as a uniform color change over the patterned area. A full analysis of the BCP morphology over a quarter wafer can be found in ESI,† Fig. S5.

Conclusions

Improvements in scalability and reliability are a key step in making BCP lithography commercially viable. Also better control, understanding and reproducibility of the solvent annealing process are needed. Since the solvent content in the thin films is an essential factor governing the final morphology and lateral order, more precise control of the swelling is required. In this paper, we describe the design and operation of an automated SVA system that is capable of modulating the film swelling with nanometer precision. The film swelling behavior is manipulated by changing the relative vapor saturation locally, near the surface of the sample. This control implementation uses local heating or cooling, which is a much faster method than the typical one using gas flow mixing. The advantage of feedback-controlled swelling is that the annealing process becomes insensitive to minor variations in the ambient conditions, gas flow rate and solvent vapor concentration.

With feedback-controlled SVA, different aspects of the film swelling profile can be isolated and their influence on the BCP self-assembly evaluated. For practical applications, the influence of SVA parameters on defect reduction, lateral ordering and self-assembly kinetics are of great interest. We demonstrated the utility of the SVA device by annealing high segregation strength polymers that typically display slow self-assembly kinetics due to low chain mobility. We have shown that 258 kg mol^{-1} PS–P2VP thin films can be made to self-organize into well-ordered cylinder patterns in under 15 minutes by optimizing the swelling profile. Complex swelling profiles are also possible, and we demonstrated controlled cyclic solvent annealing for the first time.

Experimental section

Thin film preparation

PS–P2VP cylinder-forming diblock copolymers were purchased from Polymer Source Inc. and used as received. The number average molecular weights of the BCPs were 258 kg mol^{-1} (M_{PS} = 185 kg mol^{-1}, M_{PVP} = 73 kg mol^{-1}, PDI = 1.17) and 188 kg mol^{-1} (M_{PS} = 135 kg mol^{-1}, M_{PVP} = 53 kg mol^{-1}, PDI = 1.18) with a PS volume fraction f_{PS} = 0.72. Analytical grade solvents acetone, toluene and anhydrous tetrahydrofuran (THF, contains 250 ppm BHT as inhibitor) were obtained from Sigma-Aldrich. The BCPs were dissolved in a 7 : 3 mixture of toluene : THF to obtain 0.5–1.0% (w/v) solutions. The solutions were left to stir overnight and filtered using a 0.22 μm pore size syringe filter to remove any undissolved particulates. Test grade (100) silicon wafers with the native oxide intact were washed using acetone and isopropanol followed by oxygen plasma cleaning for 1 min (Oxford Plasmalab System100). The BCP thin films were fabricated on 1/4 pieces of 2-inch Si wafers by spin coating at 2500–3000 rpm for ~60 s in a closed chamber SSE OPTIcoat spinner. The thin films were immediately soft-baked at 125 °C for 2 min to remove any residual solvent. Samples were diced

into 1 cm × 1 cm pieces and the initial thickness of the films was measured from the center of the pieces using a HeNe laser ellipsometer (Rudolph Research AutoEL III) at a 70° incident angle.

Solvent annealing device setup

The SVA chamber consisted of a custom-made stainless steel body and a detachable lid. The chamber had a maximum internal volume of V = 103 ml and could fit substrate wafers up to 2 inch in diameter. The copper stage plate was bonded to a thermoelectric cooler module (MultiComp, TEC 110 W, 12 A). The TEC element could either heat or cool the stage depending on the direction and magnitude of an electrical current driven through it (Thorlabs ITC4005 TEC controller). Temperature of the sample stage was monitored with a temperature transducer (AD590MF) for the feedback loop.

Dry nitrogen gas was bubbled through a temperature-stabilized solvent reservoir to generate the solvent vapor. The flow rate of the carrier gas was set constant using a gas regulator and a Brooks Instrument Sho-rate gas flow meter. The solvent vapor was fed into the chamber from a ring-structure at the bottom to ensure more uniform vapor distribution. The chamber inlet and outlet were equipped with ball valves making it possible to cut off all flows and make the chamber airtight. The solvent reservoir could also be bypassed so that pure nitrogen gas was fed through the chamber (purging). A Thorlabs TSP01 USB Data Logger was installed inside the SVA chamber to monitor the temperature of the gas vapor. The whole SVA setup was constructed in a temperature and humidity controlled clean room to minimize external influences.

The chamber allowed optical monitoring through a quartz viewport. A USB-connected CMOS camera (Thorlabs DCC1645C) was installed above the viewport to provide live video of the thin film surface during annealing. An LED ring light (Thorlabs OSL2 Fiber Illuminator) was used for sample illumination and the system was set up to record in dark-field mode. The thickness and swelling of the polymer film was determined *in situ* using spectroscopic reflectometry with an Ocean Optics spectrometer (HR4000) and a UV-Vis light source with a spot size of approx. 4 mm. To account for changes in the signal intensity and ambient lighting, the system was calibrated and referenced using a clean Si wafer before each run. The dry and swollen film thicknesses were determined by fitting a thin film model to the measured spectral data in real-time.[63] The model used optical constants that change with the addition of solvent according to the Lorentz–Lorenz rule of mixing.[64] For PS–P2VP, it was assumed the refractive index would comply with that of the majority block PS. Either a constant refractive index (n_{PS} = 1.59) or a wavelength dependent dispersion formula[65] was applicable. A refractive index of 1.407 was used for THF. Dispersion equations were used for toluene[66] and acetone.[67]

Automated annealing process

The BCP thin films were annealed in the solvent annealing device described above. The system was operated *via* a graphical user interface that was connected to the TEC controller, spectrometer and CMOS camera. Samples were placed on the TEC plate in the chamber and the chamber was flushed with dry N_2. Solvent vapor was introduced into the chamber *via* the temperature-stabilized bubbler at a constant N_2 carrier flow rate of 100 ml min^{-1}. BCP films were annealed in the solvent + N_2 vapor flow so that the film SR (or thickness) followed a predetermined profile. The extent of swelling was measured in real-time using reflectometry and controlled using a feedback loop that automatically adjusted the temperature of the sample stage by TEC. Currently, only the proportional gain in the PID controller was used. The up ramping rates were varied from 0.6 to 1.0 SR per min and annealing (dwell) times from 0 to 25 min. At the end, the swollen thin films were vitrified by purging the chamber with dry N_2. Additional heating (40 °C) was used to remove the residual solvent from the films.

Sample characterization

A metal salt infiltration process[68] was used to enhance imaging contrast between the two blocks of the BCP. The thin films were immersed in a 1 mM Na_2PtCl_4 + 0.1% HCl(aq) solution for 10–15 min, washed with deionized water and blow dried with nitrogen. The anionic platinum complexes bind specifically to the protonated PVP domains. The morphologies of the platinum-stained BCP films were examined with a field-emission scanning electron microscope (Carl Zeiss ULTRA 55) operated at 3 kV. For BCP lithography, the PVP cylinders were selectively removed by dipping in warm ethanol and the pattern was etched into Si by SF_6/O_2 dry etching.[62]

Morphology analysis and defect counting were done using ImageJ2[69] and MATLAB R2015b. The SEM images were converted into binary black-and-white images with automatic thresholding and noise was reduced by removing outlier pixels. The center positions were used to generate a Voronoi diagram, and the number of vertex edges was counted to determine the amount of lattice defects. The periodic hexagonal morphology was analyzed using Fast Fourier Transform (FFT) from 1024 × 1024 pixel binary images.

Conflicts of interest

There are no conflicts to declare.

Acknowledgements

We would like to thank Markus Hiekkamäki for programming the interface between the external hardware and the control software for our solvent annealing device. We thank also Dr Sokol Ndoni from the Technical University of Denmark for providing the PS-PDMS polymers. This work was supported by Tampere University under Grant No. #83026. The work is part of the Academy of Finland Flagship Programme, Photonics Research and Innovation (PREIN), decision #320165.

Notes and references

1 C. M. Bates and F. S. Bates, *Macromolecules*, 2017, **50**, 3–22.
2 C. Park, J. Yoon and E. L. Thomas, *Polymer*, 2003, **44**, 6725–6760.

3 M. A. Chavis, D.-M. Smilgies, U. B. Wiesner and C. K. Ober, *Adv. Funct. Mater.*, 2015, **25**, 3057–3065.
4 A. Rahman, P. W. Majewski, G. Doerk, C. T. Black and K. G. Yager, *Nat. Commun.*, 2016, **7**, 13988.
5 J. G. Kennemur, L. Yao, F. S. Bates and M. A. Hillmyer, *Macromolecules*, 2014, **47**, 1411–1418.
6 E. Kim, H. Ahn, S. Park, H. Lee, M. Lee, S. Lee, T. Kim, E.-A. Kwak, J. H. Lee, X. Lei, J. Huh, J. Bang, B. Lee and D. Y. Ryu, *ACS Nano*, 2013, **7**, 1952–1960.
7 Q. P. Chen, L. Barreda, L. E. Oquendo, M. A. Hillmyer, T. P. Lodge and J. I. Siepmann, *ACS Nano*, 2018, **12**, 4351–4361.
8 J. K. D. Mapas, T. Thomay, A. N. Cartwright, J. Ilavsky and J. Rzayev, *Macromolecules*, 2016, **49**, 3733–3738.
9 R. N. Carmean, T. E. Becker, M. B. Sims and B. S. Sumerlin, *Chem*, 2017, **2**, 93–101.
10 J. Frascaroli, S. Brivio, F. Ferrarese Lupi, G. Seguini, L. Boarino, M. Perego and S. Spiga, *ACS Nano*, 2015, **9**, 2518–2529.
11 A. Kikitsu, T. Maeda, H. Hieda, R. Yamamoto, N. Kihara and Y. Kamata, *IEEE Trans. Magn.*, 2013, **49**, 693–698.
12 M. P. Stoykovich, H. Kang, K. C. Daoulas, G. Liu, C.-C. Liu, J. J. de Pablo, M. Müller and P. F. Nealey, *ACS Nano*, 2007, **1**, 168–175.
13 H. Yi, X. Y. Bao, R. Tiberio and H. S. P. Wong, *Nano Lett.*, 2015, **15**, 805–812.
14 C.-C. Liu, E. Franke, Y. Mignot, R. Xie, C. W. Yeung, J. Zhang, C. Chi, C. Zhang, R. Farrell, K. Lai, H. Tsai, N. Felix and D. Corliss, *Nat. Electron.*, 2018, **1**, 562–569.
15 S. Park, Y. Kim, H. Ahn, J. H. Kim, P. J. Yoo and D. Y. Ryu, *Sci. Rep.*, 2016, **6**, 36326.
16 S. Rasappa, H. Hulkkonen, L. Schulte, S. Ndoni, J. Reuna, T. Salminen and T. Niemi, *J. Colloid Interface Sci.*, 2019, **534**, 420–429.
17 P. Mokarian-Tabari, R. Senthamaraikannan, C. Glynn, T. W. Collins, C. Cummins, D. Nugent, C. O'Dwyer and M. A. Morris, *Nano Lett.*, 2017, **17**, 2973–2978.
18 S. Vignolini, N. A. Yufa, P. S. Cunha, S. Guldin, I. Rushkin, M. Stefik, K. Hur, U. Wiesner, J. J. Baumberg and U. Steiner, *Adv. Mater.*, 2012, **24**, OP23–OP27.
19 J. Y. Kim, H. Kim, B. H. Kim, T. Chang, J. Lim, H. M. Jin, J. H. Mun, Y. J. Choi, K. Chung, J. Shin, S. Fan and S. O. Kim, *Nat. Commun.*, 2016, **7**, 12911.
20 IEEE, International Roadmap for Devices and Systems 2017 – Emerging Research Materials, https://irds.ieee.org/editions/2017.
21 L. D. Williamson, R. N. Seidel, X. Chen, H. S. Suh, P. Rincon Delgadillo, R. Gronheid and P. F. Nealey, *ACS Appl. Mater. Interfaces*, 2016, **8**, 2704–2712.
22 T.-H. Chang, S. Xiong, R. M. Jacobberger, S. Mikael, H. S. Suh, C.-C. Liu, D. Geng, X. Wang, M. S. Arnold, Z. Ma and P. F. Nealey, *Sci. Rep.*, 2016, **6**, 31407.
23 I. Bita, J. K. W. Yang, Y. S. Jung, C. A. Ross, E. L. Thomas and K. K. Berggren, *Science*, 2008, **321**, 939–943.
24 S.-J. Jeong, J. E. Kim, H.-S. Moon, B. H. Kim, S. M. Kim, J. B. Kim and S. O. Kim, *Nano Lett.*, 2009, **9**, 2300–2305.
25 F. Ferrarese Lupi, T. J. Giammaria, M. Ceresoli, G. Seguini, K. Sparnacci, D. Antonioli, V. Gianotti, M. Laus and M. Perego, *Nanotechnology*, 2013, **24**, 315601.
26 P. W. Majewski and K. G. Yager, *Soft Matter*, 2016, **12**, 281–294.
27 C. Sinturel, M. Vayer, M. Morris and M. A. Hillmyer, *Macromolecules*, 2013, **46**, 5399–5415.
28 S. H. Kim, M. J. Misner, T. Xu, M. Kimura and T. P. Russell, *Adv. Mater.*, 2004, **16**, 226–231.
29 Y. S. Jung and C. A. Ross, *Nano Lett.*, 2007, **7**, 2046–2050.
30 M. Y. Paik, J. K. Bosworth, D.-M. Smilgies, E. L. Schwartz, X. Andre and C. K. Ober, *Macromolecules*, 2010, **43**, 4253–4260.
31 S. Rasappa, L. Schulte, D. Borah, H. Hulkkonen, S. Ndoni, T. Salminen, R. Senthamaraikannan, M. A. Morris and T. Niemi, *Microelectron. Eng.*, 2018, **192**, 1–7.
32 X. Zhang, K. D. Harris, N. L. Y. Wu, J. N. Murphy and J. M. Buriak, *ACS Nano*, 2010, **4**, 7021–7029.
33 W. I. Park, K. Kim, H. I. Jang, J. W. Jeong, J. M. Kim, J. Choi, J. H. Park and Y. S. Jung, *Small*, 2012, **8**, 3762–3768.
34 W. I. Park, S. Tong, Y. Liu, I. W. Jung, A. Roelofs and S. Hong, *Nanoscale*, 2014, **6**, 15216–15221.
35 W. I. Park, Y. J. Choi, J. M. Yun, S. W. Hong, Y. S. Jung and K. H. Kim, *ACS Appl. Mater. Interfaces*, 2015, **7**, 25843–25850.
36 X. Gu, I. Gunkel, A. Hexemer and T. P. Russell, *Macromolecules*, 2016, **49**, 3373–3381.
37 X. Gu, I. Gunkel, A. Hexemer, W. Gu and T. P. Russell, *Adv. Mater.*, 2014, **26**, 273–281.
38 A. Baruth, M. Seo, C. H. Lin, K. Walster, A. Shankar, M. A. Hillmyer and C. Leighton, *ACS Appl. Mater. Interfaces*, 2014, **6**, 13770–13781.
39 K. A. Cavicchi and T. P. Russell, *Macromolecules*, 2007, **40**, 1181–1186.
40 J. D. Cushen, L. Wan, G. Pandav, I. Mitra, G. E. Stein, V. Ganesan, R. Ruiz, C. G. Willson and C. J. Ellison, *J. Polym. Sci., Part B: Polym. Phys.*, 2014, **52**, 36–45.
41 K. W. Gotrik, A. F. Hannon, J. G. Son, B. Keller, A. Alexander-Katz and C. A. Ross, *ACS Nano*, 2012, **6**, 8052–8059.
42 D. T. Hoang, J. Yang, K. Paeng, Y. Kwon, O. S. Kweon and L. J. Kaufman, *Rev. Sci. Instrum.*, 2016, **87**, 015106.
43 D. Posselt, J. Zhang, D.-M. Smilgies, A. V. Berezkin, I. I. Potemkin and C. M. Papadakis, *Prog. Polym. Sci.*, 2017, **66**, 80–115.
44 C. Jin, B. C. Olsen, E. J. Luber and J. M. Buriak, *Chem. Mater.*, 2017, **29**, 176–188.
45 R. Lundy, S. P. Flynn, C. Cummins, S. M. Kelleher, M. N. Collins, E. Dalton, S. Daniels, M. A. Morris and R. Enright, *Phys. Chem. Chem. Phys.*, 2017, **19**, 2805–2815.
46 G. Nelson, C. Drapes, M. Grant, R. Gnabasik, J. Wong and A. Baruth, *Micromachines*, 2018, **9**, 271.
47 A. Baruth, M. Seo, C. H. Lin, K. Walster, A. Shankar, M. A. Hillmyer and C. Leighton, *ACS Appl. Mater. Interfaces*, 2014, **6**, 13770–13781.
48 A. Knoll, R. Magerle and G. Krausch, *J. Chem. Phys.*, 2004, **120**, 1105–1116.
49 B.-J. Niebuur, J. Puchmayr, C. Herold, L. Kreuzer, V. Hildebrand, P. Müller-Buschbaum, A. Laschewsky and C. Papadakis, *Materials*, 2018, **11**, 850.
50 J. Jaczewska, A. Budkowski, A. Bernasik, I. Raptis, J. Raczkowska, D. Goustouridis, J. Rysz and M. Sanopoulou, *J. Appl. Polym. Sci.*, 2007, **105**, 67–79.

51 I. Smallwood, *Handbook of Organic Solvent Properties*, Elsevier, Oxford, 1996.
52 J. A. Emerson, D. T. W. Toolan, J. R. Howse, E. M. Furst and T. H. Epps, *Macromolecules*, 2013, **46**, 6533–6540.
53 W. Zeng, Y. Du, Y. Xue and H. L. Frisch, in *Physical Properties of Polymers Handbook*, ed. J. E. Mark, Springer New York, New York, 2007, pp. 289–303.
54 S. P. Paradiso, K. T. Delaney, C. J. García-Cervera, H. D. Ceniceros and G. H. Fredrickson, *Macromolecules*, 2016, **49**, 1743–1751.
55 C. T. Black, C. Forrey and K. G. Yager, *Soft Matter*, 2017, **13**, 3275–3283.
56 M. J. Maher, J. L. Self, P. Stasiak, G. Blachut, C. J. Ellison, M. W. Matsen, C. M. Bates and C. G. Willson, *ACS Nano*, 2016, **10**, 10152–10160.
57 Q. Yang and K. Loos, *Polymers*, 2017, **9**, 525.
58 C. T. Black and K. W. Guarini, *J. Polym. Sci., Part A: Polym. Chem.*, 2004, **42**, 1970–1975.
59 H. Yoshida, H. S. Suh, A. Ramírez-Hernández, J. I. Lee, K. Aida, L. Wan, Y. Ishida, Y. Tada, R. Ruiz, J. de Pablo and P. F. Nealey, *J. Photopolym. Sci. Technol.*, 2013, **26**, 55–58.
60 W. J. Durand, M. C. Carlson, M. J. Maher, G. Blachut, L. J. Santos, S. Tein, V. Ganesan, C. J. Ellison and C. G. Willson, *Macromolecules*, 2016, **49**, 308–316.
61 S. Ji, C.-C. Liu, J. G. Son, K. Gotrik, G. S. W. Craig, P. Gopalan, F. J. Himpsel, K. Char and P. F. Nealey, *Macromolecules*, 2008, **41**, 9098–9103.
62 H. H. Hulkkonen, T. Salminen and T. Niemi, *ACS Appl. Mater. Interfaces*, 2017, **9**, 31260–31265.
63 P. Yeh, *Optical waves in layered media*, Wiley-Interscience, Hoboken, NJ, 2005.
64 R. Mehra, *J. Chem. Sci.*, 2003, **115**, 147–154.
65 N. Sultanova, S. Kasarova and I. Nikolov, *Acta Phys. Pol., A*, 2009, **116**, 585–587.
66 S. Kedenburg, M. Vieweg, T. Gissibl and H. Giessen, *Opt. Mater. Express*, 2012, **2**, 1588.
67 J. Rheims, J. Köser and T. Wriedt, *Meas. Sci. Technol.*, 1997, **8**, 601–605.
68 J. Chai, D. Wang, X. Fan and J. M. Buriak, *Nat. Nanotechnol.*, 2007, **2**, 500–506.
69 C. T. Rueden, J. Schindelin, M. C. Hiner, B. E. DeZonia, A. E. Walter, E. T. Arena and K. W. Eliceiri, *BMC Bioinf.*, 2017, **18**, 529.